

# Advanced Propulsion for Microsatellites

by

Vadim Khayms

B.S., Aeronautics & Astronautics, MIT (1995)

B.S., Physics, MIT (1995)

S.M., Aeronautics & Astronautics, MIT (1997)

Submitted to the Department of Aeronautics & Astronautics  
in partial fulfillment of the requirements for the degree of

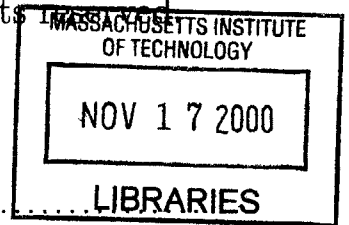
Doctor of Philosophy in Aeronautics & Astronautics

at the

MASSACHUSETTS INSTITUTE OF TECHNOLOGY

September 2000

© Massachusetts Institute of Technology 2000. All rights reserved.



Author .....

Department of Aeronautics & Astronautics  
June 23, 2000



Certified by .....

Manuel Martinez-Sanchez  
Professor  
Thesis Supervisor

Read by .....

Jack L. Kerrebrock  
Professor  
Thesis Reader

Read by .....

Akintunde I. Akinwande  
Professor  
Thesis Reader

Read by .....

George R. Ricker Jr  
Senior Research Scientist  
Thesis Reader

Accepted by .....

Nesbitt W. Hagood  
Chairman, Departmental Committee on Graduate Students

# Advanced Propulsion for Microsatellites

by

Vadim Khayms

Submitted to the Department of Aeronautics & Astronautics  
on June 23, 2000, in partial fulfillment of the  
requirements for the degree of  
Doctor of Philosophy in Aeronautics & Astronautics

## Abstract

Microsatellites have become increasingly popular in recent years as they offer significant cost savings, higher reliability, and are generally more affordable for a large variety of commercial applications. Since many microsatellite missions require considerable propulsion capabilities, miniaturization of the propulsion subsystem is critical in the design of most miniature spacecraft. A broad range of existing propulsion technologies have been considered for the purpose of identifying those devices which maintain high performance at small scale. Scaling laws were developed for each of the selected devices so as to preserve, whenever possible, the basic non-dimensional quantities which ultimately determine the performance of the individual thrusters at small scale. Hall thrusters were initially identified as most promising. In an effort to miniaturize the Hall thruster, a number of complications have been encountered. Some of the most troublesome were higher magnetic field requirements, larger internal heat fluxes and temperatures, and difficulties associated with the manufacturing of the various miniaturized components. In order to validate the proposed scaling laws, a 50 Watt Hall thruster has been designed, manufactured, and tested in a vacuum tank. Results of the experimental testing indicate that, although the maximum thrust levels obtained were on the order of 1.8 mN, about two thirds of the nominal design value, the propellant utilization efficiencies were unexpectedly low at approximately 40%. Close examination of the magnetic assembly has shown that the tip of the iron center pole was overheating during operation due to the insufficient heat conduction. The tip temperatures were estimated to reach 900°C, exceeding the Curie point of iron. As a consequence of the change in the magnetic field profile and the resultant leakage of electrons, the observed ionization fraction and, therefore, the utilization efficiency were lower than expected. Despite the low efficiencies, which were most likely caused by the design imperfections rather than physical limitations, the effort to miniaturize a Hall thruster has provided a number of useful insights for any such attempts in the future. Most importantly, this work has highlighted the generic difficulty, common to all plasma thrusters, associated with the increase of the plasma density as the scale of the device is reduced. The consequences of strict scaling, most notably the higher particle fluxes which cause an increase in the erosion rates and

significant loss of operating life at small scale, created a strong incentive to search for propulsion schemes which avoid ionization by electron bombardment.

In the quest for a more durable device that could operate at low power, yet provide sufficient operating life to be of practical interest, colloidal thrusters were considered for miniaturization. These are representatives of a technology of electrostatic accelerators which does not rely on ionization in the gas phase and, hence, their operating life is not compromised at small scale. In addition to their intrinsically small dimensions and extremely low operating power levels, eliminating the need for further “miniaturization”, colloidal thrusters possess a number of desirable characteristics which make them ideal for many microsatellite missions. Although the physics of electrospray emitters has been studied for decades, many of the mechanisms responsible for the formation of charged jets are still poorly understood. In order to gain further insight, a semi-analytical fluid model was developed to predict the effects of fluid’s viscosity on the flow pattern. Results of the analysis indicate that over a broad range of operating conditions viscous shear flow is insignificant in the vicinity of the jet irrespective of the fluid’s viscosity. In an attempt to further understand the physics of colloidal thrusters, specifically the effects of internal pressure, electrode geometry, and the internal electrostatic fields on the processes involved in the formation of charged jets, a detailed electrohydrodynamic model was formulated. A numerical scheme was developed to solve for the shape of the fluid meniscus given a prescribed set of operating conditions, fluid properties, and electrode configurations. Intermediate solutions for the conical region have already been obtained, however, convergence in the vicinity of the jet requires further studies. A fully developed model promises to provide valuable information and guidance in the design of colloidal thrusters.

Thesis Supervisor: Manuel Martinez-Sanchez

Title: Professor

## Acknowledgments

Successful completion of this work would not have been possible without the help, advice, and support of many individuals, some of whom I would like to thank here.

First and foremost, I would like to thank my advisor, Prof. M. Martinez-Sanchez for his patience, insight, and continuous support over the course of my graduate education. His immense knowledge of absolutely everything, his enthusiasm, and willingness to share this knowledge have been most invaluable.

I would like to thank Prof. Edgar Choueiri, Bob Sorenson, and John Ziemer at the Electric Propulsion and Plasma Dynamics Lab of Princeton University for allowing us to use their vacuum facilities to test the miniature thruster, for their time, resources, and support. I would also like to thank the personnel of the Busek company, Vlad Hruby and Jeff Monheiser, for loaning some of their equipment, without which many of the experiments would not have been possible, and for letting us use their vacuum facilities to perform preliminary test runs. I am also in debt to the personnel at the Electric Propulsion Lab at the Edwards Air Force Base, to Ron Spores and Greg Spanjers, for supporting laboratory testing at their facilities, and to Mike Fife and Jaime Malak for devoting their time in the lab.

I am also grateful to the engineering staff of the Dexter Magnetic Materials Division (Permag) for their support in the design and simulation of the magnetic circuitry and assembly of the microthruster components. Many thanks to the machine shop personnel of the Draper Laboratory, especially to Edward McCormack for his valuable advice and help in manufacturing some of the low-tolerance components for the Hall thruster. His capabilities in performing seemingly impossible machining tasks were quite impressive.

I would also like to thank Bohus Ondrusek for his help in the testing phase of the miniature Hall thruster. Always eager to help, his experience with cathodes was extremely valuable in the initial attempts to operate the Hall thruster.

Many thanks to the staff members at the department of Aeronautics & Astronautics of MIT for their technical assistance and advice: Dick Perdichizzi, Paul Bauer,

Donald Wiener. Thanks to Sharon Leah Brown and Peggy Edwards for all the cookies, candies, and last but not least, all the help during the past several years. Also, thanks to the undergraduate students who have helped with the assembly of the thrust balance, most notably Maria Ishutkina, Jeff Reichbach, and Marshall Brenizer.

I would also like to thank Bernard Asare, my former roommate and an officemate, for all the coffee and all the stimulating discussions.

I am most grateful to my girlfriend, Sofya, for proof-reading half of my thesis, and then insisting that I acknowledge her contribution to rocket science; and, of course, for all the moral support and help as this document was slowly coming into existence.

I am most indebted to my parents, Alik and Nelya, as well as to my brother Alex for always believing in me and for constantly inspiring and encouraging me to do my best. My coming and successfully graduating from MIT (on multiple occasions) is credited exclusively to them.

# Contents

<b>1</b>	<b>Introduction</b>	<b>13</b>
1.1	Advantages of Micro-satellites . . . . .	13
1.2	Propulsion System Options . . . . .	14
1.3	Goals & Objectives . . . . .	15
<b>2</b>	<b>Scaling of Existing Propulsion Technologies</b>	<b>17</b>
2.1	Introduction . . . . .	17
2.2	Hall Thrusters . . . . .	18
2.2.1	Principles of operation . . . . .	18
2.2.2	Ionization efficiency . . . . .	18
2.2.3	Confinement of electrons . . . . .	20
2.2.4	Magnetic confinement schemes . . . . .	22
2.2.5	Performance analysis . . . . .	23
2.3	Ion Engines . . . . .	24
2.3.1	Principles of operation . . . . .	24
2.3.2	Confinement of neutrals . . . . .	25
2.3.3	Confinement of electrons . . . . .	27
2.3.4	Scaling of the ion optics . . . . .	28
2.4	Pulsed Inductive Thrusters . . . . .	30
2.4.1	Principles of operation . . . . .	30
2.4.2	Loss mechanisms and scaling . . . . .	30
2.5	Contact Ionization Thrusters . . . . .	33
2.5.1	Principles of operation . . . . .	33

2.5.2	Scaling of contact ionization thrusters . . . . .	34
2.6	Colloidal Thrusters . . . . .	37
2.6.1	Principles of operation . . . . .	38
2.6.2	Applicability to micro-propulsion . . . . .	39
2.7	Field-Effect Electrostatic Propulsion (FEEPs) . . . . .	41
2.7.1	Principles of operation . . . . .	41
2.7.2	Applicability to micro-propulsion . . . . .	42
2.8	Summary . . . . .	43
2.8.1	Hall thrusters . . . . .	43
2.8.2	Ion engines . . . . .	44
2.8.3	Pulsed inductive thrusters . . . . .	44
2.8.4	Contact ionization thrusters . . . . .	45
2.8.5	Colloidal thrusters . . . . .	45
2.8.6	Field-Effect Electrostatic Propulsion . . . . .	46
2.8.7	Recommendations . . . . .	46
<b>3</b>	<b>Design of a 50W Hall Thruster</b>	<b>47</b>
3.1	Introduction . . . . .	47
3.2	General Design Considerations . . . . .	48
3.3	Magnetic Circuit Design . . . . .	49
3.4	Thermal Design/Material Selection . . . . .	53
3.5	Cathode Design . . . . .	56
3.6	Final Design . . . . .	56
<b>4</b>	<b>Experimental Testing of a 50-Watt Hall Thruster</b>	<b>59</b>
4.1	Preliminary testing attempts . . . . .	59
4.2	Testing Facility . . . . .	62
4.2.1	Vacuum Tank . . . . .	62
4.2.2	Thrust Balance, Calibration, & Data Acquisition . . . . .	63
4.2.3	Cathode . . . . .	64
4.2.4	Flow system . . . . .	65

4.3	Test results . . . . .	65
4.4	Analysis . . . . .	67
4.5	Alternative scaling scenarios . . . . .	70
4.6	Conclusions and recommendations . . . . .	76
<b>5</b>	<b>Physics of Colloidal Thrusters</b>	<b>80</b>
5.1	Literature Review . . . . .	80
5.1.1	Scientific work in the area of electro-spray physics . . . . .	80
5.1.2	Developments in the field of colloidal propulsion . . . . .	82
5.2	Weaknesses of current models . . . . .	84
5.3	Scaling and performance of colloidal thrusters . . . . .	87
5.3.1	Electrostatics of cone-jet emitters . . . . .	87
5.3.2	Formation of the jet . . . . .	93
5.3.3	Production of droplets . . . . .	97
5.3.4	Regimes of operation . . . . .	100
5.4	Ion emission . . . . .	106
5.4.1	Mixed-regime operation . . . . .	110
<b>6</b>	<b>Creeping Flow Model for a Conical Meniscus</b>	<b>115</b>
6.1	Introduction . . . . .	115
6.2	Model Formulation . . . . .	117
6.3	Numerical Procedure and Results . . . . .	123
<b>7</b>	<b>Electro-Hydrodynamic Model of a Cone-jet Emitter</b>	<b>127</b>
7.1	Introduction and Literature Survey . . . . .	127
7.2	Model description and assumptions . . . . .	129
7.3	External electrostatics model . . . . .	131
7.4	Electrohydrodynamics at the fluid interface . . . . .	135
7.4.1	Surface electrostatics . . . . .	135
7.4.2	Stress and momentum balance . . . . .	138
7.5	Results of the numerical model . . . . .	140

7.5.1	Summary of the model . . . . .	140
7.5.2	Preliminary numerical results . . . . .	142
7.6	Conclusions . . . . .	143
<b>8</b>	<b>Conclusions and Recommendations for Future Work</b>	<b>145</b>
8.1	Contributions to the scaling methodology . . . . .	145
8.2	Recommendations pertinent to scaling of Hall thrusters . . . . .	148
8.2.1	Theoretical work . . . . .	148
8.2.2	Experimental work . . . . .	149
8.3	Contributions to the modeling of colloidal thrusters . . . . .	150
8.4	Recommendations pertinent to the modeling of colloidal thrusters . .	151
<b>A</b>	<b>Additional Considerations in the Scaling of Hall Thrusters</b>	<b>153</b>
<b>B</b>	<b>Additional Considerations in the Design of a 50 W Hall Thruster</b>	<b>158</b>
B.0.1	Vacuum insulation . . . . .	158
B.0.2	Analytical thermal model of the anode . . . . .	159

# List of Figures

2-1	Hall thruster schematic . . . . .	19
2-2	Scaling of plasma density . . . . .	21
2-3	Scaling of magnetic confinement schemes . . . . .	23
2-4	Ion thruster schematic . . . . .	25
2-5	PIT schematic . . . . .	30
2-6	Schematic of a contact ionization thruster . . . . .	33
2-7	Current density vs. temperature for cesium-tungsten configuration . . . . .	35
2-8	Colloidal thruster schematic . . . . .	38
2-9	FEEP schematic . . . . .	42
3-1	Magnetic circuit geometry (all dimensions in <i>mm</i> ) . . . . .	51
3-2	Magnetic flux profile (courtesy of Dexter Magnetics) . . . . .	51
3-3	Magnetic circuit assembly . . . . .	52
3-4	Anode schematic [all dimensions in inches (mm)] . . . . .	55
3-5	Anode . . . . .	55
3-6	Final design schematic . . . . .	57
3-7	Anode assembly . . . . .	58
3-8	Final assembly . . . . .	58
4-1	Operational testing . . . . .	60
4-2	Vacuum facility schematic . . . . .	63
4-3	Cooling jacket . . . . .	64
4-4	50W Hall thruster performance . . . . .	66
4-5	50W Hall thruster performance . . . . .	67

4-6	Test data . . . . .	68
4-7	Dependence of the efficiency on the mean free path parameter $\tilde{h}$ . . . . .	73
4-8	General scaling strategies . . . . .	74
4-9	Scaling scenarios . . . . .	75
4-10	Erosion pattern at the center pole piece . . . . .	79
5-1	Conical geometry . . . . .	91
5-2	Operating regimes: a) charge relaxation effect, b) dynamic pressure effect . . . . .	101
5-3	Onset of the minimum flow rate (boundary indicates maximum allowable current for a given flow rate) . . . . .	103
5-4	Onset of ion emission (dashed line indicates the current obtained in the absence of ion emission) . . . . .	111
5-5	Mixed-regime scenario . . . . .	114
6-1	Coordinate definitions . . . . .	118
6-2	Streamline map (horizontal axis is the axis of symmetry, all dimensions given in meters) . . . . .	124
7-1	Computational domain (assuming cylindrical symmetry) . . . . .	131
7-2	Coordinate definition . . . . .	132
7-3	Computational grid . . . . .	133
7-4	Surface field configuration . . . . .	135
7-5	Internal field configuration . . . . .	137
7-6	Force diagram . . . . .	138
7-7	Sample solution . . . . .	143
B-1	Vacuum gap insulation . . . . .	159
B-2	1-D thermal model . . . . .	160
B-3	(a) Anode temperature profile; (b) Radiative heat fluxes . . . . .	161

# List of Tables

3.1 Scaled Design Parameters . . . . . 48

# Chapter 1

## Introduction

### 1.1 Advantages of Micro-satellites

Ever since the very beginnings of man's ventures into space, costs of delivering and deploying complex multi-functional spacecraft and scientific instruments into orbit have played a major role in their design and implementation. Although launch vehicle capabilities have improved significantly over the past thirty years, allowing larger and more capable spacecraft to be launched, recent changes in government policies and defense spending as well as the resulting budget constraints have shifted the emphasis of most spacecraft manufacturers almost entirely to cost. Reduction of these costs is the main incentive for producing and flying small scale satellites [1].

Although the benefit of flying smaller and, therefore, lighter spacecraft from the overall launch cost perspective may be apparent, additional advantages make micro-spacecraft a viable alternative for a number of potential missions. For instance, functionality of a single spacecraft can be effectively distributed among several smaller vehicles, thus reducing the complexity of each individual spacecraft, reducing the design and manufacturing costs per satellite, and improving the reliability of the overall system. The need for integrating a number of diverse and, at times, incompatible functions on a single spacecraft in the past has produced compromised solutions which often suffered from poor and inefficient designs. By redistributing functionality and focusing on the individual subsystems and components at a functional level, sig-

nificant improvements in the design efficiency could be achieved. Lastly, reduction of the complexity of individual spacecraft would facilitate rapid prototyping, lower the development life-cycle, and stimulate more efficient and economical production and manufacturing practices. Even if the functionality of a spacecraft were reduced in proportion, lower costs of the resulting less capable spacecraft may attract additional users thus broadening the spectrum of applications and opening up new avenues in space exploration [2].

The recent emphasis on cost reduction and down-sizing of spacecraft has forced a reevaluation of technologies which may have critical impact on spacecraft mass. For many commercial, scientific, and military missions on-board propulsion has been a dominant contributor to the overall mass of the spacecraft. As many of these missions generally require a wide range of on-orbit functions, including orbit raising, drag makeup, station-keeping, and attitude control, the use of miniature high performance propulsion on board of these spacecraft would help reduce the subsystem weight and, therefore, aid in achieving the ultimate goal of deploying cost-effective and reliable spacecraft. Recent communications and remote sensing missions introduce additional requirements for constellation maintenance and mandatory end-of-life deorbit, both of which result in the increase of the overall propulsive requirements. New spacecraft architectures, costs of ground testing and handling of toxic or hypergolic propellants all lead to the considerations of alternative propulsion technologies, once again demonstrating the urgent need for development of more capable miniature high-performance propulsion.

## 1.2 Propulsion System Options

The choice of an appropriate propulsion system for most spacecraft is primarily dictated by the specific mission objectives that nowadays demand increasingly better propulsion capabilities. A number of recent scientific missions, such as JPL's LISA mission (Laser Interferometer Space Antenna), require low thrust propulsion capable of delivering precise impulse bits at the thrust level of about 1-20  $\mu N$ . Due to the

insignificant use of on-board propulsion and small overall velocity increments ( $\Delta V$ ) such missions can tolerate lower specific impulse and efficiencies. On the other hand, missions intended for long duration deep space exploration (such as New Millennium DS-1), which require large velocity increments, usually optimize in the high specific impulse ( $I_{sp}$ ) regime at 2,000 sec and above. A large number of near-Earth missions such as constellation flights or missions requiring north-south station keeping, drag makeup, and other moderately intensive orbit maintenance maneuvers, all optimize in the intermediate  $I_{sp}$  range between 1,000 and 1,600 sec. Electric thrusters capable of efficiently delivering low thrust within a wide range of  $I_{sp}$  become suitable for a majority of such missions accommodating a diverse set of requirements, ranging from performing auxiliary attitude/position control tasks to economically delivering substantial velocity increments over extended periods of time. A summary of the propulsion system options to satisfy specific mission requirements is detailed in Ref. [3].

### 1.3 Goals & Objectives

A number of existing electric propulsion devices already possess those desirable characteristics that make them ideal for a number of representative micro-satellite missions. It may, therefore, be possible to scale these devices down to a length scale at which they can be efficiently operated at low power. The power levels to which these devices can be scaled are arbitrary, however, it is expected that scaling limitations will, in general, impose constraints on the achievable reduction in size and power. Those devices that are deemed to be most promising at small scale can be subsequently modified so as to preserve their basic operating characteristics, then miniaturized, manufactured, and tested to validate the scaling laws used in their design. The objective of this work is multi-fold. First, a generic scaling evaluation and an overview of some of the existing propulsion technologies will be performed. This will be accomplished by modeling their operating characteristics based on the known physics of these devices while, at the same time, identifying potential performance

limitations and implementation hurdles. A number of operational and handling issues will be considered as well.

A single device which is suitable for miniaturization and shows greatest potential for microsatellite applications will be selected and pursued further through development, manufacturing, and testing. Some of the physical limitations encountered in the scaling process will be analyzed and addressed in the design. Results of the experimental testing would be used to assess the validity of the scaling model and reveal challenges, if any, in the design and implementation of similar devices at small scale. Recommendations as to the possible improvements will be made based on the accumulated body of knowledge and experience. A number of alternative technologies will be considered for miniaturization as well. Numerical modeling will be employed to gain further understanding of the physics and the operational characteristics of these novel devices to enable future design and implementation.

# Chapter 2

## Scaling of Existing Propulsion Technologies

### 2.1 Introduction

The goal of this chapter is to provide a comprehensive overview of the existing propulsion technologies, emphasizing scalability of the major performance metrics such as the specific impulse, efficiency, and life, subject to the reduction in size and operating power. Simple scaling arguments based on the governing physics will be presented and employed in each case, as appropriate, to demonstrate feasibility of miniaturization.

The following technologies will be considered: ion thrusters, Hall thrusters, contact ionization thrusters, pulsed inductive thrusters, colloidal thrusters, and Field-Effect Electrostatic Propulsion (FEEPs). For the purposes of the discussion, these technologies will be subdivided into two categories: those relying on gas phase ionization (ion thrusters and Hall thrusters) and those relying on alternative means of ionizing the working fluid. Operation and scaling of gas-phase ionization devices will be discussed first. This will be followed by the analyses of the remaining systems with the objective of identifying those which demonstrate superior performance at small scale.

## 2.2 Hall Thrusters

### 2.2.1 Principles of operation

Hall thrusters were originally developed in Russia in the 1960s and since then have been extensively studied, both theoretically and experimentally. Nowadays, although somewhat less efficient than the state-of-the-art ion engines, their relative simplicity and compactness make Hall thrusters quite attractive, especially at small scale.

Hall thrusters accelerate ionized propellant through an electrostatic potential, thereby ejecting ions at high speed and producing thrust by reaction. A schematic of a generic Hall thruster is shown in Fig. 2-1. Ionization of neutrals relies on collisions of neutrals with the electrons. Electrons are emitted by the cathode as they enter the ionization zone where they are trapped in the magnetic field preventing them from streaming directly into the anode. Through collisions and turbulent scattering, both primary and secondary electrons can penetrate the magnetic field lines towards the anode, sustaining the ionization discharge. A potential difference externally applied between the anode and the cathode produces an axial electric field. The two fields set in mutually perpendicular directions result in an electron  $\mathbf{E} \times \mathbf{B}$  drift motion in the azimuthal direction, perpendicular to both the electric and the magnetic fields. The  $e\mathbf{v} \times \mathbf{B}$  force on the electrons due to this drift balances the electrostatic force on them, and the corresponding reaction on the magnetic assembly transmits the thrust to the body. This is the origin of the generic “Hall Thruster” designation for this device.

### 2.2.2 Ionization efficiency

The Hall thruster technology has by now reached its maturity and over the course of the past 20 – 30 years individual thruster assemblies have been experimentally optimized with respect to the various configurations and operating regimes. It is, therefore, desirable to preserve these optimum characteristics (e.g. specific impulse and efficiency) under scaling. This can be accomplished by identifying the relevant

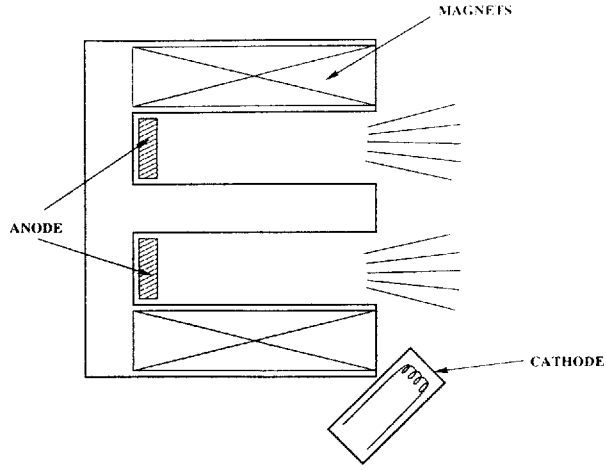


Figure 2-1: Hall thruster schematic

parameters that govern their physics and enforcing them to remain constant under scaling. All the basic plasma characteristics in gas-phase ionization devices rely heavily on the ionization process, whereby the neutrals are ionized in collisions with the electrons. As the size of the device is reduced, all else remaining constant, the number of collisions that the electrons and the neutrals experience with each other as they traverse the effective length of the device is reduced. Thus, in order to maintain the effective collision probability, it is necessary to increase the number densities of all the species in proportion. Equivalently, the mean free paths of the species between the consecutive collisions must scale with the characteristic length of the device:

$$h \equiv \frac{\lambda}{L} = \left( \frac{v_n}{c_e Q} \right) \frac{1}{nL} \quad (2.1)$$

where  $\lambda$  is the mean free path,  $n$  is the particle number density,  $Q$  is the collision cross-section,  $L$  is the characteristic size of the device,  $v_n$  and  $c_e$  are the thermal velocities of the neutrals and the electrons respectively. It was shown in Ref. [4], that the electron energy equation is consistent with the assumption that the electron temperature is constant and independent of scale, hence  $c_e$  must remain constant (refer to Appendix A for additional details). Therefore, the number density can be written as:

$$n \sim \frac{1}{Lh} \quad (2.2)$$

indicating that at constant  $h$  the number density  $n$  must scale inversely with size, as expected. Incidentally, surface erosion rates of the thruster components exposed to the ion beam are proportional to the ion flux into the wall which scales in proportion with the ion number density. Therefore, the expected life of exposed thruster components would scale as the ratio of the characteristic thickness to the erosion rate:

$$T_{life} \sim \frac{L}{n} \sim L^2 h \quad (2.3)$$

Existing 1.35 kW Hall thrusters have undergone laboratory lifetime tests and have demonstrated a maximum life of just over 7,000 hrs. Thus, a ten-fold reduction in operating power would already decrease the theoretical operating life to only 70 hours. It is the lifetime limitation that makes miniature gas-phase ionization thrusters impractical for most long-term missions (unless scaling and performance are relaxed, as discussed in Sec. 4.5). The on-board power processing equipment is generally dominated by the weight of the solar array whose weight scales as the array area ( $L^2$ ). Since the thruster mass, which scales as  $L^3$ , becomes less and less dominant in comparison to the power processing equipment at small scale, the overall lifetime can be improved by introducing a system of redundant thrusters. In addition, properly chosen materials and magnetic field configurations can reduce the erosion rates and improve lifetime even further. A graphical summary of these scaling arguments and their consequences is schematically shown in Fig. 2-2. The lines of constant plasma density are shown as hyperbolas of the form  $n = 1/Lh$ . It can be seen that, although the lifetime generally suffers at small scale, additional improvements are possible at small values of  $L$  by compromising on the invariance of the scaling ratio  $h$ .

### 2.2.3 Confinement of electrons

Under the influence of an applied electric field, electrons emitted by the cathode are free to migrate towards the anode, in which case their residence time in the ionization region would not be sufficient to produce ionizing collisions with neutrals and sustain ionization. An external magnetic field is generally employed for the

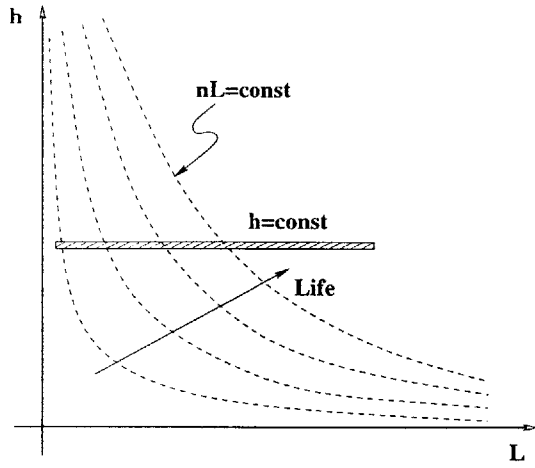


Figure 2-2: Scaling of plasma density

purpose of trapping the electrons so that they can spiral around the magnetic field lines, thus increasing their residence time within the chamber. The ratio ( $f$ ) of the Larmor radius to the thruster dimension can be used as a quantity characterizing the effectiveness of such a confinement scheme (refer to Appendix A for details). For adequate confinement  $f$  must be much smaller than unity. In fact, typical values of  $f$  in the existing Hall thrusters range anywhere between 0.008 and 0.01. The quantity  $f$  can be expressed as follows:

$$f = \frac{r_L}{L} = \left( \frac{mv}{eB} \right) \frac{1}{L} \quad (2.4)$$

To preserve  $f$  under scaling the strength of the magnetic field must vary inversely with length:

$$B \sim \frac{1}{Lf} \quad (2.5)$$

This result indicates that, in order to maintain sufficient confinement of electrons, stronger fields are required at small scale. Existing 1.35 kW Hall thrusters operate at a magnetic field strength of 0.02 T. Keeping  $f$  constant, a thruster with a ten-fold reduction of power would require a field strength of 0.2 T. The following section addresses the feasibility of creating such magnetic fields and discusses the options available to do so.

## 2.2.4 Magnetic confinement schemes

Most of the existing Hall thrusters in the power range between 200 W and 5 kW utilize electric coils to produce the required magnetic field. Ion engines, on the other hand, due to their intrinsic geometry generally use permanent magnets. It is interesting to first examine whether electric coils are still practical at small scale. To do so, consider a simplified model of a magnetic circuit with a narrow gap  $g$  driven by a coil with  $N$  turns and carrying a constant current  $I$ . The strength of the magnetic field produced within the gap is given by the following relation:

$$B = \frac{\mu_o IN}{g} \quad (2.6)$$

Since  $g$  is proportional to  $L$  and  $B$  scales as  $1/Lf$ , the product  $IN$  must scale as  $1/f$ . Although it is not always the case, it is useful to assume for the purposes of the current discussion, that most Hall thrusters use their main discharge current to drive the magnets. The discharge current  $I$  can be determined as the product of the current density times the area of the device:

$$I \sim jL^2 \sim nL^2 \sim \frac{L}{h} \quad (2.7)$$

Suppose, for simplicity, that  $h$  is kept constant. Then,  $I \sim L$  and  $N \sim 1/Lf$ . The coil resistance scales as the total wire length  $NL$  divided by the cross-sectional area of the wire  $L^2/N$ , so that:

$$R \sim \frac{N^2}{L} \sim \frac{1}{L^3 f^2} \quad (2.8)$$

The power dissipated as heat is given by  $Q = I^2 R$ . In steady state  $Q$  must be conducted out to the surroundings, therefore,  $Q \sim \Delta T L$  or:

$$\Delta T \sim \frac{1}{L^2 f^2} \quad (2.9)$$

This result suggests that if the temperature of the coils in a large thruster is elevated by only ten degrees with respect to the surroundings, a five-fold reduction in size

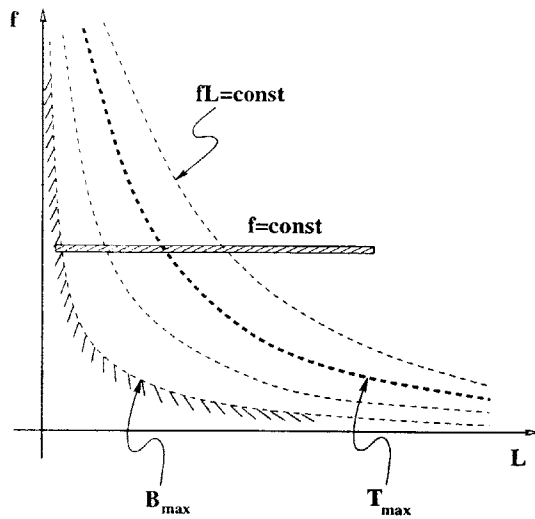


Figure 2-3: Scaling of magnetic confinement schemes

would create a temperature elevation of 250 degrees ! It is, therefore, quite clear that electric coils are not suitable for miniature devices. The strongest existing permanent magnets, on the other hand, (such as SmCo alloys) are capable of producing magnetic fields on the order of 1 T. It is that figure of merit, representing the maximum achievable magnetic field strength, that limits the scalability of gas-phase ionization devices. A generic representation of the scaling for the magnetic field is illustrated in Fig. 2-3. The lines of constant magnetic field strength are hyperbolas of the form  $B = 1/Lf$ . The lines of constant  $\Delta T$  are also hyperbolas of the form  $\Delta T^2 = 1/Lf$ . The dotted line represents an upper temperature limit beyond which electrical coils are no longer practical. The boundary on the left-hand side is the field strength limit beyond which no known magnet exists that can produce the required field and beyond which scaling at constant  $f$  is no longer feasible.

### 2.2.5 Performance analysis

It is the purpose of this section to utilize the previously developed scaling relations to discuss the scalability of thruster efficiency and specific impulse. As a result, it may be possible to infer the limitations of the attainable performance of Hall thrusters at small scale in comparison to the competing technologies.

An axial electric field created between the anode and the cathode imparts kinetic energy to the ions ejecting them at high speed. Their exhaust velocity can be

determined by applying conservation of energy:

$$c = \sqrt{\frac{2eV}{m_i}} \quad (2.10)$$

where  $m_i$  is the ion mass, and  $V$  is the applied voltage. Clearly, in order to preserve the specific impulse, it is necessary to keep the applied voltage constant. The thruster efficiency can be determined as the ratio of the useful beam power to the input power in the form:

$$\eta = \frac{\dot{m}c^2}{2IV} \quad (2.11)$$

where  $\dot{m}$  is the mass flow rate,  $I$  is the anode current,  $V$  is the applied voltage, and  $c$  is the exhaust speed. Since the flow rate scales as the product of the plasma density and the area  $nL^2$  while the current scales with  $L$ , the efficiency must scale as:

$$\eta \sim \frac{nL^2}{L} \sim 1 \quad (2.12)$$

and, therefore, remains constant. It has been shown [4] that the major loss mechanisms associated with recombination of ions at the walls, radiation losses, as well as the propellant utilization  $m_i I_a / e$  all scale in proportion to the characteristic dimension  $L$ , confirming that the obtained efficiency must, indeed, be independent of scale. The analysis of some of the relevant loss mechanisms is presented in Appendix A. Incidentally, currently existing 1.35 kW Hall thrusters have demonstrated efficiencies on the order of 50 – 55%. It is, therefore, conceivable that a miniature Hall thruster could be built to operate at an  $I_{sp}$  of 1,600 sec with a comparable efficiency.

## 2.3 Ion Engines

### 2.3.1 Principles of operation

In their standard configuration ion engines accelerate ionized propellant through a set of extractor grids expelling ions at high speed and producing thrust by reaction. A simplified diagram of an ion engine is schematically shown in Fig. 2-4. The main

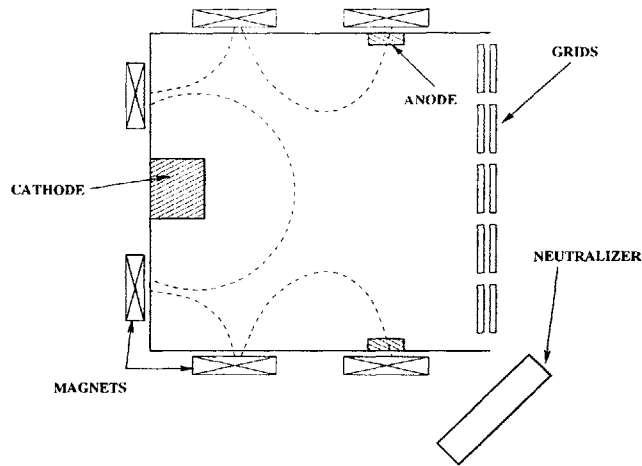


Figure 2-4: Ion thruster schematic

distinction in the configuration of ion engines compared to that of Hall thrusters is that ion engines make use of a set of grids to accelerate ions and, therefore, require an additional power supply to sustain ionization discharge and another power supply to heat the cathode filament which emits electrons within the ionization chamber. Due to this additional complexity, ion engines are generally considered inferior to the Hall thruster, even though, because of the larger operating voltages, they usually demonstrate efficiencies 5 – 10% higher than the Hall thrusters.

Although the scaling analysis for ion engines is similar to the one performed for the Hall thrusters, it is worth developing the model from first principles. It will be shown shortly that, unlike the geometry of Hall thrusters, the grids of an ion engine do not scale geometrically with the ionization chamber. For that reason, the overall configuration of a miniature ion engine needs to be revisited and the invariance of certain characteristic quantities, in general, can not be automatically assumed.

### 2.3.2 Confinement of neutrals

The geometry of a typical ion engine is such that the neutrals are free to escape from the ionization chamber through the grid holes without encountering any ionizing collisions with the electrons. In order to ensure that a sufficient percentage of the neutrals are ionized, it is necessary for the residence time of the neutrals within the ionization chamber to be much longer than the mean time between ionizing collisions.

The residence time of the neutrals within the ionization chamber is given by:

$$t_{res} = \frac{m_i n_n V}{\dot{m}_n} \quad (2.13)$$

where  $n_n$  is the density of neutrals,  $\dot{m}$  is the flow rate of neutrals, and  $V$  is the volume of the ionization chamber such that  $V = AL$  where  $A$  is the cross-sectional area of the device and  $L$  is the chamber length. The mass flow rate of neutrals escaping through the grid holes can be expressed in terms of the effective open area fraction (transparency ratio)  $\phi_n$  as follows:

$$\dot{m}_n = m_i \frac{n_n c_n}{4} A \phi_n \quad (2.14)$$

On the other hand, the mean time between the ionizing collisions is given by:

$$t_i = \frac{1}{\nu_i} = \frac{1}{n_e c_e \sigma_i} \quad (2.15)$$

where  $n_e$  is the electron density,  $c_e$  is the mean thermal velocity of the electrons, and  $\sigma_i$  is the ionization cross-section. In order to ensure that at least one ionizing collision occurs during the time that a neutral particle resides within the ionization chamber,  $t_{res}$  must be greater than  $t_i$ , or:

$$\frac{4Ln_e c_e \sigma_i}{c_n \phi_n} > 1 \quad (2.16)$$

Disregarding quantities which are independent of scale (assuming  $T_e$  is invariant), the above equation reads as follows:

$$\frac{n_e L}{\phi_n} \sim const \quad (2.17)$$

If  $\phi_n$  were to remain constant, the latter relation for the number density would be consistent with the one obtained earlier for the case of Hall thrusters.

### 2.3.3 Confinement of electrons

Although the idea of scaling the Larmor radius in proportion to the size of the device is still applicable, the cusped geometry of the magnetic field lines permits the additional freedom of placing the anode such as to allow an appropriate proportion of electrons to be captured. Just as in the case of the analysis for the neutrals, it is useful to examine the relative magnitudes of the mean time for a primary electron to encounter an ionizing collision and the mean diffusion time of such an electron across the magnetic field lines. The mean time for a primary electron to ionize a neutral is given by the following relationship:

$$t_i = \frac{1}{n_n v_p \sigma_i} \quad (2.18)$$

where  $v_p$  is the mean velocity of primary electrons. Assuming Bohm diffusion to be the dominant transport mechanism, the mean diffusion time for a primary electron is given by:

$$t_{diff} \sim \frac{L^2}{\Delta} \sim f^2 A \frac{16e B_{ave}}{kT_e} \quad (2.19)$$

where  $B_{ave}$  is the effective magnitude of the magnetic field within the region where electrons reside while diffusing towards the anode. A dimensionless geometrical factor  $f$  has been introduced to account for the relative location of the anode with respect to the magnetic poles (large  $f$  when the anode is “between cusps”, smaller when it is directly in line with one). Larger values of  $f$  are equivalent to a reduction of the diffusivity  $\Delta$ , hence, yield a longer time for an electron to diffuse to the anode. For sufficient utilization of the primary electrons  $t_{diff}$  must be of the same order as  $t_i$ , or:

$$f^2 A B_{ave} n_n \sim 1 \quad (2.20)$$

Since the input power scales with  $n_n A$ , one can rewrite the above relation as follows:

$$f^2 B_{ave} P \sim 1 \quad (2.21)$$

With the exception of an additional geometrical factor  $f$ , this result is identical to the one obtained earlier for the scaling of the magnetic field in Hall thrusters. In this case, however, additional flexibility is offered by allowing the appropriate placement of the anode to draw just enough primary electrons to sustain ionization discharge. It should be noted, however, that if the effective Larmor radius is chosen to be of the same order as the dimension of the ionization chamber or less, most of the electrons would be rapidly drawn towards the anode irrespective of its position. Hence, ion thrusters, just as the Hall thrusters, suffer from a similar lower bound on the size determined by the maximum attainable magnetic field. Taking the mean field to be on the order of 0.1 Tesla, the corresponding minimum chamber size for which the electrons are still sufficiently confined is about 1 – 2 mm. The currently existing models of ion engines already utilize magnets which produce magnetic fields on the order of 0.1 – 0.2 T. It may, therefore, be difficult to achieve large reduction in size and power without sacrificing electron confinement characteristics. One way to partially offset this complication is to make the magnets proportionally larger as the chamber size is reduced. In such a case, the region occupied by the electrons will be disproportionately closer to the magnetic poles resulting in concentration of the field strength at that location and, therefore, improving the confinement efficiency. Conclusive analysis of such a scheme, however, requires detailed numerical modeling and will be avoided for the purposes of this preliminary analysis.

### **2.3.4 Scaling of the ion optics**

Most of the existing models of ion engines utilize an extractor grid with a large number of holes sized in such a way as to be no larger than twice the characteristic Debye length. Had the holes been larger in diameter, the electrodes would have been completely shielded by the sheath and the ions would have been free to escape from the ionization chamber without undergoing any acceleration. Although smaller holes are acceptable as well, manufacturing these introduces unnecessary fabrication/assembly difficulties and is usually avoided. Following this logic the expression for the hole size

can be written as :

$$d_h = 2\sqrt{\frac{\epsilon_0 k T_e}{e^2 n_e}} \left( \frac{eV}{kT_e} \right)^{3/4} \quad (2.22)$$

Since the plasma density scales inversely with  $L/\phi_n$ , the hole diameter would scale as:

$$d_h \sim \sqrt{\frac{L}{\phi_n}} \quad (2.23)$$

This result indicates that the holes become larger in proportion as the size of the device is reduced and, thus, fewer holes will be needed in a smaller grid:

$$N_h \sim \frac{D^2}{d_h^2} \sim \phi_n \frac{D^2}{L} \sim \phi_n L \quad (2.24)$$

It is, therefore, plausible that a small enough chamber could be built such as to require only one hole. Just for the purposes of illustration, one such design would consist of a 2 mm long chamber with a transparency ratio  $\phi$  of 0.2, the resulting hole size of 1 mm, and the corresponding chamber diameter of 2.3 mm.

As it was mentioned earlier, grid spacing does not scale photographically with the rest of the structure. A scaling relation for the grid spacing can be obtained by examining the current density limited by the effects of the space charge:

$$j \sim \frac{V^{3/2}}{d^2} \quad (2.25)$$

Since the current density  $j$  is proportional to the plasma density, which scales as  $1/L$ , at a given voltage  $V$  grid spacing varies as:

$$d \sim \sqrt{L} \quad (2.26)$$

indicating that the grid spacing becomes proportionately larger at small scale. This result is of no major consequence to the overall thruster design, other than the fact that it may alleviate some of the manufacturing difficulties associated with the production of grids in comparison to their larger counterparts for which grid separations are already on the order of 1 mm.

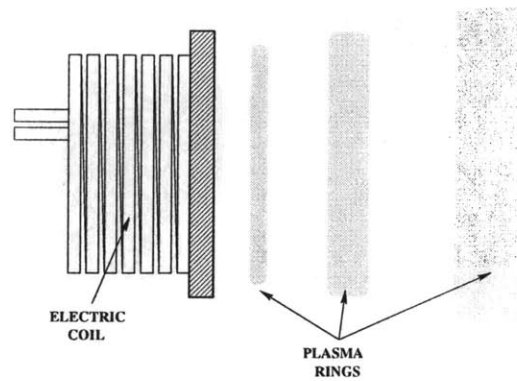


Figure 2-5: PIT schematic

## 2.4 Pulsed Inductive Thrusters

### 2.4.1 Principles of operation

High power Pulsed Inductive Thrusters (PITs) have been originally introduced in the 1960's, however, since then have not received much attention. PITs accelerate propellant away from its walls, hence, unlike miniature Hall and ion thrusters, PITs may not suffer from intensified erosion rates and degradation of life and, along with their controllability advantages could be promising for micro-satellite applications.

PITs operate by injecting puffs of gas over a coil which is subjected to a set of periodic current impulses (see Fig. 2-5). The time varying magnetic flux produces a circulating electric field within the gas causing an electrical breakdown to occur. The resulting plasma ring carrying electrical current is magnetically accelerated away from the coil producing thrust transmitted to the coil by reaction [5].

### 2.4.2 Loss mechanisms and scaling

Two major loss mechanisms have been identified in the operation of PITs - those due to shocks and those due to Ohmic losses in the plasma ring. Shock losses arise from the well-known "snow-plow" effect [5], whereby the region of gas located further away from the coil is unable to ionize as it is partially shielded by the self-field of the plasma ring created in close proximity to the coil. The ionized ring accelerates through the remainder of the neutral gas, resulting in heavy dissipation. Ohmic losses in the

plasma ring. on the other hand, arise due to the finite conductivity of the plasma. It has been shown in Ref. [5] that the characteristic thickness of the plasma ring scales in proportion to the square root of the thruster dimension, indicating that a thicker layer of gas can be ionized and accelerated as the size of the device is reduced. In fact, a device 1 cm in diameter would produce a plasma ring whose thickness is of the same order as the gas layer itself. It can, therefore, be argued that shock losses will have either minimal impact on the thruster performance or be completely eliminated at small scale. Ohmic losses, however, exhibit less desirable characteristics. These losses can be estimated by determining the ratio of the induced electric field due to the variation of magnetic flux in time to the electric field due to Ohmic resistance in the plasma:

$$R_m = \frac{E_i}{E_\theta} \quad (2.27)$$

The quantity  $R_m$  is known as the magnetic Reynolds number which indicates the relative importance of resistive losses in the induction-driven accelerators. The induced electric field generally scales with the motional EMF which is given by:

$$E_i = v_z B_r \quad (2.28)$$

where  $v_z$  is the velocity of the ring and  $B_r$  is the magnetic field, while the field in the plasma ring can be determined from:

$$E_\theta = \frac{j_\theta}{\sigma} \quad (2.29)$$

where  $j_\theta$  is the azimuthal current density in the ring and  $\sigma$  is the electrical conductivity of the plasma. The current density  $j_\theta$  can be determined from the Ampere's law:

$$\nabla \times \mathbf{B} = \mu_0 \mathbf{j} \quad (2.30)$$

or, written for the azimuthal component of the current:

$$j_\theta = \frac{1}{\mu_0} \frac{\partial B_r}{\partial z} \sim \frac{1}{\mu_0} \frac{B_r}{z} \quad (2.31)$$

Substituting the above relationships into the expression for  $R_m$  one has:

$$R_m = \mu_0 \sigma v z \quad (2.32)$$

The quantity  $z$  can be interpreted as a characteristic size of the plasma ring, while the electrical conductivity of the Coulomb dominated plasma is given by :

$$\sigma = \frac{e^2}{m_e c_e Q_{ei}} \quad (2.33)$$

The speed of the ring  $v$  which determines the  $I_{sp}$  of the device as well as the quantities appearing in the expression for  $\sigma$  are independent of scale. Since  $z \sim \sqrt{D}$ , where  $D$  is the characteristic size, the magnetic Reynolds number will decrease as the size of the device is reduced, resulting in the relative increase of Ohmic losses and degradation of efficiency. To put this argument in perspective, Ref.[6] reports a PIT (1 m in diameter) operating at an average power of 100 kW PIT (assuming 10,000 to 1 duty cycle) which has successfully demonstrated efficiencies on the order of 50 – 60% and an  $I_{sp}$  of 3,000 – 6,000 sec. The magnetic Reynolds number  $R_m$  for this device was on the order of 100, indicating that resistive losses were negligible in comparison to the operating power. On the other hand, a 1 cm device operating at 10 kW under similar conditions would yield a Reynolds number  $R_m$  on the order unity, indicating that a sizable fraction of the power coupled into the plasma by induction would be dissipated as heat. It is this intrinsic limitation of the induction devices in general that makes them impractical at power levels below about 10 kW.

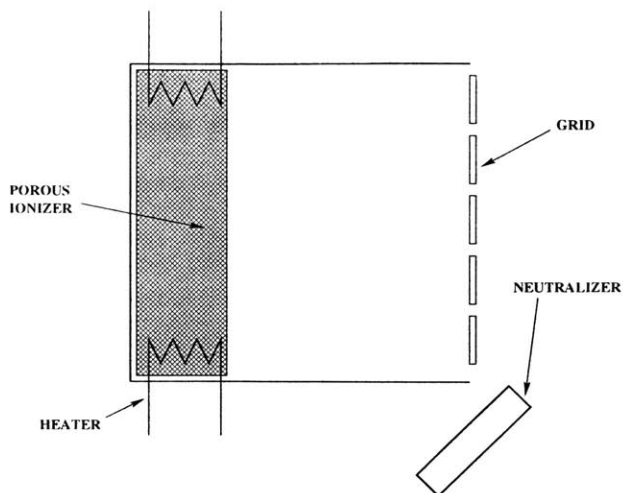


Figure 2-6: Schematic of a contact ionization thruster

## 2.5 Contact Ionization Thrusters

In the quest for a more durable device that could operate at low power yet provide sufficient operating life to be of practical interest, contact ionization thrusters were considered for miniaturization. They do not rely on collision-based ionization, hence do not require the usual increase in the plasma density to counter the reduction in size. Although erosion is intrinsically unavoidable, it is anticipated that these thrusters are less likely to suffer from quadratic decrease in operating life and, thus, become excellent candidates for miniaturization.

### 2.5.1 Principles of operation

It was originally proposed and later demonstrated by Langmuir that a heated surface of a metal with high electron work function  $\phi_e$  immersed in a vapor of an alkali metal, whose ionization potential  $\phi_i$  is lower than  $\phi_e$ , would convert some of the alkali atoms into positive ions. These ions can be electrostatically accelerated to high speeds producing thrust by reaction similar to the operation of a typical ion engine. The schematic of a contact ionization thruster is shown in Fig. 2-6.

Existing models of contact ionization thrusters normally consist of a porous tungsten ionizer heated to temperatures on the order of 1,200–1,400 K and utilize cesium as a working fluid. Any surface contamination lowers the work function of the ionizer and seriously impairs its ability to ionize the propellant. High ionizer temperatures

are, therefore, necessary to help evaporate alkali particles off of the surface and maintain adequate ion production in steady-state. Too high a temperature, on the other hand, enhances thermionic emission of electrons from the cesium absorbed on the surface, partially neutralizing some of the ions and reducing the resultant ion current density. This suggests the existence of an optimum operating temperature at which maximum ion current density can be extracted.

## 2.5.2 Scaling of contact ionization thrusters

Just as in the case of ion engines, the resultant current density extracted by the electrodes is limited by the space charge and can be modeled by the Child-Langmuir equation:

$$j_0 \sim \frac{V_0^{3/2}}{x_0^2} \quad (2.34)$$

where  $V_0$  is the extractor voltage and  $x_0$  is the spacing between the ionizer and the negative electrode. As the extractor voltage is first increased from zero, the current density follows the Child-Langmuir law until it asymptotes to a value dependent upon the ionizer temperature. Higher temperatures generally enhance cesium evaporation rates and yield larger saturated current densities as illustrated in Fig. 2-7. Since any accumulation of ions at the ionizer site would contaminate its surfaces and degrade utilization efficiency, it is desirable to operate these devices at the onset of saturation, i.e. at such voltages for which all or most of the ions produced by contact ionization are extracted in the steady state. Since the power extracted by the jet is proportional to the current density, it is desirable to keep the current density high so that the radiative losses remain a small fraction of the total input power. As expected, the major loss mechanism in contact ionization devices is thermal radiation from the heated ionizer surfaces. The radiated power is governed by the Boltzman radiation law which scales as:

$$P_{loss} \sim \sigma \epsilon T^4 L^2 \quad (2.35)$$

where  $T$  is the ionizer temperature and  $L$  is the characteristic thruster dimension. The useful power extracted by the jet in the form of kinetic energy can be determined

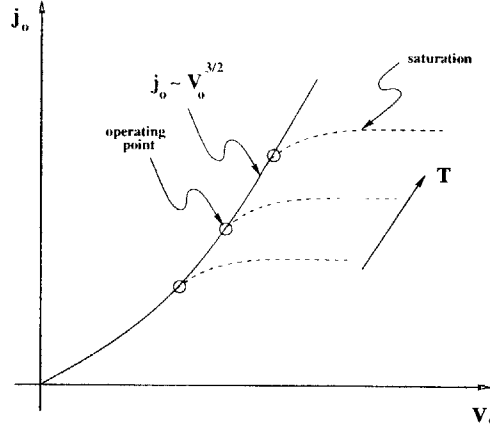


Figure 2-7: Current density vs. temperature for cesium-tungsten configuration

from the following relation:

$$P_{jet} \sim j_0(T)V_n L^2 \quad (2.36)$$

where  $j_0(T)$  is the saturated current density and  $V_n$  is the net accelerator voltage. Suppose that operation at constant voltage is desired. From Eqns. 2.35 and 2.36 it is clear that both the jet power and the radiative losses scale with  $L^2$ . Thus, their ratio and, therefore, the efficiency, will remain constant. However, since  $x_0$  must remain constant as well, in order to achieve the desired reduction in power the diameter of the device  $L$  must be reduced. The resultant device will become proportionately longer and thinner. Although the losses of ions to the wall in larger devices are generally negligible in comparison to the radiative losses, they may become significant for this disproportionately scaled configuration. The power lost to the wall scales as the product of the ion flux and the surface area of the side wall. Since the voltage remains constant, particle flux is proportional to the current density. Therefore:

$$P_{wall} \sim j_0(T)x_0 L \quad (2.37)$$

Clearly, the power lost to the wall falls off slower than the jet power with decreasing  $L$ , hence, it is possible that for sufficiently high aspect ratios  $x_0/L$  wall losses will dominate over the radiative losses and the efficiency will no longer remain constant.

An alternative scaling strategy is possible for which the aspect ratio is preserved, i.e.  $x_0 \sim L$ , however, the voltage is allowed to vary at a constant value of  $j_0$ . Intro-

ducing a scaling parameter  $f$  to indicate the reduction of operating power, such that  $f \sim j_0(T)L^2V_n$ , the operating voltage  $V_n$  can be expressed in terms of the operating power. Since  $j_0(T)$  depends only on the ionizer properties and is independent of scale, the extractor voltage  $V_0$  must scale as:

$$V_0 \sim L^{4/3} \sim f^{2/5} \quad (2.38)$$

The overall efficiency can now be evaluated as the ratio of the jet power to the total input power:

$$\eta = \frac{P_{jet}}{P_{jet} + P_{loss}} \sim \frac{1}{1 + \frac{\sigma\epsilon T^4}{j_0 V_n}} \quad (2.39)$$

Just as in the case of ion engines, in order to preserve the shape of the ion beam and maintain minimal beam divergence, the ratio of  $V_n$  to  $V_0$  must remain constant. In this case the efficiency would scale as:

$$\eta = \frac{1}{1 + \frac{\sigma\epsilon T^4}{j_0 V_0} \left(\frac{V_0}{V_n}\right)} \sim \frac{1}{1 + K} \quad (2.40)$$

where  $K$  scales as  $T^4/j_0 L^{4/3}$  or, alternatively as  $T^4/j_0 f^{2/5}$ . As the size of the device is reduced at constant  $j_0$  and  $T$ , the ratio of radiated (lost) power to the beam power is increased in proportion to  $1/f^{2/5}$ , indicating a reduction of efficiency at small scale. In order to evaluate the impact of these losses it is useful to examine some of the existing devices and compare their efficiencies to those obtained for the proposed smaller models operating at lower power. Ref. [7], for instance, supplies a detailed set of experimentally measured data for a cesium-operated linear contact ionization thruster. A thrust of 1.37 mN was obtained at an  $I_{sp}$  of 6,700 sec and the total input power of 105 W yielding an efficiency of 45%. Using the above definition for  $K$  this value of efficiency corresponds to  $K = 1.22$  indicating that radiative losses are of the same order as the useful power carried by the jet. Reduction of jet power by a factor of 10 would yield size reduction by a factor of 2 (from  $f \sim j_0 L^{10/3}$ ) with a disproportional increase of radiative energy losses corresponding to  $K = 3.07$  and the resulting efficiency of only 24%. Although the overall efficiency drops with the

reduction of power, specific impulse which scales with the square root of the applied voltage or, alternatively, as  $L^{2/3}$  or  $f^{1/5}$  yields a favorable decrease from 6,700 sec to 4,220 sec. Since many near-Earth missions of practical interest optimize at much lower values of  $I_{sp}$ , additional reduction of size and power would be desirable, however, any further miniaturization would result in unacceptable energy losses.

One possibility for mitigating such a dramatic drop in the efficiency is to reduce the operating temperature of the ionizer. Since radiative losses generally scale as  $T^4$  and, thus, are very sensitive to variations in  $T$ , it is conceivable that propellant utilization and  $j_0$  can be sacrificed to a limited extent for additional gain in the overall efficiency. It is expected, however, that under such circumstances the quantity  $T^4/j_0$ , which was previously assumed to depend only on the ionizer characteristics and remained invariant, could be reduced by a proper choice of operating temperatures and/or alternative ionizer configurations. As  $j_0$  is reduced from its optimum value, however, possible gains in the overall efficiency may be offset by the degradation of propellant utilization, eliminating any practical benefit of this approach.

It should be pointed out that although the efficiency of contact ionization thrusters does suffer at small scale, a 10-Watt device operating at 24 % efficiency is quite an attractive alternative in comparison to the existing PPTs, which can operate at similar power levels, yet demonstrate efficiencies of only 7-10 %. There is one drawback, however, which makes contact ionization thrusters inferior to many other technologies. The use of highly reactive and corrosive propellants, such as cesium, significantly complicates storage, handling, and operation of these thrusters on board of a spacecraft. A more detailed discussion of the handling issues can be found in the Summary section of this chapter.

## 2.6 Colloidal Thrusters

Colloidal thrusters are representatives of yet another technology of electrostatic accelerators which does not rely on ionization in the gas phase and, hence, their operating life is not compromised at small scale. In addition to their intrinsically small di-

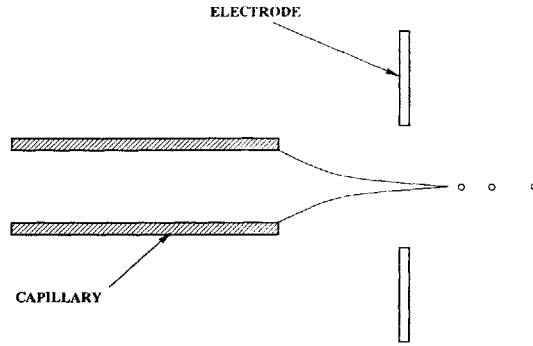


Figure 2-8: Colloidal thruster schematic

mensions and extremely low operating power levels, eliminating the need for further “miniaturization”, colloidal thrusters possess a number of desirable characteristics which make them attractive for a number of potential missions. Colloidal thrusters can be actively controlled to deliver precise impulse bits, they operate on non-corrosive fluids, and they do not produce plasma plumes, significantly simplifying integration of the propulsion subsystem with other critical spacecraft elements and components.

### 2.6.1 Principles of operation

Colloidal thrusters consist of a thin capillary tube which supplies a conducting fluid to its tip from an upstream reservoir. The fluid is usually held at a large positive potential with respect to an outside electrode creating a strong electric field at the tip of the capillary (see Fig. 2-8). Sufficiently high voltage applied between the two electrodes causes the fluid surface to become unstable and deform into a conical meniscus. A thin jet carrying charge on its surface forms at the tip of the meniscus and later breaks into small highly charged droplets. These droplets are electrostatically accelerated to high speeds and are neutralized by an external cathode producing thrust by reaction.

## 2.6.2 Applicability to micro-propulsion

Although the multitude of physical phenomena governing the operation of colloidal thrusters have been observed and studied since the beginning of the 20th century, colloidal thrusters have been actively pursued only in the 60s and 70s and since then have not received much attention up until recently. It was the inability to produce droplets with high enough charge to mass ratio and the resulting need for high voltages ( $\sim 10 - 100$  kV) that diverted the attention of engineers away from colloidal thrusters towards more accommodating alternative technologies. Recent modeling and experimental efforts, however, revealed that the desired low-voltage operation can be attained with a proper choice of fluid properties, capillary dimensions, and under suitable operating conditions. Although a more detailed analysis of colloidal thrusters can be found in the later chapters, for the purposes of identifying potential benefits and limitations and for the purposes of comparison to other propulsion technologies a brief overview of their performance will be presented here.

Charged droplets of mass  $m$  each carrying a positive charge  $q$  are produced by an unstable jet and are electrostatically accelerated to an exhaust speed  $c$  which can be determined from the conservation of energy:

$$c = \sqrt{\frac{2qV}{m}} \quad (2.41)$$

where  $V$  is the applied voltage between the capillary and the ground electrode. Clearly, in order to operate at sufficiently high values of  $I_{sp}$ , either high voltages or high values of  $q/m$  are required. A series of experimental studies in the past [8], [9], [10] have shown that for typical electrolyte solutions with electrical conductivities not exceeding 0.1 Si/m, charge to mass ratios were limited to values on the order of 200 – 400 C/kg. It was later observed [11], [12], [13] that certain viscous solutions with glycerol were capable of producing particles with extremely high values of the charge to mass ratio. The inability to produce high values of  $q/m$  in most other fluids required voltages on the order of 100 kV in order to achieve a competitive  $I_{sp}$  of 1,000 sec. More recent developments in the understanding of the mechanisms behind the

formation of the charged jet [14], [15], [16] indicated that the jet diameter and, hence, the droplet size were determined primarily by the flow rate and the electrical conductivity of the fluid. Specifically, it was verified, both experimentally and theoretically, that higher values of  $q/m$  could be achieved by using high conductivity solutions operated at sufficiently low flow rates. Recently conducted experiments using solutions of various inorganic salts dissolved in formamide [17] have demonstrated that droplets with  $q/m$  values of over 5,000 C/kg could be produced. Even with such a significant improvement, voltages on the order of 10 kV were required. Further experimentation revealed that it was possible, under certain conditions, to reduce the jet diameter to a point where ions with charge to mass ratios significantly larger than those of droplets ( $\sim 240,000$  C/kg) could be extracted directly from the tip of the meniscus. In combination with slowly moving droplets, such a mixed-regime operation would enable one to “dial in” any desired value of  $I_{sp}$  by a proper choice of the relative proportions of ions to droplets. Although low-voltage operation can, indeed, be achieved for large enough values of the mean charge to mass ratio, it should be noted that there still exists a lower bound on the applied voltage required to initiate the emission of the jet. This voltage is such as to electrostatically overcome the surface tension of the meniscus formed at the tip of the capillary. This threshold voltage can be estimated by equating the surface tension of an idealized spherical meniscus to the electrostatic traction at the surface:

$$V_{min} = \sqrt{\frac{\gamma R}{\epsilon_0}} \quad (2.42)$$

where  $R$  is the radius of the capillary, and  $\gamma$  is the surface tension coefficient. It can be seen from the above equation that the minimum startup voltage depends only on the size of the capillary and can be made sufficiently small if so desired. Using surface tension for formamide of 0.05 N/m and a 0.5 mm capillary the minimum startup voltage comes out to be on the order of 2,000 V. The relationship for the minimum startup voltage in Eqn. 2.42 is only approximate as it ignores the effect of external electrodes and assumes a simplified spherical profile for the fluid meniscus. A quantitatively more precise analysis of this phenomenon is presented in Chapter 5.

Although the mixed regime offers a great deal of flexibility, it does come at an expense. As in any other propulsion device, an exhaust jet containing two distinct species moving at different speeds is a suboptimal arrangement. More energy is spent accelerating particles with higher  $q/m$  than the extra thrust derived from them. This leads to the degradation of an otherwise very high efficiency. For the previously quoted values of  $q/m$ , i.e. 6,000 C/kg for droplets and 240,000 C/kg for ions, the maximum dip in the efficiency due to the polydispersity in the mixed-regime mode is about 48 %. Considering their additional advantages, even in this worst-case efficiency scenario, colloidal thrusters remain quite attractive in comparison with other competing technologies. It should be noted that in the above configuration, such colloidal emitters each operate at  $mW$  power levels and produce thrust on the order of a fraction of a  $\mu N$ . It is, therefore, intrinsic in the nature of these devices that the majority of missions would require multi-needle arrangements or clusters of up to 100 – 10,000 individual emitters.

## 2.7 Field-Effect Electrostatic Propulsion (FEEPs)

Field-Effect Electrostatic Propulsion (FEEPs) is an offspring technology very similar to that of colloidal thrusters. The main distinction between the two is that FEEPs utilize as propellants easily ionizable liquid alkali metals instead of organic solvents. Unlike colloidal thrusters, due to the emission of pure ions and the use of liquid metals with high surface tension coefficients, FEEPs generally operate at extremely high values of  $I_{sp}$ .

### 2.7.1 Principles of operation

FEEPs typically consist of a narrow slit in which liquid metal propellant (Cs, In, or others) is supplied via capillary forces. The electrode configuration of the FEEP is similar to that of a typical colloidal thruster. A large number of conical protrusions form along the slit length due to the applied electric field. Because of the very high conductivities of liquid metal propellants, the tip of each protrusion usually reaches

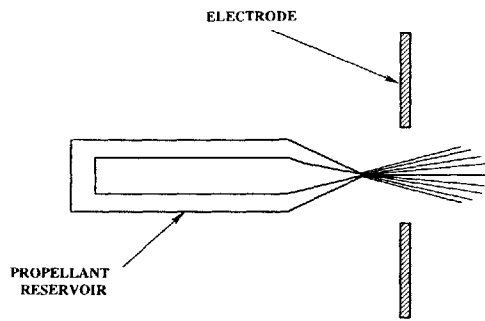


Figure 2-9: FEEP schematic

atomic dimensions ( $\sim 0.5$  nm) and ions are extracted directly from the surface of each tip by field emission. These ions are accelerated and then externally neutralized just as in the case of colloidal thrusters (see Fig. 2-9).

### 2.7.2 Applicability to micro-propulsion

Due to the high values of surface tension coefficients for liquid metals, the minimum startup voltages for FEEPs are generally a factor of three larger than those for colloidal thrusters with similar capillary dimensions. Voltages on the order of 10 – 15 kV have been reported by the ESTEC electric propulsion laboratory which has developed a liquid metal emitter with an  $I_{sp}$  of 6,000 sec delivering a thrust of 0.3 mN/cm [18]. Due to their large specific impulse, the amount of propellant required for typical FEEP missions is small enough to be stored within the emitter structure eliminating the need for a separate feed system. Although high values of  $I_{sp}$  are generally preferred due to the significant savings in the propellant usage, too high a specific impulse may offset these savings because of the need for heavier power processing equipment. Ref. [18] reports the power to thrust ratio obtained for the experimental liquid metal emitter of 55,000 W/N, over an order of magnitude larger than that for the proposed mixed-mode colloidal thruster. The main disadvantage of FEEPs, however, is the use of highly reactive elements requiring complex storage and handling procedures. Additionally, the use of liquid metals on board of a spacecraft presents a number of integration challenges ranging from possible corrosion of critical spacecraft

components to deposition of liquid metals onto sensitive optical elements.

## 2.8 Summary

This section contains a summary of the main advantages and disadvantages of the individual propulsion systems emphasizing miniaturization and scalability as presented in the prior parts of this chapter. The summary is followed by a recommendation to pursue a specific technology or technologies which demonstrate superior performance and handling qualities at small scale.

### 2.8.1 Hall thrusters

The analysis of Hall thrusters has indicated that they are capable of efficiently operating at low power levels provided that sufficient electron confinement can be maintained by increasing the strength of the magnetic field. It has also been shown that their operating life suffers at small scale due to the combined effects of the increase in the plasma density and the reduction of component dimensions. Although a proper choice of the materials and magnetic circuit configurations may offset the detrimental effects of erosion, the operating life of any device in which ionization relies on collisions can be seriously compromised with the reduction in size. Since the overall weight of the power and propulsion subsystem will dominate over the weight of the individual thrusters at small scale, it is conceivable that the loss of life could be partially offset by the use of redundant thrusters. In such a redundant configuration, a need may arise for short-term near-Earth missions in which low-power Hall thrusters would find their use. Overall, however, a combination of high efficiency, optimal range of  $I_{sp}$ , and their relative simplicity in comparison to the rival technologies (such as ion engines) make Hall thrusters one of the top candidates for miniaturization.

### 2.8.2 Ion engines

A mature technology which is very similar to Hall thrusters, ion engines can also maintain high efficiency at small scale. Scaling of ion engines is mainly limited by the inability to confine electrons within the ionization chamber. Currently existing high power ion engines already utilize high-field permanent magnets with the strength in excess of 0.5 – 1 T. Although the reduction in size would force the electrons to reside disproportionately closer to the magnets, together with the proper placement of the anode with respect to the magnetic field lines, these modifications may permit additional decrease in size. Detailed numerical modeling, however, is necessary to assess potential benefits of these changes. Since ion engines do not rely on the closed drift of electrons, they are readily reconfigurable to a linear geometry. In this configuration, linear ion engines can be microfabricated using standard etching techniques, significantly reducing manufacturing and assembly costs. The main disadvantages of ion engines in comparison to Hall thrusters are the increased complexity of the power delivery system and the need for a set of grids presence of which may exacerbate the lifetime issue even further. In their standard configuration, ion engines require two power supplies for the grids, two power supplies for the ionization chamber (one for the cathode filament, one for chamber discharge) and another power supply for the neutralizer. A combination of high specific impulse on the order of 3,000 sec which may be suboptimal for many near-Earth applications, additional development effort necessary to reconfigure existing magnetic confinement schemes, and their additional complexity, all make ion engines inferior to Hall thrusters.

### 2.8.3 Pulsed inductive thrusters

It was shown earlier in this chapter that pulsed inductive thrusters, although less susceptible to erosion, suffer significant losses in efficiency due to the decrease in the magnetic Reynolds number with scale. It was demonstrated that although shock losses are almost entirely eliminated at small scale, Ohmic losses in the plasma ring become proportionately more significant and are detrimental at power levels below

about 10 kW. It is, therefore, recommended that pulsed inductive thrusters be eliminated from further consideration.

#### **2.8.4 Contact ionization thrusters**

The analyses of the two scaling alternatives for contact ionization thrusters both indicated a degradation of efficiency at small scale. In the case of the operation at constant voltage the resultant loss in efficiency was shown to be due to the increased losses of ions to the wall, while scaling at constant aspect ratio yielded increased energy losses due to the relative decrease of kinetic energy carried by each ion in comparison to the energy needed to create one. The latter result was shown to be due to the radiative losses per unit area which remained constant under scaling, while the jet power per unit area was decreased at small scale. In spite of the reduced efficiency, contact ionization thrusters still remain competitive at power levels on the order of 5-10 W and offer performance superior to that of the conventional PPTs in this power range. Contact ionization thrusters, however, operate at very high values of  $I_{sp}$ , are very susceptible to surface contamination, and require stringent handling and operational precautions. Lastly, contact ionization thrusters utilize reactive liquid metal propellants which can potentially contaminate critical spacecraft elements or deposit onto sensitive optical instruments. Considering the numerous operational disadvantages, contact ionization thrusters do not appear attractive at this time and, therefore, will not be pursued any further.

#### **2.8.5 Colloidal thrusters**

Colloidal thrusters represent a unique technology which is already miniature by its nature. It has been shown that these thrusters can operate over a wide range of  $I_{sp}$ , generally at very high efficiencies. Colloidal thrusters do not suffer from degradation of life and can operate on non-reactive and non-corrosive propellants eliminating a number of operational issues, specifically the plume interactions with sensitive spacecraft components. Although the physics of colloidal thrusters is not yet well understood,

considering the performance advantages and flexibility that colloidal systems offers, it is recommended that the physics of colloidal thrusters be studied further to enable fabrication and testing of these devices in the future.

### **2.8.6 Field-Effect Electrostatic Propulsion**

FEEP technology is very similar to that of colloidal thrusters, yet it falls short on a number of important aspects. FEEPs normally require very high voltages and, therefore, operate at extremely high values of  $I_{sp}$  optimal only for long-term and propulsion-intensive missions. Just as in the case of contact ionization thrusters, FEEPs utilize liquid metal propellants, thus posing similar concerns with regards to spacecraft interaction. In addition, due to the insignificant propellant usage, most of it is generally stored within the exposed emitter structure, requiring a complex pre-launch procedure in which the thrusters are completely sealed and frozen for the duration of the atmospheric flight. It is for these numerous disadvantages, that FEEPs do not appear to be attractive and will no longer be pursued.

### **2.8.7 Recommendations**

Based on the above observations, it can be concluded that of the several technologies that were examined, Hall thrusters and colloidal thrusters seem most promising for micro-satellite applications. It is the objective of the remaining chapters of this work to, first, elaborate on the development and testing of a miniature Hall thruster, and, second, to present models of the different aspects of physics of a colloidal emitter: a detailed semi-analytical fluid model of a cone-jet and a simplified numerical electrostatics model predicting the formation of the jet.

# Chapter 3

## Design of a 50W Hall Thruster

### 3.1 Introduction

It was concluded, based on the scaling laws presented in Chapter 2 that a typical Hall thruster can be scaled down in power level and efficiently operated in the  $I_{sp}$  range between 1,400 – 1,600 sec provided that the magnetic field strength can be increased and the size of the device reduced, both in the same proportion. Although the final design of the thruster evolved towards a somewhat different configuration, the initial design parameters were estimated by scaling from a ceramic-based 1.35 kW SPT-100 Hall thruster. This particular model has been experimentally optimized and has undergone extensive performance and lifetime evaluations in the past and was selected because of the readily available performance data. The scaling factor was chosen to be roughly 27. This scaling ratio corresponds to the power level reduction from 1.35 kW to about 50 W - power level suitable for many envisioned micro-satellite applications. Such a reduction in scale also corresponds to the upper limit of the maximum strength of the magnetic fields attainable with the strongest existing permanent magnets. The proposed design, therefore, falls near the low end of the achievable reduction in power while still obeying the scaling laws discussed in Chapter 2. The summary of the micro-thruster specifications based on this scaling is presented in Table 3.1.

Parameter	SPT-100	mini-SPT
Power, $W$	1350	50
Thrust, $mN$	83	3
Specific Impulse, $sec$	1600	1600
Efficiency	50	50
Channel Diameter, $mm$	100.0	3.7
Flow Rate, $mg/sec$	5.0	0.2
Magnetic Field, $T$	0.02	0.5

Table 3.1: Scaled Design Parameters

## 3.2 General Design Considerations

A Hall thruster in its standard configuration consists of a magnet, an insulated plasma channel, an anode, a propellant feed system, and a hollow cathode. Often, the plasma channel is thermally insulated from the surroundings by a layer of high-temperature ceramic that protects the magnets and other components from excessive heating. However, because of the larger heat fluxes involved, internal temperatures may exceed those imposed by the material limitations. By leaving a vacuum gap between the insulator and the body of the thruster, heat fluxes from the channel can be significantly reduced and limited to those mainly due to thermal radiation (refer to Appendix B for details on vacuum insulation). The manufacturing of a tiny ceramic channel that would have to withstand high temperatures and be resistant to thermal shock, however, may prove to be extremely complicated. For this reason, it was decided to abandon the idea of using an insulator at all. Hall thruster configurations manufactured without an insulator do exist. They are commonly known as thrusters with anode layer (TAL). In order to mimic the design of existing TALs, the anode was extended further into the channel and used to conduct all of the heat generated at its tip through the thruster body out to the surroundings.

In the TAL configuration, its bare metallic walls are usually kept at the cathode potential thus repelling electrons trapped by the magnetic field near the exit of the channel. Although the physics of the near-wall processes in the TAL is somewhat different from that of the SPT, performance characteristics of the two thrusters were

reported to be almost identical.

### 3.3 Magnetic Circuit Design

As it was shown in Chapter 2, the use of electric coils to achieve the required strength of the magnetic field at small scale is impractical due to the excessive Ohmic heating and the inability to dissipate heat by conduction. A different approach is to abandon the idea of using electric coils in favor of permanent magnets. Although a number of advantages make them ideal for this application, there is one drawback. Scaling of the thruster components leads to a significant reduction in the overall radiative surface area causing larger heat fluxes, and as a result, potentially, higher temperatures. The maximum allowable temperatures, however, are limited due to the possible loss of magnetization dictated by the Curie point of the specific magnetic alloys. It is necessary, then, to provide for adequate heat escape paths, presence of which substantially complicates both the design and the manufacturing process. Startup problems are possible due to the existence of a strong magnetic field that may prevent the electrons from entering the channel to initiate ionization during ignition. Lastly, an increase in the required magnetic field strength poses a question of feasibility of using permanent magnets of reasonable size for this application. The analysis of a magnetic circuit utilizing permanent magnets is discussed next.

A single shell of permanently magnetized material can be used to achieve the required magnetic field, which was estimated to range anywhere between 0.3 – 0.5 Tesla within the gap (see Table 3.1). A simplified analysis was done for preliminary assessment and comparison of the possible circuit geometries and materials to be used for construction. Assuming a uniform cross-section with infinite core permeability, Ampere’s law around the loop yields:

$$H_m d + \frac{B_m g}{\mu_0} = 0 \tag{3.1}$$

where  $H_m < 0$  is the magnetic field and  $B_m$  is the magnetic induction within the

magnet. A linear approximation to the magnetization curve for a given magnetic material can be written in the form:

$$B_m = \frac{B_0}{H_0} H_m + B_0 \quad (3.2)$$

where  $H_0 > 0$  and  $B_0$  are the coercive force and the magnetic remanence respectively. Eliminating  $H_m$  between the two equations yield an estimate of the resultant magnetic field within the gap.

$$\frac{B_m}{B_0} = \frac{1}{1 + \left(\frac{g}{d}\right)\left(\frac{B_0}{\mu_0 H_0}\right)} \quad (3.3)$$

The gap width is limited by the channel opening while the ratio  $g/d$  is a fixed parameter independent of scale. Thus, in order to achieve the required magnetic field strength, the material of choice would have to possess the following characteristics:

- $B_0 \approx 0.7 - 1.0$  Tesla
- Small  $B_0/H_0$ ,  $\rightarrow$  high coercivity ( $H_0$ )

In addition, the material is required to withstand elevated temperatures without significant loss of magnetization. Only three magnetic alloys were identified to meet the above specifications out of a wide variety of currently available magnetic materials. Both *NdFeB* and *Alnico* magnetic alloys possess excellent magnetic properties. However, *NdFeB* has low Curie temperature ( $\sim 350^\circ C$ ) and most *Alnico* alloys have low coercivity. *SmCo* alloys, on the other hand, with their high coercivity (9,000 Oersts) and high maximum operating temperature of  $275^\circ C$  (Curie point of  $750^\circ C$ ) were found to be optimal for this application.

Attention was paid in the design to the magnetic field profile within the gap. The goal was to prevent any electrons emitted by the cathode from entering the channel and diffusing towards the anode. This imposed a constraint on the field profile so that the adjacent field lines be everywhere tangent to the anode frontal surface. This configuration would also prevent the ion beam from deflecting either away or towards the center of the channel. Such a deflection may be a result of non-uniformities in the electric field caused by the presence of electrons trapped in the magnetic field. Two-

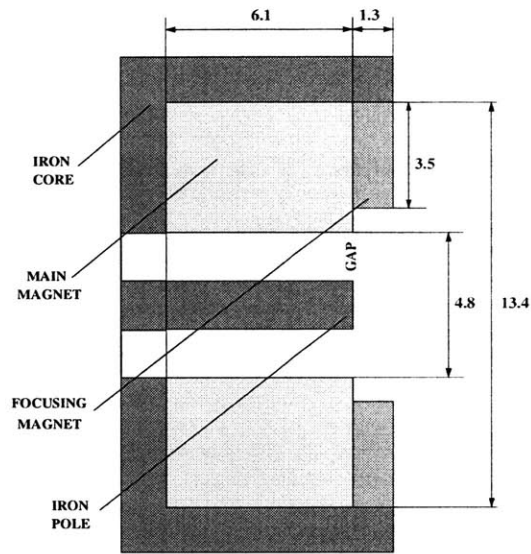


Figure 3-1: Magnetic circuit geometry (all dimensions in *mm*)

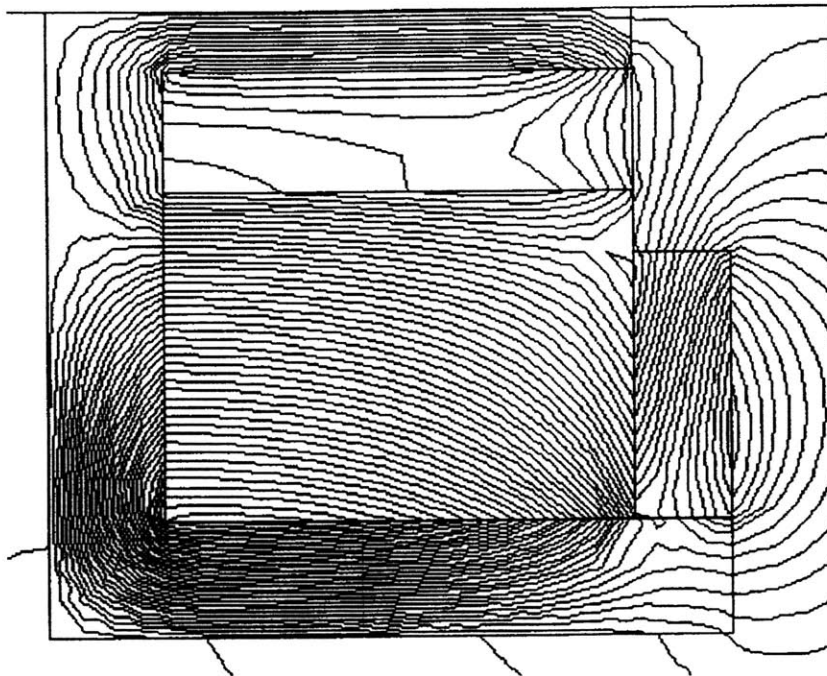


Figure 3-2: Magnetic flux profile (courtesy of Dexter Magnetics)

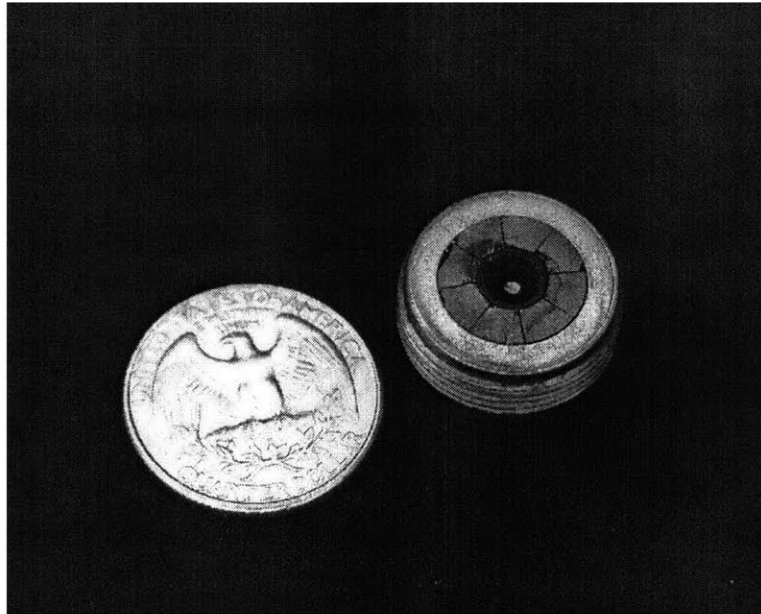


Figure 3-3: Magnetic circuit assembly

dimensional numerical magnetic computations were run for several configurations of the proposed geometry one of which is schematically shown in Fig. 3-1 (simulation courtesy of Dexter Magnetic Materials Division). Two SmCo permanent magnets were used in the design of the magnetic circuit. One of the magnets is shaped in the form of an axially polarized cylindrical shell which is the main “driving magnet”. The second one, consisting of eight arc segments, is polarized radially in the direction perpendicular to the polarization of the main magnet. It is used to force the flux into the gap and to shape the field lines so as to meet the profile specifications. Propellant and power feed lines were inserted into the channel via four circular holes in the back side of the iron core. The iron return path was designed to extend all the way around the main magnet to reduce the flux leakage out of the circuit and to help directing the flux into the segmented magnet (see Fig. 3-2) The attained values of the magnetic field strength in the gap for the final geometry were numerically estimated to range between 0.4 – 0.6 Tesla at the maximum operating temperature of  $250^{\circ}C$ , thus meeting our specifications. The top view of a completed magnetic assembly is shown in Fig. 3-3 (after 5-6 hours of operation).

### 3.4 Thermal Design/Material Selection

The two mechanisms for evacuating heat from solid components (anode, magnets, etc) are radiation and conduction. The resulting equilibrium temperatures depend on which of the two mechanisms predominates. The heat deposition rate per unit area scales as power/area  $\sim 1/L$ . The radiative cooling rate per unit area is given by  $\epsilon(T)\sigma T^4$ , and is independent of scale if  $T$  is successfully maintained. Thus, if radiation dominates, the wall temperature would increase roughly as  $1/L^{\frac{1}{4}}$  (a significant problem for small  $L$ ). The conductive cooling rate per unit area is  $k\Delta T/l$ , where  $l$  is some thickness, hence, this cooling rate scales as  $1/L$ , the same way as the deposition rate. Therefore, if heat conduction is dominant, wall temperatures can be kept invariant upon scaling and high temperatures within the channel and at the anode can be avoided by designing adequate heat conduction paths from the channel out to the surroundings. Since the anode is kept at a positive potential with respect to ground, it is virtually impossible to maintain direct contact of the anode with an external heat sink. Instead, the anode along with its electrical leads can be designed as a dual-purpose device. The propellant feed lines that normally supply gas to the anode can be used to conduct heat generated inside the channel towards the back of the thruster. Using for the back support structure a material which is a good electrical insulator as well as a good thermal conductor, the heat can be transferred to the surrounding metal, maintained near ambient temperature. From the materials standpoint, a heat-conducting ceramic such as  $BN$  or  $AlN$  would be most appropriate. Although  $AlN$  has a higher thermal conductivity, it is harder to machine, hence  $BN$  was selected.

Another important aspect from the materials standpoint is the design of the anode. A simple one-dimensional thermal model has shown that the anode tip temperatures would not exceed  $1,300\text{ }C^{\circ}$ . The analysis was carried out under the assumption that all of the heat generated at the anode is allowed to be either radiated to the magnets or conducted through the gas-feed lines towards the back of the thruster where it is rejected to the surroundings. Since the heat generated inside the channel

arises mainly due to the thruster inefficiency, roughly 25 W of the total power would be deposited as heat to the walls. Localized heating due to the impinging ions was neglected in this simple model. The details of the model and the results are presented in Appendix B.

The analysis has shown that conduction through the feed lines is the dominant mechanism of heat rejection. In addition, because of the large contact area in the back of the thruster, the temperature of the magnet surrounding the anode remains close to ambient. Therefore, the material of choice for both the anode and the feed lines would need to have the following characteristics:

- High thermal conductivity to ensure adequate heat rejection rate by conduction
- High surface emissivity to enhance heat rejection by radiation
- Adequate melting point ( $T_m > 1700\text{ }C^\circ$ ), compatible with the limiting values predicted by the model
- Easily machinable

Although refractory materials such as *W*, *Ta*, or *Mo* seem to best fit this category, the intricate shapes of such small dimensions are extremely hard to machine out of pure metals. Alloys of these refractories with copper, nickel, or iron, although more ductile, have melting temperatures that are below the acceptable limits and, therefore, would not be appropriate for this application. A platinum anode was used in the first model of the thruster, however, excessive arcing and exposure to high temperatures have damaged the anode tip over the course of the first few hours of operation. The second generation anodes were made out of molybdenum, as it is an excellent heat conductor with the melting point of  $2700^\circ C$ , hence providing more than a sufficient margin for the envisioned application. The final design schematic and a photograph of the manufactured anode are shown in Figs. 3-5 and 3-4 respectively.

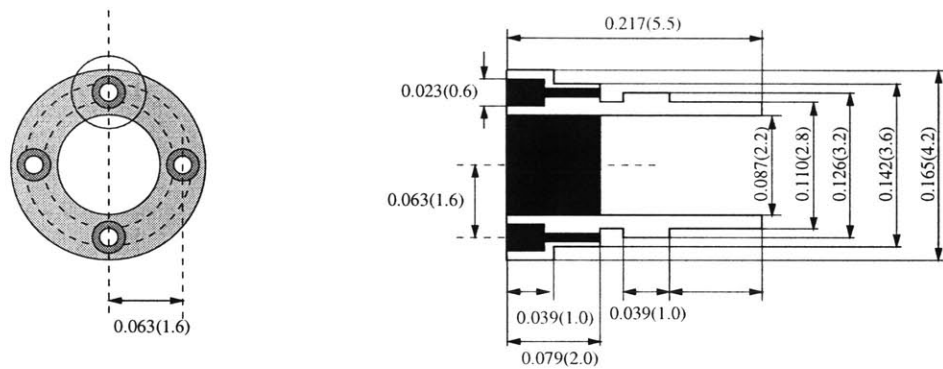


Figure 3-4: Anode schematic [all dimensions in inches (mm)]

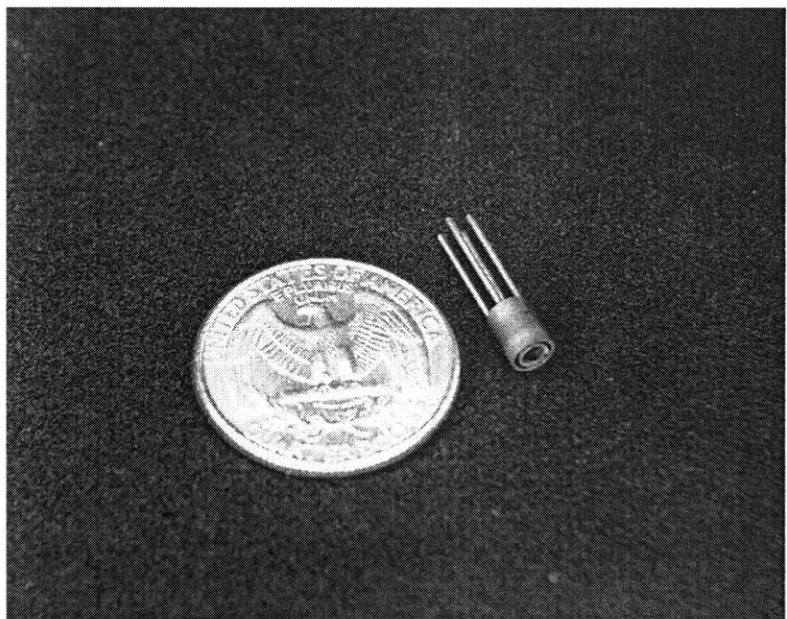


Figure 3-5: Anode

## 3.5 Cathode Design

Due to the lack of a suitable low-power cathode, several options were considered and experimentally evaluated. Although the new generation of field-effect (cold) cathodes seems to be promising for this application, no state-of-the-art technology exists for their use at this time. Hollow cathodes, conventionally employed in the SPTs, do not easily conform to the photographic scaling, yet they do have some potential for being miniaturized for this application. Thoriated tungsten filaments coated with barium oxide were used in the preliminary tests because of their ease in handling and operation. The main disadvantage of such filaments is that they consume a great deal of power ( $50 W/cm^2$ ) because of the need for high temperature to initiate thermionic emission. In addition, emission of coated filaments deteriorates quickly over time as the brittle coating cracks and falls off due to thermal expansion of the filament. Materials with lower electron work-function, such as  $LaB_6$ , would be more suitable for this application, however, they require special handling during operation and many deteriorate when exposed to the atmosphere. A hollow cathode was utilized in the most recent experiments. Refer to Sec. 4.1.3 for details. The optimal choice of a cathode for this thruster is a subject for further studies.

## 3.6 Final Design

The final version of the miniaturized Hall thruster is schematically shown in Fig. 3-6. The anode is designed as a hollow concentric channel with a flow buffer to achieve uniform azimuthal jet distribution. The four capillaries attached to the anode deliver the propellant from a gas distributor region located in the back of the assembly to the plasma channel. The frontal cap (made out of stainless steel) is a structural component that presses the magnets together with the protective molybdenum ring into the iron assembly and holds them in place during operation. Ceramic inserts are used to support the anode and improve its alignment with respect to the iron core. The anode assembly including the four ceramic inserts, the flow distributor,

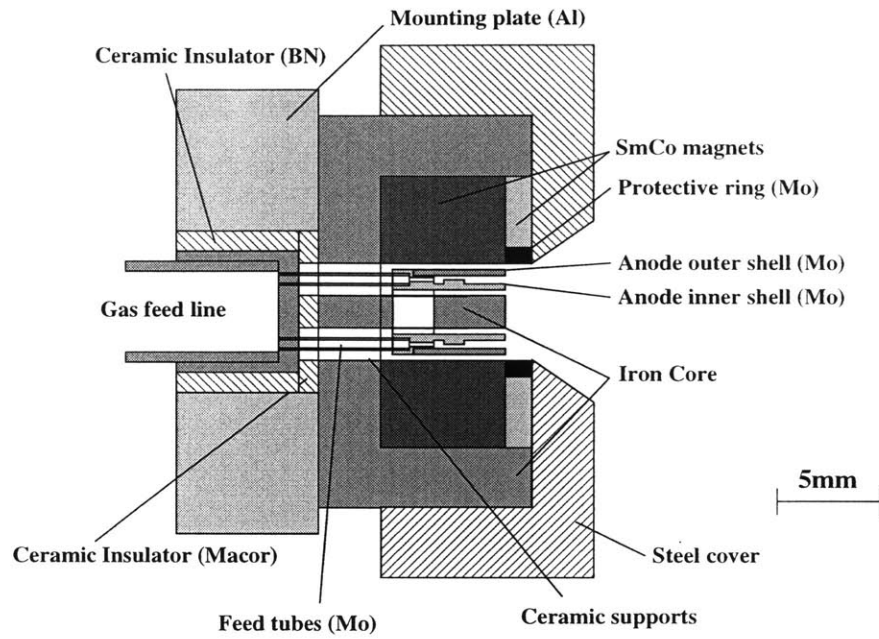


Figure 3-6: Final design schematic

and the insulators are shown in Fig. 3-7. A complete thruster assembly (excluding the propellant feed tube and the anode) is shown in Fig. 3-8.

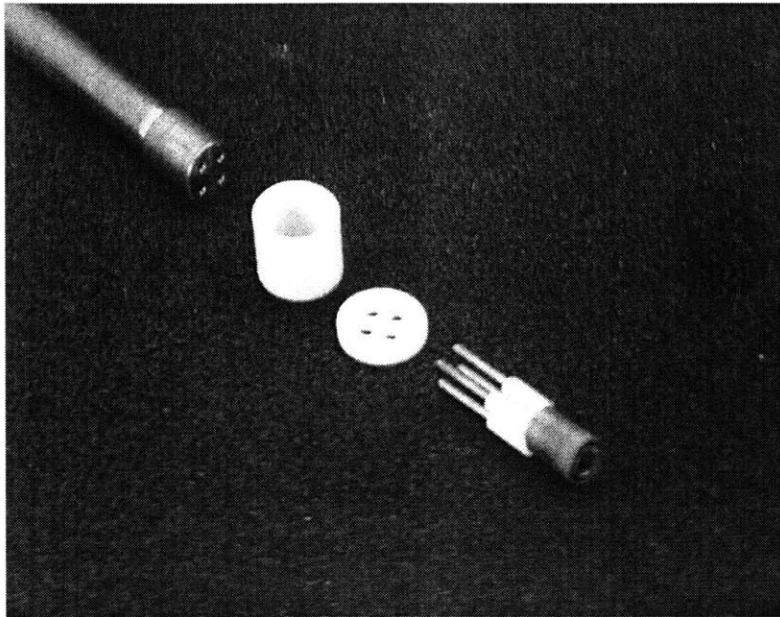


Figure 3-7: Anode assembly

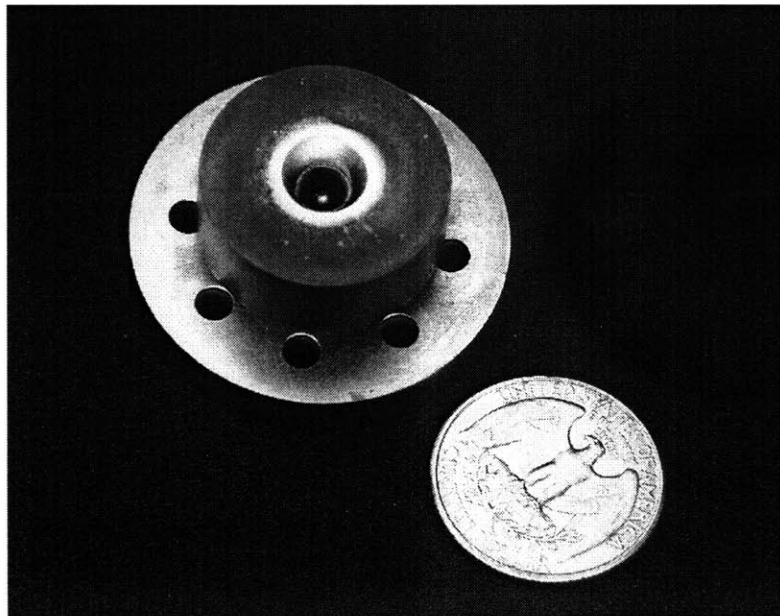


Figure 3-8: Final assembly

# Chapter 4

## Experimental Testing of a 50-Watt Hall Thruster

### 4.1 Preliminary testing attempts

Preliminary operational tests using Argon were first performed at MIT in a small bell-jar vacuum facility ( $\sim 0.2$  cu. meters) equipped with single mechanical and a diffusion pumps. Several cathodes were tested to achieve stable thruster operation at the designed nominal flow rate. A number of thin tungsten filaments extracted from regular incandescent light bulbs were used first. However, occasional arcs to the filaments destroyed them within seconds of operation. These thin pre-made cathodes were later replaced by a thicker 0.25 mm thoriated tungsten wire wrapped into a coil and supplied with heating current on the order of 10 Amps. Not only did these filaments consume and radiate a great deal of power (100-150 Watts), they also failed to provide sufficient electron emission to maintain stable thruster operation and created excessive arcing to the thrust stand resulting in periodic pulsations of the thruster discharge. These filaments also became extremely brittle after their first use and had to be often replaced. After a number of unsuccessful trials, a 0.25 mm molybdenum wire coated with barium oxide was shown to provide sufficient emission for the thruster to operate for extended periods of time. Although these cathodes eliminated arcing to the thrust stand and facilitated stable thruster operation, thermal cycling

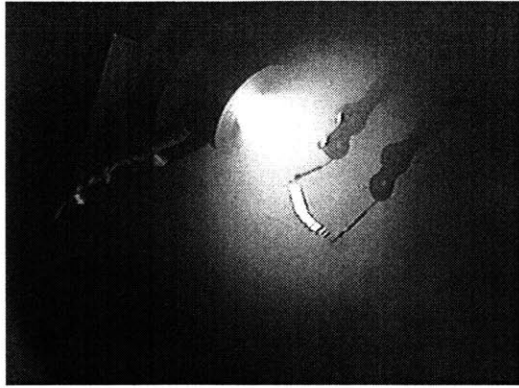


Figure 4-1: Operational testing

of the filament damaged the brittle coating over time and the filaments had to be replaced or re-coated after each test run. The micro-Hall thruster is shown in operation in Fig. 4-1 (note the heated filament in the foreground). No thrust measurements were obtained at the time due to the lack of a sensitive micro-balance. Subsequent experiments with Argon were performed at the Electric Propulsion Laboratory of the Edwards Air Force Base, CA. A heated filament made out of molybdenum and coated with barium oxide was used as a cathode. The thrust was measured using a horizontal arm balance at two different flow rates as a function of the operating voltage ranging between 200 and 300 V. A digital flow controller (Omega Inc.) was used to supply the necessary flow rate. However, because of the operation at the bottom of its nominal scale, flow rate measurements taken during the tests were not repeatable and the performance figures could not be reliably determined. In addition, although the thrust signal usually stabilized within the first few seconds of operation, the anode current never reached a steady value and, in most cases, kept increasing in time. To avoid overheating the thruster by passing excessive currents through the anode, test runs were limited in duration to under two minutes each.

A sensitive micro-balance (based on the inverted pendulum design [19]) was assembled and installed into the AstroVac facility at the Gas Turbine Laboratory, MIT. Extensive tests of the balance have shown that the thrust signal obtained by sampling the output of a linear variable differential transformer was corrupted by noise due to the coupling with the surrounding plasma. The spurious output of the position sen-

sor with the thruster operating at nominal conditions on a fixed platform exceeded that of the expected thrust levels. Numerous attempts were made to shield the signal cables and remove any existing ground loops in the detector circuitry. Although the noise levels in the output signal were generally reduced by proper grounding, changes in operating conditions, thruster location, and cable orientations had an unpredictable effect on the signal and, as a result, no reliable thrust measurements could be obtained.

Follow-up tests were performed at the Busek Co., MA using a thrust stand identical to the one assembled at MIT [19]. A hollow cathode manufactured by Busek Co. was used in the experiments. The lack of interference with the plasma has not been experimentally verified. However, during operation the thrust signal and the current both drifted significantly over time. Such behavior was inconsistent with the earlier observations made at the Edwards AF Base in which the thrust signal usually stabilized within the first few seconds of operation. Due to the lack of available run time at the facility, the issue of the drift in the thrust signal has never been completely resolved and could be attributed to either the thrust stand (thermal drift) or the thruster itself. Occasional shorting of the anode to the thruster body was also observed, often resulting in the need to vent the chamber, clear the spacing between the anode and the magnets of any trapped magnetic particles, and adjust the relative positions of the anode with respect to the center pole piece.

Further tests were attempted again at the Edwards Air Force Base, CA on a modified version of the thruster. The modifications included electro-plating the magnets with nickel to prevent crumbling and the inclusion of the new ceramic standoffs for the anode to facilitate better alignment with respect to the center post. In addition, the anode previously made out of platinum was this time machined out of molybdenum which has higher thermal conductivity and higher melting point than platinum. Although the new measures to improve alignment and eliminate crumbling significantly reduced internal arcing during operation, manufacturing and assembly imperfections of the magnetic components resulted in the failure of the magnets to hold in place. As a result of the reduction in the magnetic field strength and the increase in the

electron leakage, the observed anode currents were three to four times the nominal design value even at the relatively low voltages on the order of 100-150 V. The test runs were limited to under a minute each due to the excessive heating of the thruster assembly and were soon terminated after the realization that the segmented magnets were no longer held together.

After a number of unsuccessful attempts to test the micro Hall thruster conclusive results were finally obtained at a vacuum tank facility of the Plasma Propulsion Laboratory at Princeton University. Brief descriptions of the facility and the diagnostics equipment are provided below.

## 4.2 Testing Facility

### 4.2.1 Vacuum Tank

The vacuum tank was equipped with two mechanical roughing pumps and a single diffusion pump. In addition, a copper baffle cooled with liquid nitrogen was operated throughout the duration of the tests. At the nominal Xenon flow rate of 2 sccm and the cathode flow rate of 1.4 sccm the steady state chamber pressure did not exceed  $5 \times 10^{-5}$  torr. Although such background pressures may be considered marginal for testing larger devices, favorable scaling of particle densities at small size make these pressures more than adequate for micro-thruster testing. The chamber was equipped with a number of gas and electrical ports, thus allowing all of the monitoring and control circuitry for the thrust balance, power supplies, and the flow controller to be positioned outside of the vacuum tank. Main power to the thruster was provided by a 300 Volt - 5 Amp DC power amplifier. Two additional supplies were used to power the cathode - one to heat the filament and one to maintain the keeper current. A schematic diagram of the vacuum facility is shown in Fig. 4-2.

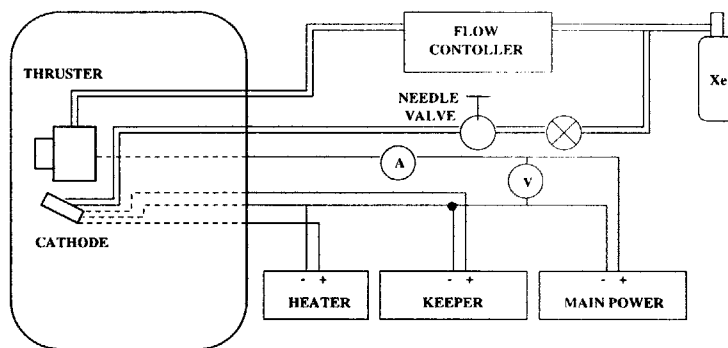


Figure 4-2: Vacuum facility schematic

## 4.2.2 Thrust Balance, Calibration, & Data Acquisition

The micro-balance used in the experiments was a horizontal arm design with the thruster mounted at its tip. The propellant supply line and a flexible power cable were both attached to the two fixed cable clamps, one mounted to the arm and another mounted onto a fixed platform to avoid variations in stiffness and dry friction. To avoid imposing additional stiffness and thus reducing the resolution of the thrust measurements, the cathode, its power cables, and the gas feed lines were mounted to the fixed platform in close proximity to the thruster. As the balance arm failed to provide sufficient heat capacity to accommodate the heat dissipated by the thruster, a cooling jacket was mounted to the thruster walls as shown in Fig. 4-3. Cooling lines were attached to the arm by the cable clamps and diverted to the exterior water supply. An LVDT (Linear Variable Differential Transformer) sensor was used to detect movements of the arm away from its equilibrium position. The signal was fed into a derivative amplifier which in turn activated the damper coil. Two motors were used to control longitudinal and lateral positions of the platform. Prior to the operation of the balance the motors were adjusted so as to bring the arm to its equilibrium position. The LVDT signal was sampled by a digital oscilloscope and stored into a data file for further analysis.

The thrust balance was calibrated in air by determining the effective spring constant of the assembly. This was done by applying a known impulse to the tip of the arm at the point of thrust application and measuring the resultant initial linear

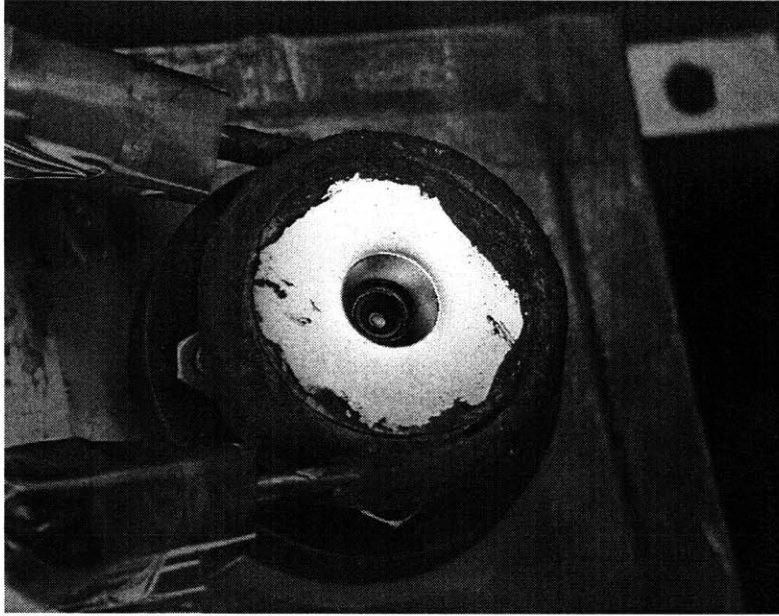


Figure 4-3: Cooling jacket

velocity of the arm at that location. The impulse was determined by integrating the signal from the calibrated force transducer and the effective mass of the arm was computed knowing the impulse and the linear velocity. The effective mass of the arm was estimated to be  $0.001365 \text{ kg} \cdot \text{m}/\text{V}$ . The spring constant was obtained by measuring the undamped natural frequency of the arm undergoing free oscillations which was estimated from the samples of the LVDT traces to be  $1.24 \text{ rad}/\text{sec}$ . The numerical value of the resultant spring constant was  $2.109 \text{ mN}/\text{V}$ .

### 4.2.3 Cathode

A hollow cathode manufactured by Busek Co. was used in the experiments. The cathode was supplied with Xenon at the flow rate of  $1.4 \text{ sccm}$ . Since the cathode was originally designed to operate with larger thrusters in a self-heating mode, the smaller currents drawn by this thruster were not sufficient to maintain stable cathode operation. For this reason, once in a standby mode, the heater current was reduced from the nominal  $6.5 \text{ A}$  to  $3 \text{ A}$  while the keeper current was maintained at  $0.5 \text{ A}$ .

#### 4.2.4 Flow system

Xenon was supplied into the vacuum tank by means of a digital MKS flow controller calibrated for flow rates between 1 and 10 sccm (0.098 to 0.98 mg/s). The upstream pressure in the Xe tank was kept at 50 psi. The flow rate was calibrated before and after the test runs for each of the flow rate settings by passing Xenon bubbles through a beaker immersed upside down into a container with water, thus maintaining nearly atmospheric pressure. The cathode flow was supplied from the same Xenon tank via a needle valve calibrated to deliver 1.4 sccm (see Fig. 4-2).

### 4.3 Test results

A series of vacuum tank tests was performed to assess the overall performance of the micro-Hall thruster. The thrust balance arm was calibrated prior to evacuating the tank while the cooling water was allowed to flow in the lines. Additional calibration was performed at the end of each testing procedure once the tank was vented to the atmosphere. The calibration constant remained unchanged under vacuum as indicated by the arm's natural frequency measured before and after the tank was evacuated. Prior to each test sequence the main flow was turned on and the cathode was set into standby mode until all thermal and mechanical transients in the thrust signal could no longer be observed. Both the anode voltage and the discharge current were monitored at all times, while the thrust signal was visually observed on the oscilloscope screen and logged by the data acquisition system upon completion of each test sequence.

Preliminary test trials have shown a significant thermal drift in the arm's reference position throughout the duration of the firings. After the cooling jacket was mounted to the thruster, however, thermal drifts were almost entirely eliminated. As part of the preliminary validation process for the balance, the arm was allowed to rest at one of its stops while the LVDT signal was monitored with the thruster operating at its nominal conditions. This was done to ensure that the LVDT or any other auxiliary cables which run to the balance and are in close proximity to the plasma do not pick

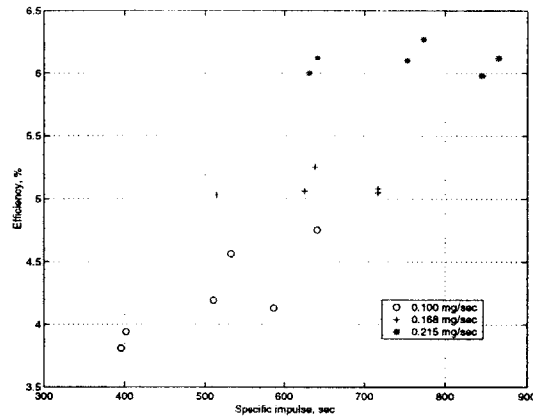


Figure 4-4: 50W Hall thruster performance

up any spurious signals interfering with the thrust measurement. No deviations in the signal were observed.

The test runs were performed at three different voltages: 200, 250, and 300 Volts and three different flow rates: 0.100, 0.168, and 0.215 mg/s. For each test run sufficient time was allotted for the thrust signal and the discharge current to stabilize. Each run lasted approximately 7 to 8 minutes and included one minute before and after each firing to obtain a stable signal reference. The thruster was run twice at each operating condition to ensure that the measurements were repeatable and were not affected by any thermal drifts in the thruster or the balance arm assembly. Thruster efficiencies and specific impulse values were computed from the measured current, voltage, flow rate, and thrust using the following relations:

$$\eta = \frac{T^2}{2IV\dot{m}} \quad (4.1)$$

$$I_{sp} = \frac{T}{\dot{m}g} \quad (4.2)$$

where  $T$  is the thrust,  $\dot{m}$  is the flow rate, and  $g$  is the acceleration due to gravity.

Results of these test runs are conveniently summarized in Fig. 4-4 showing the efficiency as a function of the specific impulse at different flow rates. The measured thrust as a function of the applied voltage is shown in Fig. 4-5. Additional test data can be found in Table 4-6.

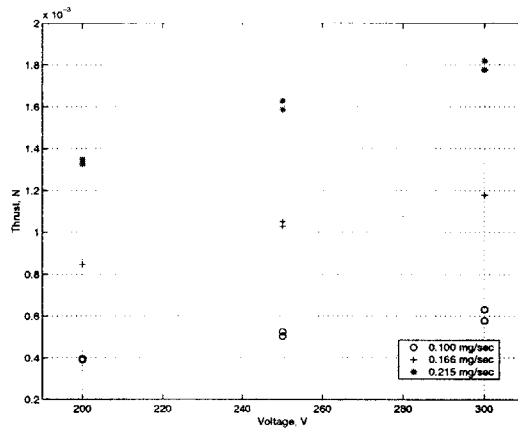


Figure 4-5: 50W Hall thruster performance

## 4.4 Analysis

Analysis of the data shows that, at the near nominal flow rate of 0.215 mg/s, the measured thrust levels were about a factor of two lower than expected, while the discharge current was twice its nominal design value. The resulting efficiencies were, therefore, unexpectedly low at only one eighth of the nominal 50 %. Assuming that most of the voltage drop develops downstream of the ionization zone, the total efficiency can be broken down into the product of the utilization and the acceleration efficiencies:

$$\eta = \eta_u \eta_a \quad (4.3)$$

where  $\eta_u$  is given by:

$$\eta_u = \frac{I_b m_i}{\dot{m} e} = \eta_a \frac{I_a m_i}{\dot{m} e} \quad (4.4)$$

and  $\eta_a = I_b/I_a$ . Since the overall efficiency  $\eta$  can be obtained from the experimentally measured quantities only, both  $\eta_a$  and  $\eta_u$  could be determined from:

$$\eta_a = \sqrt{\eta \frac{\dot{m} e}{I_a m_i}} \quad (4.5)$$

$$\eta_u = \frac{\eta}{\eta_a} \quad (4.6)$$

The resulting utilization efficiencies ranged anywhere between 22 and 40%, values which are unusually low for these types of thrusters. Additionally, measured values of

Flow (kg/s)	Voltage (V)	Current (Amp)	Thrust (N)	Isp (sec)	Efficiency (%)	Ib/Ia (%)	Util. effic (%)
1.005e-07	250	0.120	5.029e-04	510.6	4.19%	16.04%	26.14%
1.005e-07	300	0.134	5.778e-04	586.7	4.13%	15.07%	27.42%
1.005e-07	250	0.120	5.243e-04	532.3	4.56%	16.73%	27.25%
1.005e-07	300	0.139	6.313e-04	641.0	4.75%	15.87%	29.96%
1.005e-07	200	0.099	3.959e-04	402.0	3.94%	17.12%	23.01%
1.005e-07	200	0.099	3.895e-04	395.5	3.81%	16.84%	22.64%
1.676e-07	200	0.212	8.453e-04	514.6	5.03%	17.07%	29.46%
1.676e-07	200	0.212	8.453e-04	514.6	5.03%	17.07%	29.46%
1.676e-07	250	0.250	1.049e-03	638.4	5.25%	16.06%	32.69%
1.676e-07	250	0.249	1.027e-03	625.4	5.06%	15.79%	32.02%
1.676e-07	300	0.273	1.177e-03	716.6	5.05%	15.07%	33.49%
1.676e-07	300	0.271	1.177e-03	716.6	5.08%	15.18%	33.49%
2.146e-07	200	0.346	1.348e-03	641.1	6.12%	16.68%	36.69%
2.146e-07	200	0.342	1.327e-03	630.9	6.00%	16.61%	36.11%
2.146e-07	250	0.393	1.626e-03	773.3	6.27%	15.84%	39.59%
2.146e-07	250	0.383	1.584e-03	753.0	6.10%	15.83%	38.55%
2.146e-07	300	0.420	1.819e-03	864.9	6.12%	15.14%	40.42%
2.146e-07	300	0.410	1.776e-03	844.6	5.98%	15.14%	39.47%

Figure 4-6: Test data

$I_{sp}$ , even at high voltages (300 V), have not exceeded 850 sec. All of these observations point to one likely cause: low degree of ionization in the plasma results in poor utilization of neutrals, hence, low thrust for a given flow rate. Poor ionization can be a result of partial degradation or loss of the magnetic confinement of the electrons. The unusually high values of the ratio of the anode current to the mass flow rate at high voltages, on the order of 2.6-2.7 (as opposed to values  $\sim 1.3$  for larger units), indicate excessive leakage of electrons, and support the above hypothesis. In the search for possible clues, two mechanisms consistent with the observations were identified as most likely to explain the loss of magnetic confinement.

1) Degradation and non-reversible loss of the magnetic field due to the excessive heating and damage to permanent magnets may be a possible cause for electron leakage. Although this mechanism is plausible, thermocouple measurements throughout the tests have indicated that the temperature of the thruster assembly has never exceeded  $42^{\circ}C$ . Since the path between permanent magnets and the thruster mount has relatively low thermal impedance, it is unlikely that the magnets ever reached their maximum allowable temperature of  $275^{\circ}C$ . Subsequent measurements of the magnetic field strength using a miniature Gauss probe indicated that the mean field strength in the vicinity of the pole averaged at about 0.17 Tesla with a maximum of 0.25 Tesla. Since the diameter of the axial probe used in the measurements was com-

parable to that of the central pole piece and since the field strength falls off rapidly away from the pole tip, it is very likely that the measured values of the average field strength over the volume of the probe are a factor of 2 to 3 lower than the expected value within the gap. Since the nominal field strength should be on the order of 0.4-0.5 Tesla, it can be concluded with a certain degree of confidence that the permanent magnets have experienced at worst minimal damage during the course of the experiments.

2) The center pole piece is not properly cooled due to its small cross sectional area and, as a result, may have locally reached temperatures at which magnetic permeability of iron sharply drops to zero. Such a dramatic reduction of permeability would have caused increased fringing of the magnetic field inside the thruster channel, possibly resulting in the loss of the field strength at the channel exit forcing some of the field lines to cross the anode. If that were the case, electrons emitted by the cathode would follow the field lines and easily leak into the anode without fully ionizing the propellant. To validate this hypothesis further, one can estimate the temperature gradient across the magnetic pole subjected to external heating by the plasma and the anode. Although the anode temperatures were never measured directly, prior designs using platinum as the anode material showed slight signs of melting at the tip. Assuming the tip of the anode gets at least as hot as the melting point of platinum ( $\sim 2,000^{\circ}K$ ) and radiates heat from a section at the tip ( $\sim 3$  mm deep), the amount of heat deposited into the iron pole just from the anode is on the order of 6 Watts. Accurately accounting for the additional heat due to the impinging ions and electrons is more difficult. However, it is safe to assume that, including the heat radiated from the anode, a total of 10 Watts are deposited into the iron pole. In steady state, this amounts to a tip temperature differential of  $950^{\circ}K$  with respect to the iron base. Since the Curie temperature for iron is about  $1061^{\circ}K$  and the base temperature is no lower than  $350^{\circ}K$ , it is very likely that the magnetic flux does not penetrate all the way to the tip of the iron pole thus modifying the field profile and reducing its strength within the gap. As a result, magnetic field lines can intersect the anode and enhance collection of electron current without allowing sufficient residence time for

the electrons to fully ionize the gas.

## 4.5 Alternative scaling scenarios

In view of the numerous difficulties associated with the manufacturing and operation of a small-scale device designed to satisfy the strict scaling relations outlined in Chapter 2, alternative scaling models have been considered in the hope of alleviating some of these difficulties while preserving the superior performance characteristics achieved for the larger devices. One such scaling model is based on photographic scaling, i.e. reduction in size of the device while maintaining constant plasma density and the operating voltage. It is easily shown that in this case the quantities of interest scale as follows:

$$P = IV \sim nL^2 \sim L^2 \quad (4.7)$$

$$T \sim nL^2 \sim L^2 \quad (4.8)$$

$$\dot{m} \sim L^2 \quad (4.9)$$

$$I_{sp} \sim 1 \quad (4.10)$$

Maintaining constant plasma density, however, implies that the mean free path becomes proportionately larger in comparison to the scale of the device:

$$\frac{\lambda}{L} \sim \frac{1}{L} \quad (4.11)$$

Therefore, the electrons will not have sufficient residence time to adequately ionize the propellant. Aside from this difficulty, the main advantage of this scaling model is that a given reduction of operating power results in the decrease of size  $L$  in proportion to  $\sqrt{P}$  as opposed to  $L \sim P$  as in the case of strict scaling. Thus, reduction of the operating power from 1.35 kW to 50 W amounts to a decrease in size by only a factor of 5. As a consequence, the strength of the required magnetic field for this configuration will only increase by a factor of 5, possibly within the thermal operational range of standard electric coils. Most importantly, however, this scaling model predicts that

the expected lifetime scales as:

$$t_{life} \sim \frac{L}{n} \sim L \quad (4.12)$$

Therefore, a 50 W Hall thruster would suffer only a five-fold reduction in the operating life in comparison to a device built to satisfy strict scaling, in which case the operating life dropped by almost a factor of 1,000 ! The drawback, however, is that because of the relative increase of the mean free path in comparison to the size of the device, the ionization fraction will be lower causing a reduction in the utilization efficiency. Operation in this regime is equivalent to a reduction of the flow rate for a given geometry. Such operation has been experimentally attempted in the past for a variety of conventional thrusters and, in most cases, has caused significant degradation of the overall thruster efficiency.

It becomes apparent that, depending on which of the two scaling methods are utilized in the design, the resultant device suffers either from a significant loss of the overall efficiency or a loss of the total operating life. One would then expect, that an alternative scaling in which the plasma density is not constant yet does not increase as strongly as  $n \sim 1/L$  with the reduction in size would yield a reasonably efficient thruster with the maximum possible operating life for a given scaling in power and allowable drop in the efficiency.

Consider an arbitrary scaling scenario in which both the power and the length scale reduction are independent. Then, the power and the flow rate both scale in proportion to the product of the plasma density and the characteristic area of the device:

$$P \sim nL^2 \quad (4.13)$$

$$\dot{m} \sim nL^2 \quad (4.14)$$

The ratio of the mean free path to the length scale,  $h = \lambda/L$ , is no longer fixed as an invariant quantity but, instead, is allowed arbitrary variations with the plasma

density and the length scale:

$$h = \left(\frac{v_n}{c_e Q}\right) \frac{1}{nL} \sim \frac{1}{nL} \quad (4.15)$$

Suppose a nominal device with the operating/geometrical characteristics given by  $n_0$ ,  $P_0$ ,  $L_0$ ,  $h_0$ ,  $\dot{m}_0$ , and  $\eta_0$  is to be scaled down in power. Introducing non-dimensional parameters scaled to the nominal:

$$\tilde{n} = \frac{n}{n_0} \quad (4.16)$$

$$\tilde{P} = \frac{P}{P_0} \quad (4.17)$$

$$\tilde{L} = \frac{L}{L_0} \quad (4.18)$$

$$\tilde{h} = \frac{h}{h_0} \quad (4.19)$$

$$\tilde{\dot{m}} = \frac{\dot{m}}{\dot{m}_0} \quad (4.20)$$

$$\tilde{\eta} = \frac{\eta}{\eta_0} \quad (4.21)$$

relations in Eqns. 4.13-4.15 can be written as:

$$\tilde{P} = \tilde{n}\tilde{L}^2 \quad (4.22)$$

$$\tilde{\dot{m}} = \tilde{n}\tilde{L}^2 \quad (4.23)$$

$$\tilde{h} = \frac{1}{\tilde{n}\tilde{L}} \quad (4.24)$$

Substituting Eqn. 4.24 into Eqn. 4.23 yields an expression for the power scaling as a function of the characteristic parameter  $\tilde{h}$ :

$$\tilde{P} = \frac{\tilde{L}}{\tilde{h}} \quad (4.25)$$

The disproportional increase of the mean free path in comparison to the size of the device is what is thought to produce the drop in the utilization efficiency. Therefore,

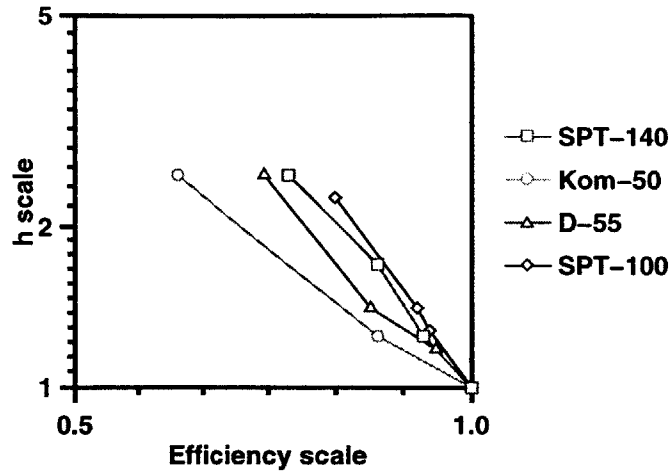


Figure 4-7: Dependence of the efficiency on the mean free path parameter  $\tilde{h}$

obtaining a relationship between  $\tilde{h}$  and  $\tilde{\eta}$  would allow one to predict the degradation in performance under arbitrary scaling conditions.

It was already noted that an increase in the quantity  $h$  can be due to either a disproportionately small reduction in size for a given decrease in the flow rate or, alternatively, to a corresponding decrease in the flow rate for a device with a fixed geometry. Several existing thruster models for which the efficiency data are readily available have been operated at off-design conditions, specifically at reduced flow rates. The empirical dependence of  $\tilde{\eta}$  versus  $\tilde{h}$  for several commercial thrusters in the SPT series: SPT-100 [20], SPT-140 [21], a TAL model D-55 [22], and a 50 mm laboratory version by Komurasaki [23] was extracted from the data and is graphically summarized in Fig. 4-7. The experimental quantities plotted in Fig. 4-7 were scaled to the operating conditions corresponding to the maximum obtained efficiency for a given thruster. Fig. 4-7 clearly indicates a drop in the overall efficiency as the mean free path becomes disproportionately larger in comparison to the size of the device. Moreover, as the data suggest, the dependence of  $\tilde{h}$  on  $\tilde{\eta}$  can be simply modeled as an inverse power law which, surprisingly, is very weakly dependent on the dimension of the device and can be extrapolated to predict the efficiency of smaller thrusters with an equivalent deviation in  $\tilde{h}$ . Extracting the empirical dependence of  $\tilde{h}$  on  $\tilde{\eta}$  for the SPT series as approximately given by:

$$\tilde{h} \approx \frac{1}{\tilde{\eta}^3} \quad (4.26)$$

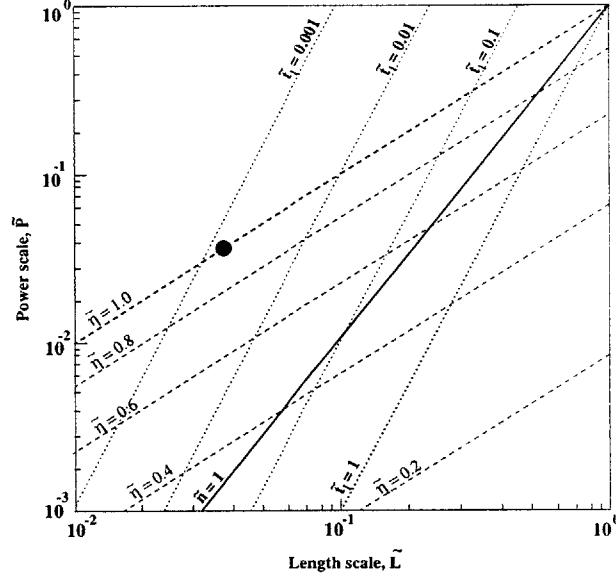


Figure 4-8: General scaling strategies

the contours of constant efficiency can be determined by substituting Eqn. 4.26 into Eqn. 4.25:

$$\tilde{\eta}^3 = \frac{\tilde{P}}{\tilde{L}} \quad (4.27)$$

The contours of constant efficiency are plotted as dashed lines in the  $\tilde{P}$ - $\tilde{L}$  scale space as shown in the accompanying Fig. 4-8. Note that the strict scaling for which the efficiency remains constant and for which  $P \sim L$  is easily recovered as the curve  $\tilde{\eta} = 1$ . The lines of constant operating life referenced to the nominal can be determined as the ratio of the length scale to the plasma density:

$$\tilde{t}_l = \frac{\tilde{L}}{\tilde{n}} = \frac{\tilde{L}^3}{\tilde{P}} \quad (4.28)$$

These lines can be overlaid on top and are shown as dotted lines in Fig. 4-8. Photographic scaling can also be shown as the line of constant plasma density (solid line):

$$\tilde{n} = \frac{\tilde{P}}{\tilde{L}^2} \quad (4.29)$$

The scaling alternatives conveniently summarized in Fig. 4-8 can be easily interpreted. Following strict scaling (solid line  $\tilde{\eta} = 1$ ) from the upper right corner, the

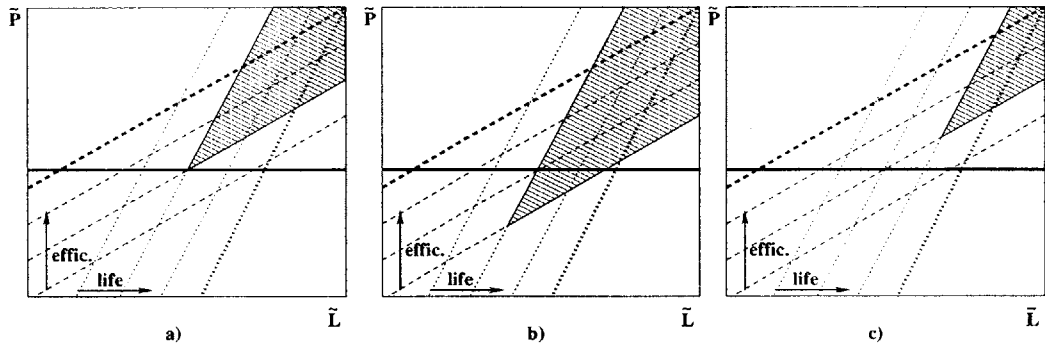


Figure 4-9: Scaling scenarios

reduction of power from 1,350 W to the desired 50 W level ( $\tilde{P} = 0.037$ ) corresponds to a reduction in size by a factor of 27 or  $\tilde{L} = 0.037$ . The location of this operating point is marked on the diagram. Although the efficiency has remained constant, the lifetime is reduced by almost a factor of 700 from the nominal. Alternatively, following the photographic scaling strategy (solid line) to the power level corresponding to  $\tilde{P} = 0.037$ , the reduction in size corresponds to only  $\tilde{L} = 0.2$ . At that location, the lifetime is reduced by only a factor of 5, however, the efficiency is down by a factor of 0.6 from the nominal. The plot also indicates that the two scaling strategies presented earlier are not special and are just examples of limiting behavior ( $\tilde{\eta} = 1$  or  $\tilde{n} = 1$ ), so that for a given reduction in power (line  $\tilde{P} = 0.037$ ) there is an unlimited number of scaling alternatives for which the drop in efficiency can be traded with the loss in operating life. For a specified minimum operating life and a minimum tolerable efficiency, there is a maximum reduction of power for which these specifications can be met with a single scaling strategy (Fig. 4-9a). If the desired power level reduction is less than the maximum, there exists an unlimited number of alternatives (Fig. 4-9b). However, if the reduction of power exceeds the maximum allowable, no scaling solutions are available to meet the specifications (Fig. 4-9c). The use of alternative scaling strategies presents a viable solution for overcoming or offsetting the intrinsic lifetime limitations that most plasma devices experience at small scale by partially sacrificing their operating efficiencies. Studies of the applicability of these devices to missions of future interest, comparison to other competing technologies, and possible implementation of these alternative scaling strategies are important avenues for further exploration.

## 4.6 Conclusions and recommendations

Despite the disappointingly low performance, the effort to miniaturize a Hall thruster has provided a number of useful insights for any such attempts in the future. Most importantly, this work has highlighted the generic difficulty, common to all plasma thrusters, associated with the increase of the plasma density as the scale of the device is reduced. The consequences of such scaling, most notably the higher particle fluxes which cause an increase in the erosion rates and significant loss of operating life at small scale, create a strong incentive to search for propulsion schemes which avoid ionization by electron bombardment.

Another important aspect of the higher plasma density is the increased heat flux into the wall. It was found that, with an appropriate choice of materials and component configurations, the intrinsically stronger thermal gradients could be exploited to shunt heat to non-critical areas for radiation. The final dimensions of the iron center pole, however, were such that sufficient heat conduction was not achieved. This resulted in the partial loss of magnetic permeability near the tip and a decrease of the magnetic field strength within the gap. In retrospect, the situation could have been improved if the center pole had been designed to be somewhat thicker with a conical taper and a thicker base. Even if attempted, however, tight tolerances as well as the alignment and geometrical constraints dictated by scaling, make these alterations extremely difficult, if not impossible.

Another lesson learned was the need to use permanent magnets in order to achieve the higher magnetic fields dictated by scaling. Although the use of permanent magnets had extended the available scaling range to power levels beyond what is normally possible with electric coils, intrinsic limitations of the existing magnetic alloys do not permit scaling below power levels of about 40-45 Watts. In addition, the sensitivity of these magnets to temperature makes thermal design of these and other components especially important. The current design appears to be satisfactory in this respect, except that, because of the unexpectedly low efficiency and, hence, additional unforeseen heat dissipation, it is possible that some reversible field weakening

may have occurred during operation. As suggested by the subsequent measurements of the magnetic field strength, it is unlikely that excessive heating had caused any permanent damage to the magnets.

The very small physical dimensions of the 50 Watt Hall thruster have posed a number of practical difficulties. Some of the more significant and severe ones are outlined below:

a) Measuring and mapping the profile of the magnetic field strength within the narrow 1.6 mm gap to even moderate accuracy requires the use of magnetic field sensors which are less than 50-100  $\mu m$  in size. The lack of adequate instrumentation has precluded any detailed measurements from being made to validate the nominal field strength against the results of a numerical simulation, or to examine the changes, if any, in the field strength that may have occurs over the course of the experiments. A large 1.5 mm Gauss probe was used instead to provide a rough indication of the mean magnetic field strength in the vicinity of the central pole piece.

b) Following the configurations of the typical TAL designs, the anode of the miniature thruster was extended towards the exit of the channel where the field profile is tailored so as to be tangent to the frontal face of the anode. Hence, even minimal misalignment of the anode with respect to the thruster center line may force the field lines to intersect the anode and cause excessive electron leakage. Attaining relative tolerances on centering and alignment comparable to those in larger devices is generally more difficult with miniature components.

c) Rough measurements of the magnetic field strength using a 1.5 mm Gauss probe have also indicated a non-uniformity of the field strength in the azimuthal direction. Significant variations of the field strength along the circumference of the channel, at certain locations by as much as a factor of two, can be attributed to the variability in the shapes of the segmented magnets. Crumbling and the lack of axial symmetry due to the manufacturing and assembly imperfections may have contributed to the

field variations as well. Such strong azimuthal gradients suggest that, even prior to thruster operation, the nominal field profile may not have been properly shaped to prevent intersections of the field lines with the anode.

d) Reduction in component dimensions made the manufacturing of the critical parts, such as the anode and the magnetic circuit assembly, more difficult. The choice of a TAL configuration with an extended anode was primarily dictated by the desire to avoid the use of a thin and fragile ceramic insulator but, in turn, it introduced an unwanted sensitivity to alignment.

e) Small magnetic particles had a tendency to lodge in the narrow (0.3 mm) gap between the anode and the main magnet creating occasional shorting. Although some of these particles were metallic dust collected during handling and installation, the majority of them were debris from the SmCo magnet. The magnets were ultimately encapsulated in nickel to reduce crumbling.

f) Removal of the trapped magnetic particles from the gap between the anode and the magnetic assembly prior to thruster installation required the ability to access the interior of the channel. Because of the need to provide for assembly and disassembly of the anode supported by its metallic feed tubes, press fits were used at one of their ends. The problem of ensuring gas tightness at that location was not fully resolved and gas leaks could not be completely ruled out. Improvements are needed in this regard.

g) The most severe limitation, however, is the loss of operating life due to the increased particle fluxes and erosion rates at small scale. It was shown in the earlier sections that the expected lifetime of the micro-Hall thruster is reduced by almost a factor of a thousand from the nominal life of 7,000 hrs experimentally obtained for a larger 1.35 kW thruster (SPT-100). Although no specific erosion rate measurements were performed, the signs of accelerated erosion can be clearly seen with a naked

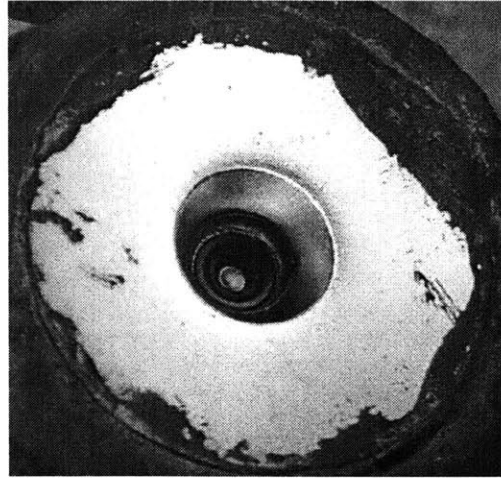


Figure 4-10: Erosion pattern at the center pole piece

eye after about 8-10 hours of accumulated operational time. Fig. 4-10 clearly shows a deep cavity which was developed on the frontal face of the center pole piece due to the impinging ions. A slight tapering of the sharp cylindrical edge of the anode tip towards the axis can also be observed. Visible deposition of sputtered metallic material onto the slanted walls of the stainless cover provides yet another indicator of the encroaching problem. To the best of our understanding, poor performance was not an intrinsic feature of the reduced scale, but rather the indirect consequence of the imperfections due to the operational, assembly, and manufacturing difficulties listed above. As noted in the earlier sections, distortion of the magnetic field due to the overheating of the center pole piece is the most likely explanation. Unfortunately, iteration and improvement would require both diagnostics, which are not available at this scale, and a stronger motivation which can not be justified in view of the intrinsic lifetime limitations of this micro-plasma device.

# Chapter 5

## Physics of Colloidal Thrusters

### 5.1 Literature Review

#### 5.1.1 Scientific work in the area of electro-spray physics

The early work in the area of electro-spray science dates back to the 1900's when experimental investigations by Zeleny [24], [25] first demonstrated the existence of a stable conical meniscus when a fluid surface was subjected to an applied electrostatic stress. Numerous qualitative observations revealed that for a range of operating voltages and flow rates the shape of the meniscus was that of a nearly perfect cone with a semi-cone angle of approximately 49 degrees. The first theoretical work that explained the observed behavior was that of G.I. Taylor [26], who showed that the simplest equipotential surface for which surface tension can balance electrostatic traction is that of a cone with a semi-cone angle of nearly 49.3 degrees. In light of this important discovery, conical equipotential surfaces for which such balance is satisfied are now referred to as Taylor cones. Shortly thereafter, Hendricks and Pfeifer [9] developed a linearized model analyzing the stability of surface perturbations under the action of a normal electric field. In their estimates of the charge to mass ratio they utilized the fact that the amount of charge accumulated on each of the ejected droplets could not exceed that for which the surface tension exactly balanced electrostatic repulsion. The breakup process of charged droplets was studied in detail by

Lord Rayleigh in 1882 and the stress criterion which yields the maximum charge to mass ratio is nowadays referred to as the Rayleigh limit.

Although Taylor's hypothesis did shed some light on the most likely mechanism responsible for the prevailing geometry of the observed fluid shapes, his simple model was inadequate to explain the formation of a thin jet issuing at the tip of the cone. In addition, it failed to explain the noticeable deviations of the fluid menisci from a 49.3-degree cone under certain operating conditions. For an electro-spray in air, where droplets are mobility limited, such deviations were explained by F. de la Mora [16] as the effects of space charge due to the droplets present in a conical jet modifying the electrostatic field at the cone surface. The work by Mestel [27] contains one of the first attempts to model the mechanisms responsible for the formation of a charged jet for flows at high Reynolds numbers showing reasonable agreement with the data. A more fundamental mechanism, however, was suggested by F. de la Mora [15] showing that the cone was unable to maintain constant potential near the tip due to the increasing rate of charge convection. As a result, the equipotential conical solution could no longer apply and a different geometry must set in. With the help of a simple semi-empirical model, F. de la Mora was able to determine the characteristic size of the jet and to obtain a scaling relation between the current and the flow rate, both found to be in good agreement with the experimental data. Another work by Chen et al [8] details an experiment further confirming the dependence of the current on the flow rate and which also analyzes the droplet size distribution as a function of the flow rate and the electrical conductivity of the solution. de Juan and F. de la Mora [28] in their joint experimental work used a differential mobility analyzer and a size spectrometer to determine the distribution of charge, droplet size, and the charge to mass ratio. Their results indicated that although the charge and the mass of the droplets were each broadly distributed, the ratio of charge to mass was contained within a narrow band, suggesting that at the time of breakup, most of the charge was frozen to the fluid. Another work was performed by Rossell-Llompart and F. de la Mora [14] to measure the droplet size distribution as a function of the flow rate, viscosity, and the electrical conductivity. The results of this study indicated that

although the jet diameter was mainly controlled by the flow rate and the electrical conductivity of the solution, and was generally unaffected by moderate changes in viscosity, the process of jet breakup and the resulting droplet size distribution did show some dependence.

A number of early studies involving glycerol solutions and more recent work with a number of high-conductivity electrolytes suggest that under certain conditions, as the jet diameter decreases in size, the electric field at the tip increases to the point when not only droplets, but also pure ions can be directly extracted from the surface. Since the charge to mass ratio of pure ions can be orders of magnitude larger than that of droplets, mixed-regime operation involving both ions and droplets is important from the standpoint of propulsion applications. The process of ion emission from the tip of a cone-jet has been studied in detail by Loscertales and F. de la Mora [29]. The experiments have shown that the strength of the electric field required for ion evaporation was on the order 1 V/nm. In a more recent study by Gamero-Castano [17], accurate measurements were performed using a stopping potential with a differential mobility analyzer to determine the constituents of the jet by their charge and mass. It was concluded that for sufficiently low flow rates ions could be extracted directly from the neck of the jet, producing significantly more current for a given flow rate than predicted for pure droplets.

### **5.1.2 Developments in the field of colloidal propulsion**

The earlier scientific work in area of electro-spray physics was mainly motivated by meteorological studies of charged rain droplets, industrial applications to spray-painting, or chemical diagnostics using mass-spectroscopy. In the 1960's, however, because of the scientific advances and progress in the understanding of electro-spray physics, strides were made to develop the first prototypes of colloidal thrusters. The specific needs of this application demanded that highly charged particles be accelerated to high speeds, yet at the same time operating at sufficiently low voltages to be acceptable in the spacecraft environment. These conflicting requirements have shifted the emphasis of the research efforts in this area from component level design

towards more detailed studies of thruster physics in an attempt to achieve emission of droplets with larger charge to mass ratios.

The first attempts to develop operational models of colloidal thrusters date back to the 1960s. Cohen et al. of TRW [30] used glycerol solutions with sulfuric acid (conductivity on the order of 0.02 Si/m) in a multi-needle arrangement to extract and accelerate droplets across a 100 kV potential difference. Such high voltages were necessary because of the relatively low charge to mass ratio obtained for the fluids used in the experiments, ranging anywhere from 100 to 400 C/kg in most cases. Krohn [31] of Space Technology Labs in his experimental work used a time-of-flight analyzer to measure the charge to mass ratio of droplets produced from the glycerol solution with antimony trichloride. A narrow distribution of charge to mass ratio was reported with the mean centering at about 470 C/kg. The author admits that an  $I_{sp}$  of 2,000 sec could be achieved only if these droplets were accelerated through a mind-boggling 430,000 Volts of potential difference. A research study by Perel and Mahoney [11] contains data for solutions of sulfuric acid in glycerol for various electrical conductivities. Surprisingly, even at sufficiently low conductivities, the reported mean charge to mass ratio was on the order of  $4 \times 10^4$  C/kg. Such large values of charge to mass ratio could be explained only by a hypothesis that a significant portion of the emitted particles were, in fact, ions which were directly extracted from the tip of the meniscus. As such, the behavior of glycerol did not conform to the existing models which predict that low conductivity solutions are unable to produce a thin enough jet for the normal field to reach sufficient strength for ion emission. This anomaly has been recently resolved and is analyzed in detail in the current Chapter. The same work by Perel also suggests a possible bipolar thruster configuration in which droplets carrying both positive and negative charge could be extracted simultaneously by applying opposite polarity potentials to a number of adjacent electrodes. Such a configuration would eliminate the need for a separate cathode and would prevent spacecraft charging during operation. A successful 1,000-hour duration test was later performed by the same group on an annular colloidal thruster operating on a solution of lithium iodide in glycerol at 15 kV with an  $I_{sp}$  of

1,160 sec [12]. Additional modifications to the design including annular configurations and the use of a different solute as a working fluid were exploited in the follow-up experiments [13],[32] reporting efficiencies as high as 73%. At about the same time a group at TRW [10] performed a 4,300-hour lifetime test on a multi-needle thruster module utilizing sodium iodide dissolved in glycerol and operating at 12.3 kV. The thruster operated at an average  $I_{sp}$  of 1,300 sec and delivered thrust on the order of 75  $\mu lb$ . Limited signs of erosion were reported, however, with little or no consequence to the overall performance of the device. One of the last reported research activities in the area of colloidal propulsion was the experimental work by Huberman and Rosen [33]. They utilized an annular geometry with three segmented electrodes to allow for limited thrust vectoring, and produced 547  $\mu N$  of thrust at an  $I_{sp}$  of 1,325 sec: performance results very similar to those obtained in [32], [10].

No relevant literature was found during the time period after 1974 up until more recently in 1995. A brief article by Shtyrlin [34] summarizes the work performed at MAI (Russia) for the past decade reporting the development efforts of a thruster array operating at 15 kV and emitting particles with charge to mass ratios of nearly 3,300 C/kg. It appears that the interest in colloidal thrusters had suddenly disappeared after a number of successful attempts to develop and test high-efficiency prototypes. It is possible that the need for high voltages, in most cases exceeding 10 kV, drew the attention of propulsion engineers away from colloidal thrusters towards alternative technologies (such as ion engines or Hall thrusters) operating at significantly lower voltages, yet demonstrating efficiencies comparable to those of colloidal thruster. Potential complications associated with the manufacturing of multi-needle arrays to produce sufficient thrust levels required for most military and commercial spacecraft may also have contributed to the overall halt in their development.

## 5.2 Weaknesses of current models

In spite of the extensive research efforts put into the development and understanding of colloidal thruster physics, there currently exists no single theory which encompasses

all of the mechanisms to satisfactorily explain the phenomena observed in the experiments. Understanding of a number of unresolved issues and experimental anomalies still remains a challenge to this day. Some of these pending problems require further investigation and are briefly summarized below.

a) It was alluded to in a number of recent models [35], [15] that the fluid's viscosity has little effect on the performance of a cone-jet emitter. This was mainly motivated by the fact that the sink flow dominates over the recirculating shear flow near the tip, so that viscosity never shows up in determining the flow pattern in the vicinity of the jet and, hence, does not affect the resulting charge to mass ratio of the droplets. Although the majority of the fluid combinations (both solvents and solutes) utilized in the experiments have, indeed, demonstrated the alleged lack of dependence on viscosity, viscous glycerol solutions in the work by Perel et al [11], [12] have yielded currents orders of magnitude larger than those predicted by the model. Such excessive currents can be attributed to either ions directly extracted from the fluid surface in the vicinity of the tip or to the development of multiple cones each of which carries much smaller currents (see below). It was believed, up until recently, that under nominal operating conditions the characteristic jet size scales with the cube root of the flow rate and inversely with the cube root of the electrical conductivity, so that low-conductivity solutions can only produce jets with larger dimensions and correspondingly lower values of the normal electric field at the surface. It was, therefore, believed that such low-conductivity solutions as those with glycerol used by Perel et al were unlikely to reach sufficient normal fields to initiate ion emission. Recent work by M. Martinez-Sanchez (MIT) has shown that the anomalous behavior of glycerol can be attributed to the dependence of ion mobility on fluid viscosity (see Sec. 5.4 for details).

b) It has been observed in a number of experiments, especially those involving glycerol, that at sufficiently high voltages multiple cones form at each of the emitter tips. Although crude explanations as to the possible nature of this so-called highly stressed regime do exist [36], no solid theory is available to adequately predict the circumstances under which such multiple tips develop.

c) In high-conductivity solutions operated at sufficiently low flow rates, in addition

to pure droplets, ions were emitted directly from the tip of the meniscus. Because of their large charge to mass ratio, even a small fraction of ions by mass contributes significantly to the overall current. Hence, the trend of current versus flow rate, which is generally well correlated with the data in the absence of ions, is no longer valid. It is, therefore, plausible that such strong ion current may have an impact on the production of droplets and the resulting charge to mass ratio. As none of the current models consider the impact of ion emission on the processes responsible for the formation of the jet and its breakup, further analysis is needed to assess these effects for the case of mixed-mode operation.

d) Currently existing electrohydrodynamic models of cone-jet emitters almost invariably assume that an unlimited supply of charge is available in the fluid core to be driven to the surface and convected towards the tip. Although this may be the case within the cone where the fluid velocity and the convective currents are still small, the number of dissociated ions in the core may be depleting in the vicinity of the tip, resulting in an effective decrease of the electrical conductivity. This effect may have been observed in the work by F. de la Mora [15] in the analysis of the so-called minimum flow rate. As suggested by the experiments, for each fluid combination there exists a minimum value of the flow rate for which only positive ions but not the negative ones are extracted together with the droplets, emitting the maximum possible current for a given flow rate. Such complete charge separation indicates that all of the available positive ions have been driven to the surface and additional ion conduction to the surface is no longer possible. Understanding the mechanisms of ion depletion and the resulting decrease in the electrical conductivity are of significance for the desired mixed-mode operation since ion emission usually occurs near the minimum flow rate.

e) Colloidal emitters based on bipolar operation are able to remove both the positive and the negative ions away from the fluid core. Conventional emitters, however, extract ions of a single polarity only, hence, the by-products of the neutralization of ions with the opposite polarity accumulate within the fluid core and can potentially affect the operation. Experimental observations [15] indicate that some of the nega-

tive ions, especially those with iodine and bromine, which are retained in the solution, combine pairwise to form a gaseous residue. Gas molecules then either dissolve in the solution or form bubbles which periodically emanate from the fluid. Aside from the limited qualitative observations, the effects of this process on the performance of cone-jet emitters are not well understood and require further studies.

## 5.3 Scaling and performance of colloidal thrusters

Complete and up-to-date descriptions of the known physics and the scaling laws governing the operation of colloidal thrusters have not yet been published in the literature. Specifically, the analysis of the mixed-regime physics, the resulting advantages of low-voltage operation, and the explanation of the minimum flow rate are discussed here in some detail. An attempt was made to provide a complete account of the relevant mechanisms responsible for the cone-jet electrostatics, charge transport, and the formation of charged droplets justifying, at least conceptually, the multitude of the experimentally observed phenomena. A more detailed numerical analysis incorporating these effects at once can be found in Chapter 7.

### 5.3.1 Electrostatics of cone-jet emitters

The free surface of a conducting fluid subject to a normal electrostatic stress can become unstable and form into a quasi-stable protrusion along which electrostatic stress balances the surface tension. Several analyses have been published in the literature [15],[27],[37],[9],[36] containing alternative derivations or statements of a criterion for the minimum electric field required to induce a surface instability. All of these derivations ignore the contribution to the overall stress due to the internal pressure in comparison to the electrostatic stress and surface tension. It is qualitatively true that the pressure alone can not induce an instability since, unlike other stress components, it does not intensify with decreasing radius of curvature. Hence, for the purposes of this analysis, once electrostatic traction dominates, the effects of internal pressure can be ignored. The simplest approach to obtain a stability criterion [15] is

to assume that a spherical meniscus is formed at the tip of a thin capillary of radius  $R_0$  such that most of the voltage drop develops near the tip and that the electric field is independent of the external electrode geometry and can be locally approximated as:

$$E_s = \frac{V}{R_0} \quad (5.1)$$

where  $V$  is the applied voltage. Surface instability occurs when electrostatic stress exceeds that due to surface tension:

$$\frac{1}{2}\epsilon_0 E_s^2 > \frac{2\gamma}{R_0} \quad (5.2)$$

or, solving for the minimum required voltage:

$$V_{min} > \sqrt{\frac{4\gamma R_0}{\epsilon_0}} \quad (5.3)$$

A more detailed analysis by Martinez-Sanchez [36] assumes that the capillary with the fluid meniscus has a shape of a prolate spheroid with radius of curvature  $R_0$  at the tip and an extractor electrode as a flat plate located a distance  $L$  away from the focus of the spheroid. This electrode geometry more closely resembles that of a typical electro-spray emitter and, in addition, has a known electrostatic solution in prolate spheroidal coordinates producing an expression similar to that in Eqn. 5.3 for the minimum required voltage,

$$V_{min} > \sqrt{\frac{\gamma R_0}{\epsilon_0}} \ln\left(\frac{4L}{R_0}\right) \quad (5.4)$$

Note that this expression now includes a logarithmic correction factor accounting for the effect of a nearby electrode.

Although quantitatively less precise, a fundamentally more appealing approach is presented in Ref. [9] where a linearized analysis of a periodically varying surface perturbation is performed to determine the criterion for which small amplitude surface waves become unstable when subjected to an applied electric field. Suppose the

surface of the fluid lies in the  $xz$ -plane with a zeroth-order uniform electric field at the surface pointing in the  $y$ -direction. Assuming the total electric potential to be a superposition of the nominal component which is linear in  $y$  with a harmonically varying perturbation of the form:

$$\phi = -E_0 y + \delta\phi e^{-ay} \cos kx \quad (5.5)$$

the equipotential surface for which  $\phi = 0$  in the limit  $ay \rightarrow 0$  can be expressed as:

$$0 \approx -E_0 y + \delta\phi \cos kx \quad (5.6)$$

or

$$y \approx \frac{\delta\phi}{E_0} \cos kx \quad (5.7)$$

The constant  $k$  in Eqns. 5.5-5.7 is the wave number given by  $k = 2\pi/\lambda$  where  $\lambda$  is the wavelength of a periodic disturbance. The maximum curvature can be determined by taking the second derivative of  $y$  and evaluating it at the crests for which  $kx = 2n\pi$ :

$$\frac{1}{R_c} = \frac{\delta\phi k^2}{E_0} \quad (5.8)$$

The instability at the surface will occur when a perturbation in the electrostatic stress exceeds the restoring stress due to surface tension:

$$\delta \left( \frac{1}{2} \epsilon_0 E^2 \right) = \epsilon_0 E_0 \delta E > \frac{2\gamma}{R_c} \quad (5.9)$$

Evaluating the total electric field at the crests:

$$E = -\frac{\partial\phi}{\partial y} = E_0 + \delta\phi k \quad (5.10)$$

and substituting the nominal and the first-order corrections into Eqn. 5.9 results in the following expression for  $E_0$ :

$$E_0 > \sqrt{\frac{\gamma k}{\epsilon_0}} \quad (5.11)$$

Since the onset of instability afflicts waves with the smallest value of  $k$  (or largest wavelength) first, taking  $\lambda/2$  to be the diameter of the capillary  $\lambda/2 = 2R_0$  and using  $V_{min} \approx E_0 R_0$  gives the following expression for the minimum required voltage:

$$V_{min} > \sqrt{\frac{\pi\gamma R_0}{2\epsilon_0}} \quad (5.12)$$

This expression is in good qualitative agreement with the alternative versions of the estimate for the minimum required voltage given in Eqns. 5.3 and 5.4.

It has been observed in numerous experimental studies by Zeleny [24],[25], Taylor [26], de la Mora [15], [16] and many others, that once the threshold voltage has been exceeded, the fluid surface deforms into a conical protrusion which remains statically in stable equilibrium. It was also observed that the resulting semi-cone angle was almost universally in the vicinity of  $49^\circ$ . The first explanation for the existence of such cones was provided by G.I. Taylor [26].

Consider a cone to be an equipotential surface with a semi-cone angle  $\alpha$  as shown in Fig. 5-1. Ignoring the contribution of the internal pressure to the overall stress balance, the normal electric field must be such that the electrostatic traction balances the surface tension at all points along the meniscus. It should be noted, however, that such a solution would apply only when the internal pressure is very small or sufficiently close to the tip. It will be shown shortly, that both the surface tension and the electrostatic traction scale inversely with the polar radius  $r$  and will both dominate over the internal pressure near the tip ( $r \rightarrow 0$ ). Thus, as long as the supplied upstream pressure is sufficiently low, Taylor's solution is likely to apply in the vicinity of the tip. Hence:

$$\frac{1}{2}\epsilon_0 E_n^2 = \frac{\gamma}{R_c} \quad (5.13)$$

where  $R_c$  is the effective radius of curvature. An expression for the curvature can be obtained from the divergence of the unit normal vector. In polar coordinates the curvature for a cylindrically symmetric surface specified by a generator  $z(R)$  can be written as:

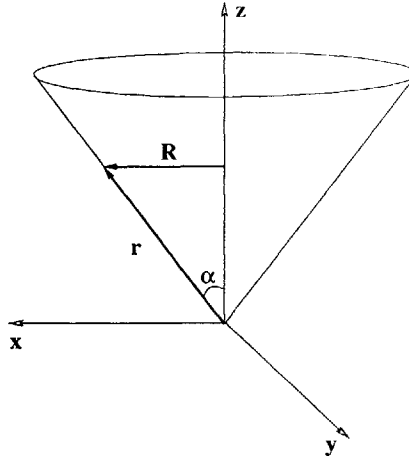


Figure 5-1: Conical geometry

$$\kappa = \frac{\ddot{z} + \dot{z}/R + \dot{z}^3/R}{(1 + \dot{z}^2)^{3/2}} \quad (5.14)$$

For a conical surface  $\ddot{z} = 0$  and  $\dot{z} = \cot \alpha$ . Rewriting Eqn. 5.14 in terms of the polar radius  $r = R/\sin \alpha$  produces the following expression for the curvature:

$$\kappa = \frac{\cot \alpha}{r} \quad (5.15)$$

Imposing the stress balance in Eqn. 5.13 and solving for the normal electric field gives:

$$E_n^o = \sqrt{\frac{2\gamma \cot \alpha}{\epsilon_0 r}} \quad (5.16)$$

It is now necessary to determine a suitable scalar potential which satisfies Laplace's equation outside the cone and which produces an electric field which varies inversely with polar radius  $r$ . The general solution of Laplace's equation in spherical coordinates can be written as:

$$\phi = Ar^\nu P_\nu(\cos \theta) + Br^\nu Q_\nu(\cos \theta) \quad (5.17)$$

where  $P_\nu$  and  $Q_\nu$  are Legendre functions of order  $\nu$ . For the electric field to have proper dependence on  $r$  (see Eqn. 5.16),  $\nu$  has to be equal to  $1/2$ . Of the two independent solutions,  $Q_{1/2}$  has a singularity inside the cone along its axis ( $\theta = 0$ ), while  $P_{1/2}$  is singular outside the cone for  $\theta = \pi$ . Since the intention is to obtain an

external solution, the coefficient multiplying  $P_\nu$  can be taken to be zero. Hence:

$$\phi = Br^{1/2}Q_{1/2}(\cos \theta) \quad (5.18)$$

For the surface to be equipotential,  $\phi$  must be constant and independent of  $r$ . Since  $B$  can not be equal to zero, the only possible solution is the one for which  $Q_{1/2}(\cos \theta) = 0$  and  $\phi = 0$ . The function  $Q_{1/2}$  has a single zero corresponding to  $\theta = 49.29^\circ$ . The latter is an equation of a cone in spherical coordinates for which the semi-cone angle is equal to  $49.29^\circ$ . It should be noted that this result is independent of the applied voltage, electrode geometry, or fluid properties.

Although this simplified analysis due to Taylor does provide a plausible explanation for the prevailing shapes numerous reported in the experiments, it fails to address a number of important issues. It is clear from Eqn. 5.16 that the electric field diverges near the tip when  $r \rightarrow 0$ . Since it is physically impossible to attain infinite fields, Taylor's solution must eventually break down in the vicinity of the singularity. Taylor's solution also implies that the conical meniscus shape is universal and is independent of the electrode geometry. This could be the case only if the local stress balance near the surface dominates the electrostatics and the transition to an arbitrary external geometry takes place far enough away to have minimal impact. In addition, an ideal conical surface considered in the analysis, the one for which  $\ddot{z} = 0$ , although the simplest, is only valid in the absence of the internal pressure, for a particular electrode geometry, and a specific value of the applied voltage. Other more complicated shapes with non-zero generator curvatures will be produced for any other geometries and operating conditions. In those cases the potential can be expressed as a superposition of Legendre polynomials with coefficients chosen to satisfy the stress balance and the equipotentiality condition. Taylor's solution, however, is still expected to be valid in the region sufficiently close to the tip (but far away from the jet), where the internal pressure is small in comparison to the other stress components and for radial distances much smaller than the typical electrode dimensions. Finally, Taylor's assumption that the cone surface is equipotential is questionable.

Experimental evidence [15] suggests that due to the finite conductivity of the fluid, voltage drop develops along the surface of the meniscus intensifying towards the tip. The same data also indicate that it is the inability to maintain constant potential near the tip that produces the tangential field, accelerates the fluid, and ultimately determines the location and the size of the jet.

### 5.3.2 Formation of the jet

As mentioned in the previous section, Taylor's conical solution fails sufficiently close the apex of the cone since the predicted expression for the electric field diverges as  $r \rightarrow 0$ . It is expected then, that an alternative electrostatic and surface profile solutions would set in to avoid the singularity. Experimentally, a thin jet is observed to emerge at the apex of the cone.

The majority of fluids utilized for the purposes of electro-spraying are generally organic solvents with dissolved electrolytes to achieve desirable levels of ionic conductivity. Under the influence of the normal electric field, charges of a single polarity are continuously drawn from the fluid core to the surface maintaining a nearly constant surface potential. Since the cone surface is highly charged, the jet which forms near the tip carries away an excess of charge and gives rise to an electrical current. Near the base of the cone, where fluid velocity is still low, the convective current is negligible, and most of the charge is transported by conduction within the fluid core. Closer to the apex, however, as the fluid velocity increases and the area available for conduction decreases, more and more charge is drawn to the surface and convected by the moving fluid. Sufficiently close to the tip, the rate of convective charge transport becomes greater than the rate at which the charge can be supplied to the surface and the surface potential begins to drop. From that point onwards the conical equipotential solution is no longer valid, and a charged jet emerges.

A scaling relation for the jet radius was first obtained and experimentally verified by F. de la Mora [15] for a variety of fluid solutions with different electrical conductivities. The scaling is based on the following argument. As long as the characteristic flow time is much longer than the electrical relaxation time, the charge can be drawn

to the surface sufficiently fast to maintain a nearly constant potential. Once the characteristic flow time becomes of the same order as the electrical relaxation time, the constant potential can no longer be maintained, and the jet forms. The characteristic flow time can be obtained from the continuity equation, assuming purely conical sink flow:

$$v = \frac{Q}{2\pi(1 - \cos \alpha)r^2} = -\frac{dr}{dt} \quad (5.19)$$

where  $v$  is the radial flow velocity and  $r$  is the polar radius. Separating terms containing  $r$  on one side and integrating both sides of the equation yields an expression for the characteristic flow time:

$$t_f \sim \frac{r^3}{Q} \quad (5.20)$$

The electrical relaxation time can be estimated by considering a fluid interface with charge density  $\sigma$  at the surface with external and internal normal electric fields  $E_n^o$  and  $E_n^i$  respectively. The fields can be related to the charge density by applying Gauss's theorem to a pill-box across the interface:

$$\sigma = \epsilon_0(E_n^o - \epsilon E_n^i) \quad (5.21)$$

where  $\sigma$  is the surface charge density and  $\epsilon$  is the dielectric constant. Assuming that the internal field  $E_n^i$  drives the charge to the surface, the rate of charge arrival per unit area can be written as:

$$\frac{d\sigma}{dt} = K E_n^i \quad (5.22)$$

where  $K$  is the electrical conductivity. Solving for  $E_n^i$  from Eqn. 5.21 and substituting into Eqn. 5.22 produces a linear differential equation for  $\sigma$ :

$$\frac{d\sigma}{dt} + \sigma \left( \frac{K}{\epsilon \epsilon_0} \right) = \frac{E_n^o K}{\epsilon} \quad (5.23)$$

The time constant characterizing variations of the charge density with time can be extracted from Eqn. 5.23:

$$t_e = \frac{\epsilon \epsilon_0}{K} \quad (5.24)$$

The characteristic jet size can now be obtained by equating the electrical relaxation time  $t_e$  to the characteristic flow time  $t_f$ :

$$\frac{\epsilon\epsilon_0}{K} \sim \frac{r^3}{Q} \quad (5.25)$$

and solving for the radius  $r = r^*$ :

$$r^* \sim \left( \frac{\epsilon\epsilon_0 Q}{K} \right)^{1/3} \quad (5.26)$$

An alternative analysis can be performed to show that the grouping in Eqn. 5.26 can, in fact, be attributed to the loss of equipotentiality and the failure of Taylor's model. Suppose Taylor's solution is satisfied far enough away from the tip so that  $E_n^o \gg E_n^i$  and the surface charge density can be approximated as:

$$\sigma \approx \epsilon_0 E_n^o \quad (5.27)$$

where the external normal field  $E_n^o$  is given by Eqn. 5.16. The current convected at the surface can be determined from the following relationship:

$$I_s = 2\pi r \sin \alpha \sigma v_s \quad (5.28)$$

where  $I_s$  is the convective current and  $v_s$  is the fluid velocity at the surface and is given by Eqn. 5.19. Substituting Eqns. 5.16, 5.19, and 5.27 into Eqn. 5.28 gives the following expression for the convective current:

$$I_s = \left( \frac{Q \sin \alpha \sqrt{2\gamma\epsilon_0 \cot \alpha}}{1 - \cos \alpha} \right) \frac{1}{r^{3/2}} \quad (5.29)$$

Since the charge is driven from the core to the surface by means of the internal normal field  $E_n^i$ , the rate at which charge is deposited to the surface per unit length is given by:

$$\frac{dI_s}{dr} = -2\pi r \sin \alpha K E_n^i \quad (5.30)$$

Substituting Eqn. 5.29 into Eqn. 5.30 and solving for  $E_n^i$  yields:

$$E_n^i = \left( \frac{3Q\sqrt{2\gamma\epsilon_0 \cot \alpha}}{4\pi K(1 - \cos \alpha)} \right) \frac{1}{r^{7/2}} \quad (5.31)$$

This equation indicates that the internal field  $E_n^i$  varies as  $1/r^{7/2}$  while the external field  $E_n^o$  varies as  $1/r^{1/2}$ . Thus, the external field dominates for sufficiently large values of  $r$ , as expected, however, in the vicinity of the tip, where  $\epsilon E_n^i$  becomes of the same order as  $E_n^o$ , the contribution from the internal field to the Gauss's law in Eqn. 5.21 can no longer be ignored and the stress balance assumed in the Taylor's model no longer applies. Setting  $E_n^o \sim \epsilon E_n^i$ :

$$\sqrt{\frac{2\gamma \cot \alpha}{\epsilon_0}} \frac{1}{r^{1/2}} \sim \epsilon \left( \frac{3Q\sqrt{2\gamma\epsilon_0 \cot \alpha}}{4\pi K(1 - \cos \alpha)} \right) \frac{1}{r^{7/2}} \quad (5.32)$$

and solving for the characteristic polar radius  $r$  yields:

$$r^* = \left( \frac{3}{4\pi(1 - \cos \alpha)} \right)^{1/3} \left( \frac{\epsilon\epsilon_0 Q}{K} \right)^{1/3} \quad (5.33)$$

Evaluating the numerical constant for  $\alpha = 49.29^\circ$  yields an estimate of the characteristic jet size:

$$r^* \approx 0.88 \left( \frac{\epsilon\epsilon_0 Q}{K} \right)^{1/3} \quad (5.34)$$

which is in close agreement to a similar estimate obtained earlier in Eqn. 5.26. This scaling law has been validated in a number of experimental studies by F. de la Mora [15], [14] for a variety of fluid solutions with different electrical conductivities and at different flow rates. The reported ratio of the measured jet radius to  $r^*$  averages at a constant value of approximately 0.2. It is believed, based on these results, that the charge relaxation hypothesis presented in this section provides a workable explanation for the basic mechanism responsible for the formation of the jet and lays the necessary groundwork for further modeling.

As discussed earlier, the convective current, which is generally considered to be small along the majority of the conical surface, becomes dominant in the vicinity of

the tip as more and more charge is drawn to the surface by the normal internal field. The value of the convective current in the vicinity of the jet can be estimated by evaluating the expression for  $I_s$  in Eqn. 5.29 at  $r = r^*$ :

$$I_s^* \approx \frac{\sin \alpha \sqrt{2 \cot \alpha}}{1 - \cos \alpha} \left( \frac{\gamma Q K}{\epsilon} \right)^{1/2} \quad (5.35)$$

Although there is no firm theoretical basis for this result, experimental evidence [15] for a variety of solutions with different fluid parameters strongly suggests that the total current collected at the extractor plate scales with the quantity  $(\gamma Q K / \epsilon)^{1/2}$  found in Eqn. 5.35 with good accuracy:

$$I = f(\epsilon) \left( \frac{\gamma Q K}{\epsilon} \right)^{1/2} \quad (5.36)$$

where  $f(\epsilon)$  is some empirically determined function of  $\epsilon$  which ranges in value anywhere between 15 and 25 for polar solutions ( $\epsilon > 40$ ). This result indicates that, sufficiently close to the jet, the relative proportions of the conductive and the convective currents to the overall current  $I_0$  are independent of the operating conditions and depend only on the dielectric constant  $\epsilon$ . More importantly, it shows that the emitted current is independent of the applied voltage and depends only on the flow rate and the fluid properties. Just as an indicator, for some of the fluid solutions used in the experiments by F. de la Mora, the resultant fraction of the convective to the overall current at  $r = r^*$  was estimated to be on the order of 0.01. This suggests that the majority of the total current at  $r^*$  is still carried by conduction and that the correlation  $I_0 \sim I_s$  implied by Eqn. 5.36 is not automatic, but is rather a consequence of an as yet unknown mechanism.

### 5.3.3 Production of droplets

It was concluded, based on the Taylor's model, that the meniscus surface, once formed, maintains stress equilibrium at the surface between the surface tension and electrostatic traction. Presumably, such equilibrium is still satisfied throughout the menis-

cus, including the jet. It is assumed here, just as before, that as  $r$  approaches  $r^*$  and beyond into the jet, both surface tension and electrostatic traction dominate over the internal pressure, so that it can still be ignored in the stress balance. The internal pressure does contribute to the axial momentum balance in the jet, however, this effect will be addressed in more detail in Chapter 7. Once the jet starts breaking up into droplets as a result of the classical Rayleigh-Taylor instability, it is reasonable to assume that the droplets are produced such as to maintain this same stress balance. Assuming perfectly spherical droplets of radius  $R_d$  carrying charge  $q$ , the electric field at the surface of such droplet is given by:

$$E_s = \frac{q}{4\pi\epsilon_0 R^2} \quad (5.37)$$

so that the stress balance at the surface can be written as:

$$\frac{2\gamma}{R} = \frac{\epsilon_0}{2} \left( \frac{q}{4\pi\epsilon_0 R^2} \right)^2 \quad (5.38)$$

Since the mass of each droplet is equal to  $4/3\pi R^3 \rho$  the charge to mass ratio is given by:

$$\frac{q}{m} = \frac{6(\epsilon_0\gamma)^{1/2}}{\rho R^{3/2}} \quad (5.39)$$

This expression gives the maximum attainable charge that can be accumulated on a droplet of a given mass. In the earlier discussion, such operation was referred to as the “Rayleigh limit”. In reality, however, experimental measurements of droplet size versus charge to mass ratio in glycerol and octoil solutions [9] indicate that the majority of droplets of a given mass carry charge almost universally half of that predicted by Eqn. 5.39. An alternative derivation of the charge to mass ratio does exist in references [9], [36]. It is based on the argument that the amount of charge carried by each droplet is such as to minimize the sum of the electrostatic and the elastic energy due to surface tension of an assembly of drops with a given total mass and total charge. This alternative derivation produces a result identical to that in Eqn. 5.39, however, with an additional factor of 2 in the denominator. The prediction

based on the minimum-energy argument does correlate well with the data, however, since it ignores the unsteady nature of droplet production and due to the lack of a firm theoretical foundation it will not be detailed here.

Experimental data also indicates [15], [14] that the jet breaks up into droplets in accordance with the classical Rayleigh-Taylor criterion. Although the classical form of the stability criterion only applies to the cases of uncharged jets, empirical evidence strongly suggests that it is still applicable in the presence of electrostatic traction at the surface. This result can be, at least conceptually, motivated by the fact that the Rayleigh-Taylor criterion is independent of the surface tension coefficient, and should, in principle, hold even for small values of  $\gamma$ . Since the presence of electrostatic traction effectively reduces the value of  $\gamma$  to nearly zero, it is not unreasonable to believe that the Rayleigh-Taylor criterion would still apply. A more detailed analysis of the jet instability in the presence of surface charges was performed by M. Martinez-Sanchez and is detailed in Ref. [38]. Imposing the criterion to obtain the most unstable wavelength and converting the resultant cylindrical volume into a spherical droplet results in the following relationship between the jet and the droplet radii:

$$\frac{R_j}{R_d} \approx 1.89 \quad (5.40)$$

Knowing the characteristic radius of the jet from Eqn. 5.34 together with Eqn. 5.40 the charge to mass ratio on each droplet is given by:

$$\frac{q}{m} \approx \frac{15.7}{\rho} \left( \frac{\gamma K}{Q\epsilon} \right)^{1/2} \quad (5.41)$$

Just to close the argument, for consistency, a similar result can be obtained from the expression for the total current:

$$\frac{q}{m} = \frac{I}{\rho Q} = \frac{f(\epsilon)}{\rho} \left( \frac{\gamma K}{Q\epsilon} \right)^{1/2} \quad (5.42)$$

which is in agreement with Eqn. 5.41 if  $f(\epsilon) = 15.7$  (recall the empirical  $f(\epsilon) \sim 18 - 25$ ). Although a more detailed discussion of the numerical results is to follow, it

is worth noting here the attainable values of  $q/m$  for a typical solution of formamide with  $K = 1$  Si/m,  $\gamma = 0.06$  N/m,  $\rho = 1,100$  kg/m<sup>3</sup>, and  $Q = 10^{-14}$  m<sup>3</sup>/s. This value of the flow rate has been chosen such as to be just above the minimum stable flow rate, an operational limitation which will be discussed in detail in the following section. Substituting the values into Eqn. 5.42 yields a charge to mass ratio on the order of 5,570 C/kg. Just to put this number in perspective, in order to achieve an  $I_{sp}$  of 1,000 sec these droplets would have to be accelerated through a potential difference of about 8.6 kV.

### 5.3.4 Regimes of operation

The results of the experiments [15], [14] indicate that high-conductivity solutions produce stable cone-jets over a specific range of operating conditions. The minimum voltage required to initiate the surface instability was already discussed earlier in this Chapter. Once the applied voltage exceeds the minimum required value, the fluid surface assumes a conical shape and the operating characteristics of the spray are controlled by the fluid properties and the flow rate. It should be noted that for a given electrode geometry and pressure, there is only one value of the applied voltage for which the resultant shape is purely conical. Experimentally, the fluid meniscus was observed to be stable within a narrow range of applied voltages for which the emitted current was nearly independent of the voltage [8], [13]. Some of the operational limitations which depend on the choice of the working fluid and the flow rate are discussed below.

It was assumed in most of the prior discussions that the flow velocity within the cone and near the tip was sufficiently low so that fluid inertia never contributed to the force balance and, hence, never effected the operation of a cone-jet. In order to quantify the effect of fluid inertia, it is useful to consider the interplay of the three dominant pressure components: the surface tension, dynamic pressure, and the tangential electrostatic stress. It is assumed here that the surface tension balances the normal electrostatic traction and the internal pressure at all times. Since the internal pressure is nearly constant and becomes insignificant near the tip, sufficiently close to

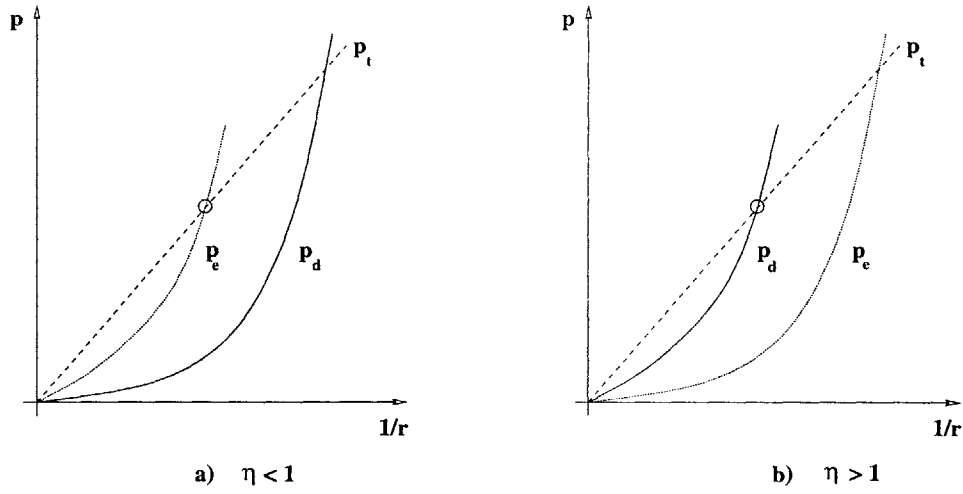


Figure 5-2: Operating regimes: a) charge relaxation effect, b) dynamic pressure effect

it, surface tension and electrostatic traction must scale in proportion. The dynamic pressure expressed in terms of the polar radius scales as:

$$p_d \sim \rho v^2 \sim \rho Q^2 \left(\frac{1}{r}\right)^4 \quad (5.43)$$

The stress due to surface tension scales as:

$$p_t \sim \gamma \left(\frac{1}{r}\right) \quad (5.44)$$

Finally, the normal electrostatic stress in the axial direction scales as  $\epsilon\epsilon_0 E_t^2$ :

$$p_e \sim \epsilon_0 \left(\frac{I}{K r^2}\right) \sim \frac{\epsilon\epsilon_0 Q \gamma}{K} \left(\frac{1}{r}\right)^4 \quad (5.45)$$

Clearly, the radial electrostatic stress scales similarly with the dynamic pressure, hence, it is useful to introduce a dimensionless parameter  $\eta^2$  as an indicator of the relative magnitudes of the dynamic pressure in comparison to the axial electrostatic stress:

$$\eta^2 = \frac{\rho Q K}{\gamma \epsilon_0 \epsilon} \quad (5.46)$$

The three pressure components are plotted versus  $1/r$  for two different cases in Fig. 5-2. Operation at small values of  $\eta$  (see Fig. 5-2 a) implies that inertia is not important and the charge relaxation limit  $p_t \approx p_e$  is reached first with decreasing  $r$ . Incidentally, since surface tension scales with normal electrostatic traction, setting  $p_t = p_e$  yields

the scale length for which internal field becomes of the same order as the normal external field, recovering the previously obtained scaling for the characteristic jet size:

$$\frac{\gamma}{r} = \frac{\epsilon\epsilon_0 Q \gamma}{K r^4} \quad (5.47)$$

or

$$r^* = \left( \frac{\epsilon\epsilon_0 Q}{K} \right)^{1/3} \quad (5.48)$$

This regime of operation is the one reported in [15] to most closely resemble that of Taylor's solution and which breaks down only very close to the tip when  $r \rightarrow r^*$ . Alternatively, when  $\eta > 1$ , corresponding to the operation at high flow rates (see Fig. 5-2 b) the charge relaxation limit is never attained and the cone-jet is nearly equipotential. Instead, the dynamic pressure takes over first when  $p_d \approx p_t$  or:

$$\frac{\gamma}{r} = \rho Q^2 \left( \frac{1}{r} \right)^4 \quad (5.49)$$

Solving for the characteristic radius  $R^*$  corresponding to the limit in which inertia dominates yields the following expression:

$$R^* = \left( \frac{\rho Q^2}{r} \right)^{1/3} = \eta^{2/3} r^* \quad (5.50)$$

Operation in the regime  $\eta > 1$  was observed and reported in Ref. [14]. It was concluded that for sufficiently large values of  $\eta$ , the jet size was no longer dependent upon the electrical conductivity of the solution, as suggested by the data and as can be verified from Eqn. 5.50. The values of  $\eta$  for which such transition occurred in the experiments with formamide ranged anywhere between 8 and 10.

On the opposite end of the spectrum, it was observed that there exists a minimum flow rate below which operation was no longer stable. The existence of such a lower bound on the flow rate was first analyzed in Ref. [36] and can be understood from the following basic argument. As observed from Eqn. 5.42, the amount of charge accumulated on each droplet increases with decreasing flow rate. In principle, therefore, by operating at sufficiently low flow rates, arbitrarily high charge to mass ratios

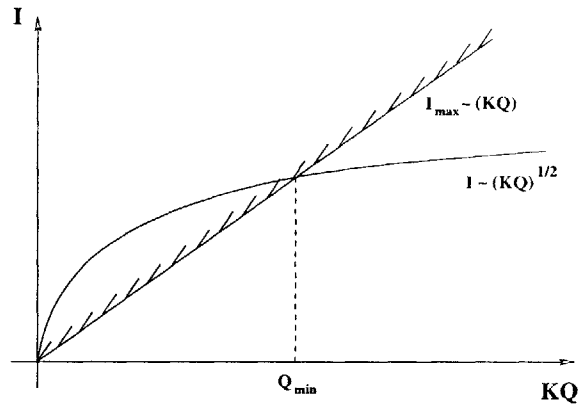


Figure 5-3: Onset of the minimum flow rate (boundary indicates maximum allowable current for a given flow rate)

could be attained. Since the charge on each droplet comes from the dissociated ions in the electrolyte solution, it is not possible to extract in steady state more ions of one polarity per unit mass than are available in the solution. The amount of charge available per unit mass can be estimated from the concentration of dissociated ions  $C$  (moles/l):

$$\left(\frac{q}{m}\right)_{max} = \frac{I_{max}}{\rho Q} = \frac{1000eN_A C}{\rho} \quad (5.51)$$

where  $N_A$  is the Avogadro's number and  $e$  is the charge of an electron. The concentration of ions in aqueous solutions can be related to the electrical conductivity  $K$  through an equivalent molar conductivity parameter (mobility)  $\Lambda_0$  tabulated in Ref. [39] for a variety of aqueous solutions. For many electrolyte solutions with low viscosity containing ions other than those of hydrogen, the values of  $\Lambda_0$  range anywhere between 12 and 15 ( $Si/m$ )( $l/mole$ ) at room temperature. It will be shown shortly that the mobility is inversely proportional to fluid's viscosity, so that the values of  $\Lambda_0$  for highly viscous solutions (such as glycerol) may be significantly smaller. The maximum current for a given flow rate can be expressed as:

$$I_{max} = \left(\frac{1000eN_A}{\Lambda_0}\right) KQ = 1000eN_A CQ \quad (5.52)$$

As intuition suggests, the maximum attainable current is only dependent on the flow rate and the concentration of the dissociated ions. Alternatively, for any given

current, Eqn. 5.52 gives the minimum flow rate which is required to provide sufficient concentration of ions to maintain such current. The existence of an operational minimum flow rate is graphically illustrated in Fig. 5-3. Plotted are the expected current for a given flow rate  $I \sim (Q)^{1/2}$  from Eqn. 5.42 and the maximum allowed current  $I_{max} \sim Q$  from Eqn. 5.52. Clearly, there is a value of  $Q_{min}$  for which the two values are equal:

$$Q_{min} = \frac{\gamma}{\epsilon K} \left( \frac{\Lambda_0 f(\epsilon)}{1000eN_A} \right)^2 = \frac{\gamma f^2(\epsilon)}{\epsilon} \frac{\Lambda_0}{(1000eN_A)^2 C} \quad (5.53)$$

and at which all of the charge of one polarity is extracted in the droplets and below which no additional current can be drawn. It was experimentally observed that near  $Q_{min}$  the cone became unstable and the jet intermittently appeared at the tip. The resultant current obtained at the minimum flow rate can be determined by substituting Eqn. 5.53 into Eqn. 5.52:

$$I(Q_{min}) = \frac{\gamma f^2(\epsilon)}{\epsilon} \frac{\Lambda_0}{(1000eN_A)} \quad (5.54)$$

In order to support the above hypothesis with the data, the characteristic quantity  $\eta$  corresponding to the minimum stable flow rate can be correlated with the data reported from the experiments by de la Mora [15], [14] for a variety of low-viscosity fluid solutions and electrical conductivities. Almost universally, the minimum attainable values of  $\eta$  were on the order of 1/2. Extracting  $\eta$  from Eqn. 5.53 in terms of the fluid properties yields:

$$\eta_{min} = \left( \frac{\rho Q K}{\gamma \epsilon \epsilon_0} \right)^{1/2} = \frac{\Lambda_0 f(\epsilon)}{1000eN_A \epsilon} \sqrt{\frac{\rho}{\epsilon_0}} \quad (5.55)$$

Just for the purposes of illustration, for formamide solutions used in the experiments with  $\epsilon = 100$ ,  $f(\epsilon) = 25$ ,  $\Lambda_0 \approx 15$  (Si/m)(l/mole), and  $\rho = 1100$  kg/m<sup>3</sup> the value of  $\eta_{min}$  is on the order of 0.43, in close agreement with the data. Incidentally, the

maximum attainable value of  $q/m$  is given by:

$$\left(\frac{q}{m}\right)_{max} = \frac{f(\epsilon)K}{\eta_{min}\epsilon\sqrt{\rho\epsilon_0}} = \frac{(1000N_Ae)C}{\rho} \quad (5.56)$$

which is a function of the fluid properties only. For the formamide solution, considered above, with the electrical conductivity of 2 Si/m and  $\eta_{min} = 1/2$  the maximum attainable charge to mass ratio is on the order of 10,000 C/kg. Such droplets would have to be accelerated across a 5 kV potential difference to achieve an  $I_{sp}$  of 1,000 sec.

Although the minimum flow rate obtained for most low-viscosity solutions (such as those with formamide, ethylene glycol, and water) have been shown to agree quantitatively with the values predicted by Eqn. 5.53, much lower values of  $Q_{min}$  were observed for highly viscous solutions of glycerol in the work by Perel et al [11], [12], [13]. Although still consistent with Eqn. 5.53, it was reported that even low-conductivity solutions were capable of producing ions (see Sec. 5.4), i.e. were able to operate at sufficiently low flow rates for the surface field to reach critical values required for field ionization. This anomaly instigated the question of whether or not viscosity plays any role in determining  $\eta_{min}$  (Eqn. 5.55). Using Stokes approximation in a simplified model for the motion of ions, each carrying charge  $ez_i$ , the balance of the drag force against the electrostatic force yields:

$$6\pi\mu v_i R_i \approx ez_i E \quad (5.57)$$

where  $v_i$  is the drift speed of ions and  $R_i$  is the radius of each ion. The mobility of the ions of each polarity is, therefore, given by:

$$\Lambda_i = \frac{v_i}{E} = \frac{ez_i}{6\pi\mu R_i} \quad (5.58)$$

In terms of the respective mobilities of the positive and the negative ions, assuming electrical neutrality  $z^+n^+ = z^-n^-$ , the electrical conductivity can be expressed as

follows:

$$K = (\Lambda^+ + \Lambda^-)ez^+n^+ \quad (5.59)$$

Since the equivalent molar mobility  $\Lambda_0$  is equal to  $K/C$ , and  $z^+n^+ = (1000N_A C)$  then:

$$\Lambda_0 = 1000N_A e(\Lambda^+ + \Lambda^-) \quad (5.60)$$

Substituting Eqn. 5.58 for both the positive and the negative ion mobilities produces the following expression for  $\Lambda_0$ :

$$\Lambda_0 = \frac{1000N_A e^2}{6\pi\mu} \left( \frac{z^+}{R^+} + \frac{z^-}{R^-} \right) \quad (5.61)$$

Although at the atomic dimensions Stokes model may be too crude to yield quantitatively accurate results, Eqn. 5.61 clearly shows the dependence of the ion mobility on viscosity. Since  $\eta_{min} \sim \Lambda_0$  and  $\Lambda_0 \sim 1/\mu$ , the minimum flow rate for more viscous solutions will generally be lower. This result does provide a plausible explanation for the anomalous ion emission observed for viscous glycerol solutions, however, due to the lack of sufficient data for these fluids, the correlation  $\eta_{min} \sim 1/\mu$  can not be experimentally justified at this time. A more detailed discussion of the criterion for the onset of ion emission and the effects of viscosity can be found in the following section.

## 5.4 Ion emission

Thus far, a complete description of the cone-jet physics has been presented. Starting with a set of fluid properties and operating conditions, the droplet size and the charge to mass ratio could be predicted at once. Given the applied voltage, the flow rate, and the charge to mass ratio, the thrust and the specific impulse of a particular emitter could be determined. Although the qualitative model presented above is still to be justified for the cases of highly viscous fluids (such as glycerol), it does correlate extremely well with the data obtained for high-conductivity solutions of formamide,

ethylene glycol, tri-ethylene glycol, octanol, and water with various salts of lithium, sodium, sulfuric acid and other electrolytes. It was shown that the maximum attainable charge to mass ratio for the majority of these fluids was limited by the onset of the minimum flow rate (complete ion extraction) to values not exceeding 10,000 C/kg.

Additional experiments with highly conductive solutions of formamide, however, have shown that under certain conditions, with flow rates just above the minimum, the extracted current greatly exceeded that predicted by Eqn. 5.38 and was very sensitive to the flow rate. This phenomenon was later attributed to the emission of ions directly from the surface of the meniscus near the tip as observed in numerous experiments by Gamero [17]. It was determined that at low flow rates the normal field at the tip could reach sufficient magnitudes to initiate field ionization. This process may be of significance from the propulsion standpoint, since pure ions have much larger charge to mass ratio than what can be practically attained with droplets alone. Hence, operation with ions and droplets simultaneously may lower the overall voltage requirements and still produce the desired specific impulse.

The problem of ion evaporation was first studied by Iribarne and Thomson [40] and was treated as a kinetic process in which an escaping ion would have to overcome a potential barrier  $\Delta$  so that the current density of ions can be written as:

$$j = \frac{kT}{h} \sigma e^{-\frac{\Delta}{kT}} \quad (5.62)$$

where  $\sigma$  is the surface charge density. In the absence of the electric field  $\Delta$  coincides with the free energy of solvation for the ion:  $\Delta G$ . More generally, however,  $\Delta$  is reduced due to the presence of an external electric field, similar to what is known as the Schottky effect in the realm of solid state electronics. Including the contribution due to the image charge, the overall potential barrier that a singly charged ion has to overcome is given by:

$$\Delta(y) = \Delta G - eEy - \frac{e^2}{16\pi\epsilon_0 y} \quad (5.63)$$

where  $y$  is the distance from the surface. The peak of the potential  $\phi(y)$  occurs at:

$$y_{max} = \left( \frac{e}{16\pi\epsilon_0 E} \right)^{1/2} \quad (5.64)$$

with the peak value modified from that in the absence of the field by the so-called Schottky hump:

$$\Delta = \Delta G - \left( \frac{e^3 E}{4\pi\epsilon_0} \right)^{1/2} \quad (5.65)$$

It can be inferred from Eqn. 5.62, that in order to initiate ion emission  $\Delta$  must be small, so that:

$$\Delta G \sim \left( \frac{e^3 E}{4\pi\epsilon_0} \right)^{1/2} \quad (5.66)$$

or solving for the critical electric field:

$$E_{cr} \sim \frac{4\pi\epsilon_0 \Delta G^2}{e^3} \quad (5.67)$$

The experimentally measured values of solvation energy  $\Delta G$  for a variety of ions solvated in ethylene glycol and formamide are on the order of 1-2 eV. From Eqn. 5.67 the corresponding values of the external field required to initiate ion emission range anywhere between 1-2 V/nm. Extensive experimental measurements by Loscertales and de la Mora [29], and later by Gamero [17] indicate that the minimum required field for ion emission for nearly all fluid/ion combinations utilized in the experiments was on the order of 1.1-1.2 V/nm.

It can be readily seen from Eqn. 5.62 that the emitted current is very sensitive to the applied electric field, so that once the critical field is reached, the ion current will almost invariably dominate over the jet current. It can also be seen that since the electric field at the tip is a function of the local radius and the jet size is determined by the supplied flow rate (Eqn. 5.48), the resultant ion current can be controlled by proper adjustments of the flow rate alone. Assuming that the majority of the ions are emitted in the vicinity of the neck at  $r \approx 3R_j$  (where  $R_j$  is the jet radius) and using the empirical correlation for jet radius,  $R_j \sim 0.2r^*$  together with Eqns. 5.16 and

5.48 and solving for the flow rate in terms of the critical field  $E_{cr}$  yields the following expression:

$$Q_{cr} \approx \frac{(3\gamma \cot \alpha)^3 K}{\epsilon \epsilon_0^4 E_{cr}^6} = \frac{(3\gamma \cot \alpha)^3 \Lambda_0 C}{\epsilon \epsilon_0^4 E_{cr}^6} \quad (5.68)$$

The corresponding charge to mass ratio of the droplets at  $Q = Q_{cr}$  is then given by:

$$\left(\frac{q}{m}\right)_{cr} = \frac{f(\epsilon)}{\rho} \left( \frac{\epsilon_0^2 E_{cr}^3}{(3\gamma \cot \alpha)^{3/2}} \right) \quad (5.69)$$

It should be noted that  $Q_{cr}$  depends only on the fluid properties and, as will be seen shortly, numerically corresponds to extremely low values of the flow rate. Thus, for some fluid combinations the onset of the minimum flow rate can occur before  $Q_{cr}$  and the regime in which ions are emitted can never be reached. Hence, for ions to be emitted the critical flow rate has to be greater than the minimum:

$$Q_{cr} > Q_{min} \quad (5.70)$$

or, using Eqns. 5.53 and 5.68:

$$\frac{(3\gamma \cot \alpha)^3 K}{\epsilon \epsilon_0^4 E_{cr}^6} > \frac{\gamma}{\epsilon K} \left( \frac{\Lambda_0 f(\epsilon)}{1000eN_A} \right)^2 \quad (5.71)$$

Solving for the electrical conductivity in terms of the remaining fluid properties yields:

$$K > \left( \frac{\Lambda_0 f(\epsilon)}{1000eN_A} \right) \frac{\epsilon_0^2 E_{cr}^3}{\gamma (3 \cot \alpha)^{3/2}} \quad (5.72)$$

Since electrical conductivity is proportional to the concentration of ions, Eqn. 5.72 can be rewritten as follows:

$$C > \left( \frac{f(\epsilon)}{1000eN_A} \right) \frac{\epsilon_0^2 E_{cr}^3}{\gamma (3 \cot \alpha)^{3/2}} \quad (5.73)$$

Eqn. 5.73 indicates that only solutions with sufficiently high concentration of dissociated ions (high solubility) will develop a strong enough field at the tip to extract ions by field ionization. It also indicates that neither the mobility nor electrical con-

ductivity affect the onset of ion emission. Just for the purposes of illustration, for formamide with  $f(\epsilon) = 25$ ,  $\epsilon = 100$ ,  $\Lambda_0 = 15$  (Si/m)(1/mole),  $\gamma = 0.059$  N/m the minimum conductivity for which ion emission is possible is on the order of 1.2 Si/m. The charge to mass ratio on each droplet for the same fluid combination evaluated at  $Q = Q_{cr}$  (see Eqn. 5.69) is on the order of 7,000 C/kg. It should be noted that because of the strong dependence of  $K$  on the critical field  $E_{cr}$  and on the characteristic dimension of the neck where ion emission takes place, Eqns. 5.72-5.73 are only intended to provide a rough indication of the ranges of conductivities for which ion emission is possible. Although no quantitative correlations of ion emission with conductivity were reported, it was experimentally observed by Loscertales [29], Gamero [17], and Perel [11] that, indeed, only high-concentration (high conductivity or low mobility) solutions were capable of producing ions.

Eqn. 5.72 demonstrates another important point. The threshold value of the electrical conductivity for which ion emission occurs is proportional to the ion mobility  $\Lambda_0$  which was shown to vary inversely with fluid's viscosity. Thus, the threshold values of  $K$  for more viscous solutions would generally be lower than those for less viscous solutions, explaining the anomalous emission of ions observed in the experiments by Perel et al [11], [12], [13]. It can be concluded from Eqns. 5.53 and 5.68 that for any solution with a fixed ion concentration,  $Q_{min}$  and  $Q_{cr}$  are both proportional to  $\Lambda_0$ , hence both flow rates will decrease with increasing viscosity (or decreasing temperature) in proportion. The process of ion emission is schematically illustrated in Fig. 5-4 for a given solution with fixed fluid properties. The dashed curve shows the nominal dependence of the current vs. flow rate (Eqn. 5.36) in the absence of any ion emission. At the onset of the critical flow rate the current is observed to exponentially rise. The maximum current for a given flow rate and the corresponding minimum flow rate are shown as well. Note that we have assumed  $Q_{cr} > Q_{min}$ .

### 5.4.1 Mixed-regime operation

As analyzed in [36] and demonstrated in the previous section, high-concentration solutions operated at sufficiently low flow rates ( $Q \sim Q_{cr}$ ) are capable of producing

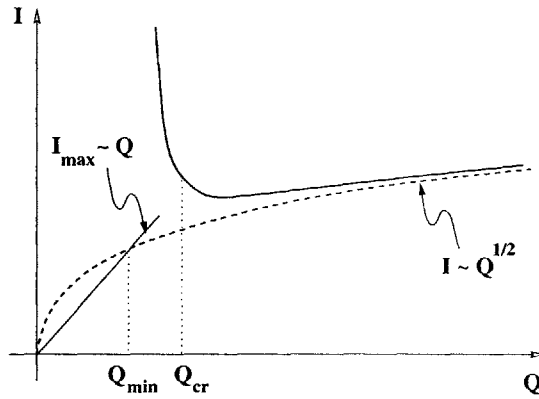


Figure 5-4: Onset of ion emission (dashed line indicates the current obtained in the absence of ion emission)

ions by field ionization extracted directly from the surface of the meniscus. The purpose of this section is to present a quantitative model of the so-called mixed-regime mode of operation in which both the droplets and the ions are produced simultaneously. The goal is to predict the performance of such an emitter and to point out its limitations. It should be noted that although droplets and ions have been experimentally observed to co-exist, the effect of ion emission on the production of droplets is not well understood. It is, therefore, assumed throughout the discussion that ions and droplets form independently and that excessive ion current does not influence the generation of droplets. It is further assumed that since the ion current is extremely sensitive to the flow rate (see Fig. 5-4), any desirable fraction of the ion current can be obtained at a nearly constant flow rate  $Q \approx Q_{cr}$ .

The ability to produce ions with extremely high charge to mass ratio together with droplets has an advantage of increasing the mean specific impulse of the device while still maintaining a sufficiently low operating voltage. As a result, particles with two very different values of the charge to mass ratio are accelerated through the same potential and, thus, attain very different exhaust speeds. Just as it is the case with any other propulsion device which produces species traveling at different speeds, such an arrangement is energetically suboptimal. This is because proportionally more energy is spent accelerating the faster particles than the extra thrust derived from them. The analysis of polydispersity and its effects on the efficiency of electro-spray

emitters has been originally performed by Hunter [41]. Some of the major results which are useful for estimating the performance of cone-jet emitters in a mixed-regime mode are discussed below in some detail.

The propulsive efficiency can be written in terms of the thrust  $F$ , flow rate  $\dot{m}$ , and the input power  $P$  as follows:

$$\eta = \frac{F^2}{2\dot{m}P} \quad (5.74)$$

The mass flow rate contains contributions from both the ions and the droplets:

$$\dot{m} = \dot{m}_i + \dot{m}_d \quad (5.75)$$

The exhaust speeds of the two species are respectively given by:

$$c_i = \sqrt{2 \left( \frac{q}{m} \right)_i V} \quad (5.76)$$

$$c_d = \sqrt{2 \left( \frac{q}{m} \right)_d V} \quad (5.77)$$

Thus, the total thrust can be expressed in terms of these quantities as follows:

$$F = \dot{m}_i \sqrt{2 \left( \frac{q}{m} \right)_i V} + \dot{m}_d \sqrt{2 \left( \frac{q}{m} \right)_d V} \quad (5.78)$$

Since  $(q/m)_i = I_i/\dot{m}_i$  and  $(q/m)_d = I_d/\dot{m}_d$ , the corresponding mass flow rates can be expressed in terms of the respective currents:

$$\dot{m}_i = I_i \left( \frac{m}{q} \right)_i \quad (5.79)$$

$$\dot{m}_d = I_d \left( \frac{m}{q} \right)_d \quad (5.80)$$

Now using the following definitions:

$$\beta_i = \frac{I_i}{I} \quad 1 - \beta_i = \frac{I_d}{I} \quad \lambda = \frac{\left(\frac{q}{m}\right)_d}{\left(\frac{q}{m}\right)_i} \quad (5.81)$$

and substituting Eqns. 5.78-5.81 into Eqn. 5.74 results in the following expression for the efficiency:

$$\eta = \frac{(1 - (1 - \sqrt{\lambda})\beta_i)^2}{1 - (1 - \lambda)\beta_i} \quad (5.82)$$

The value of  $\lambda$  in Eqn. 5.82 is generally prescribed by the specific fluid solutions and the types of ions which are extracted by field ionization. The ion current fraction  $\beta_i$ , however, can be controlled by minute adjustments of the flow rate about  $Q_{cr}$ . It is apparent from Eqn. 5.82 that the efficiency approaches unity in two extreme cases: when only droplets ( $\beta_i = 0$ ) or only ions ( $\beta_i = 1$ ) are extracted. For  $0 < \beta_i < 1$  the efficiency  $\eta$  is smaller than unity and has a minimum at:

$$\beta_i = \frac{1}{1 + \sqrt{\lambda}} \quad (5.83)$$

corresponding to the minimum efficiency of

$$\eta_{min} = \frac{4\sqrt{\lambda}}{(1 + \sqrt{\lambda})^2} \quad (5.84)$$

The minimum efficiency is equal to unity for a monodisperse case ( $\lambda = 1$ ) and is reduced to zero when  $\lambda \ll 1$  or  $\lambda \gg 1$ . It is clear then, that in order to maintain high efficiencies, the polydispersity ratio  $\lambda$  can not be arbitrarily small. Since the charge to mass ratio of the droplets near  $Q_{cr}$  is fixed by the fluid properties (see Eqn. 5.68), the only way to minimize polydispersity is to extract sufficiently large ions which have correspondingly smaller values of  $(q/m)$ . Just for the purposes of illustration, suppose that large singly-charged tetra-heptyl ammonium ions are extracted from a formamide solution. The molecular weight of such ions is 410 g/mole and their charge to mass ratio is on the order of 230,000 C/kg. Using a conservative estimate for the droplet charge to mass ratio of 6,000 C/kg at  $Q_{cr}$ , the resultant  $\lambda$  is equal to 0.026.

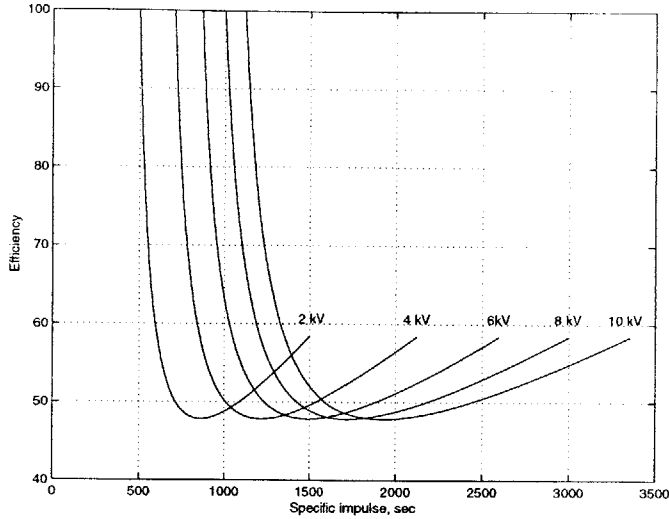


Figure 5-5: Mixed-regime scenario

For this value of  $\lambda$ , the minimum expected efficiency (Eqn. 5.84) is on the order of 48%. It is now possible to compute the mean specific impulse which is given by:

$$I_{sp} = \frac{F}{\dot{m}g} \quad (5.85)$$

Substituting Eqns. 5.78-5.80 into Eqn. 5.85 yields the following expression for the specific impulse:

$$I_{sp} = \frac{1}{g} \sqrt{2V \left( \frac{q}{m} \right)_d} \frac{1 - (1 - \sqrt{\lambda})\beta_i}{1 - (1 - \lambda)\beta_i} \quad (5.86)$$

Fig. 5-5 shows the efficiency as a function of  $I_{sp}$  plotted parametrically as a function of the current fraction  $\beta_i$  for a set of applied voltages ranging between 2 and 10 kV. The minimum value of the efficiency is independent of the voltage and, as previously demonstrated, is approximately equal to 48%. For any given voltage, there are two distinct values of the specific impulse for which the resultant efficiency is the same. If the intended application is not propulsion-intensive and lower values of specific impulse can be tolerated, efficient operation can be achieved to the left of the minimum, where the majority of the extracted particles are droplets. However, for high  $\Delta V$  applications which optimize at substantially larger values of  $I_{sp}$ , efficient operation can only be achieved to the right of the minimum, in the regime for which the majority of the exhaust is ions.

# Chapter 6

## Creeping Flow Model for a Conical Meniscus

### 6.1 Introduction

A conducting fluid supplied to the tip of a capillary of a colloidal emitter is believed to be transported downstream by means of an electrostatic shear stress tangential to the conical surface. This electrostatic pull is created by the tangential component of an internal electric field acting on the ions which reside on the conical surface. Because of the fluid's viscosity, the shear stress propagates to the internal layers of the fluid creating a recirculating flow pattern symmetric with respect to the cone axis. Since the transfer of charge is dominated by convection near the tip, further modeling of charge transport and internal electrostatics requires the knowledge of fluid velocity. In addition, since the flow profile within the conical meniscus may be affected by the fluid's viscosity, understanding its effects on the fluid flow near the tip would provide some guidelines as to the relative importance of viscosity in the regime envisioned for propulsion applications.

As suggested earlier, the desired regime of operation for a cone-jet emitter is the one in which droplets attain maximum possible values of  $q/m$ . It was also shown that under such conditions, the emitter was operated near its minimum flow rate producing droplets several tens of nanometers in diameter. It can be easily shown

that in most such cases the Reynolds number will not exceed unity. For a conical flow the local Reynolds number can be written as:

$$Re = \frac{\rho v 2r}{\mu} \quad (6.1)$$

where  $r$  is the local cone radius,  $v$  is the flow velocity, and  $\mu$  is the viscosity. Using  $v = Q/\pi r^2$  from continuity (to be justified later in this Chapter) the Reynolds number can be written as:

$$Re = \frac{2\rho Q}{\pi \mu r} \quad (6.2)$$

The Reynolds number increases towards the tip and, for a given flow rate, it is the largest near the tip where  $r \sim r^*$ . Evaluating Eqn. 6.2 at  $r = r^*$  (from Eqn. 5.34) and expressing the flow rate as a fraction of the minimum flow rate  $Q_{min}$  (from Eqn. 5.46) the worst-case Reynolds number can be written as follows:

$$Re = \frac{2}{\pi \mu} \left( \frac{\rho \epsilon \epsilon_0 \gamma^2}{K} \right)^{1/3} \eta_{min}^{4/3} \left( \frac{Q}{Q_{min}} \right)^{2/3} \quad (6.3)$$

Using typical values for formamide:  $\mu \sim 4 \times 10^{-3} Pa \cdot s$ ,  $\rho = 1,000 kg/m^3$ ,  $K = 1 Si/m$ ,  $\gamma = 0.05 N/m$  and  $\eta_{min} \sim 0.5$  the Reynolds number is of the order of: -

$$Re \approx 0.08 \left( \frac{Q}{Q_{min}} \right)^{2/3} \quad (6.4)$$

Since operation near  $Q = Q_{min}$  is desired, the Reynolds number is of the order of 0.08. Even at much higher flow rates ( $Q \sim 10Q_{min}$ ) the Reynolds number is approximately 0.37, still below unity. Moreover, it was shown in Chapter 5 that the electrical conductivity  $K$  and  $\eta_{min}$  are both proportional to the ion mobility  $\Lambda_0$  (see Eqn. 5.55) which scales inversely with the fluid's viscosity  $\mu$ . Hence, the maximum value of the Reynolds number based on the jet diameter at the minimum flow rate scales as  $1/\mu^2$  and, thus, is even smaller for more viscous solutions.

At low Reynolds numbers it is possible to formulate the flow problem within the cone utilizing the Stokes approximation in which all of the convective inertia

components are considered small in comparison with viscous forces and can be ignored for the purposes of computation. This approximation eliminates the non-linear terms in the Navier-Stokes equation and makes the problem analytically more tractable.

## 6.2 Model Formulation

The complete solution to the flow problem with arbitrary geometry requires the knowledge of the stress components on the free surface and, therefore, demands coupling with both internal and external electrostatics. Determination of internal and external fields is, in itself, a non-trivial problem and is addressed separately in the next chapter. Without any loss of generality, in order to avoid separate computations of the electric field, a conical surface boundary with a semi-cone angle equal to that of a Taylor's cone will be prescribed a priori. Although for a given electrode configuration and applied voltage the shape of the meniscus is truly conical only for a single value of the internal pressure, it has been experimentally demonstrated (Refs. [15] [16]) that in the regime of interest the free surface does not significantly deviate from that of a cone and, for the purposes of flow analysis, can be well approximated as such.

Anticipating the outcome of this analysis, it should be noted that the shear flow which produces a symmetric recirculating pattern carries zero net flow rate across the cross section of the cone. Due to the linearity of the problem, however, any other flow which satisfies continuity and contributes zero shear at the surface can be superimposed on top of the viscous flow solution to allow for a non-zero flow rate. In order to incorporate the finite flow rate passing through the cross section of the cone, a 3-dimensional sink flow will be added to the viscous solution. The problem is formulated in spherical coordinates with the origin placed at the apex of the cone as shown in the accompanying Figure 6-1. The problem is fully specified by imposing the continuity and the momentum equations:

$$\nabla \cdot \vec{v} = 0 \tag{6.5}$$

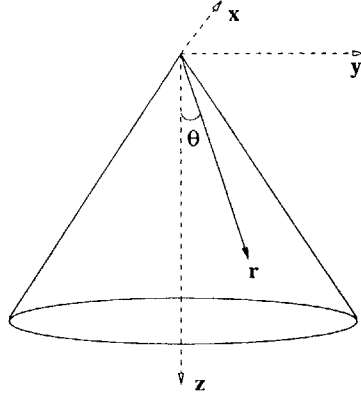


Figure 6-1: Coordinate definitions

$$\frac{\partial \vec{v}}{\partial t} + (\vec{v} \cdot \nabla) \vec{v} = -\frac{1}{\rho} \nabla p + \nu \nabla^2 \vec{v} + \vec{f} \quad (6.6)$$

Neglecting all of the time dependent and convective accelerations, the Navier-Stokes equation becomes:

$$\nabla p = \mu \nabla^2 \vec{v} \quad (6.7)$$

Letting  $\vec{w} = \nabla \times \vec{v}$  and taking the curl of both sides of Eqn. 6.7, the momentum equation reduces to:

$$\nabla \times (\nabla p) = \mu \nabla^2 \vec{w} = 0 \quad (6.8)$$

Due to the axial symmetry of this problem, of the three components of  $\vec{w}$ , only the azimuthal component -  $w_\phi$  is non-zero. Rewriting Eqn. 6.8 in spherical coordinates with  $w_r = w_\theta = 0$  gives:

$$\nabla^2 w_\phi - \frac{w_\phi}{r^2 \sin^2 \theta} = 0 \quad (6.9)$$

or alternatively:

$$\frac{1}{r^2} \frac{\partial}{\partial r} \left( r^2 \frac{\partial w_\phi}{\partial r} \right) + \frac{1}{r^2 \sin^2 \theta} \frac{\partial}{\partial \theta} \left( \sin \theta \frac{\partial w_\phi}{\partial \theta} \right) - \frac{w_\phi}{r^2 \sin^2 \theta} = 0 \quad (6.10)$$

Using separation of variables by introducing the radial and the angular components of  $w_\phi$ , such that:

$$w_\phi = R(r)\Theta(\theta) \quad (6.11)$$

Eqn. 6.10 can be rewritten separately for  $R(r)$  and  $\Theta(\theta)$  as follows:

$$r^2 \ddot{R} + 2r \dot{R} - K^2 R = 0 \quad (6.12)$$

$$\ddot{\Theta} + \dot{\Theta} \cot \theta + \left(K^2 - \frac{1}{\sin^2 \theta}\right) \Theta = 0 \quad (6.13)$$

where  $K$  is an arbitrary separation constant. Eqn. 6.12 is known as Euler's equation whose general solution is of the form:

$$R(r) = C_0 r^p \quad (6.14)$$

while Eqn. 6.13 is a Legendre equation whose general solution can be expressed in terms of Legendre polynomials of order 1 and  $-1$  as follows:

$$\Theta(\theta) = C_1 P_\nu^1(\cos \theta) + C_2 P_\nu^{-1}(\cos \theta) \quad (6.15)$$

where  $\nu^2 + \nu - K^2 = 0$ . Substituting Eqn. 6.14 into Eqn. 6.12 gives  $p^2 + p - K^2 = 0$ , hence  $p = \nu$ . Using the recursion formulas to express Legendre polynomials of order 1 and  $-1$  in terms of the appropriate polynomials of order 0 yields:

$$\Theta(\theta) = C_1 \left\{ \frac{\cos \theta P_\nu - P_{\nu-1}}{\sin \theta} \right\} + C_2 \left\{ \frac{P_{\nu+1} - P_{\nu-1}}{\sin \theta} \right\} \quad (6.16)$$

The complete solution for  $w_\phi(r, \theta)$  is obtained by combining the radial and the tangential functions:

$$w_\phi(r, \theta) = \sum r^p \left( A \left\{ \frac{\cos \theta P_\nu - P_{\nu-1}}{\sin \theta} \right\} + B \left\{ \frac{P_{\nu+1} - P_{\nu-1}}{\sin \theta} \right\} \right) \quad (6.17)$$

The unknown constants A, B, and p can be determined by imposing the necessary stress boundary conditions. The tangential component of the electrostatic stress tensor at the surface of the cone ( $\theta = \theta_0$ ) is given by:

$$\sigma_{r\theta} = \epsilon_0 E_n E_t \quad (6.18)$$

where  $E_n$  is the electric field normal to the surface (see Sec. 5.3.1) and is given by (assuming  $\Delta p = 0$ , as will be explained shortly):

$$E_n = \sqrt{\frac{2\gamma \cot \theta_0}{\epsilon_0 r}} \hat{\theta} \quad (6.19)$$

and  $E_t$  is the tangential electric field created within the fluid due to its finite electrical conductivity and is given by the Ohm's law:

$$E_t = -\frac{I_c}{2\pi(1 - \cos \theta_0)Kr^2} \hat{r} \quad (6.20)$$

where  $I_c$  is the conduction current and  $K$  is the electrical conductivity of the fluid. Conduction current dominates upstream of the tip and is assumed to be constant throughout the cone. Combining Eqns. 6.18, 6.19, and 6.20 results in the following expression for the shear stress:

$$\sigma_{r\theta} = -\sqrt{\frac{\epsilon_0 \gamma \cot \theta_0}{2}} \frac{I_c}{\pi(1 - \cos \theta_0)K} \frac{1}{r^{5/2}} \equiv -\frac{\lambda}{r^{5/2}} \quad (6.21)$$

The shear stress  $\sigma_{r\theta}$  expressed in spherical coordinates in terms of the velocity components  $v_r$  and  $v_\theta$  is given by:

$$\sigma_{r\theta} = \mu \left( \frac{1}{r} \frac{\partial v_r}{\partial \theta} + \frac{\partial v_\theta}{\partial r} - \frac{v_\theta}{r} \right) \quad (6.22)$$

Evaluating the stress at the surface by imposing  $v_\theta = 0$  at  $\theta = \theta_0$ , and combining with Eqn. 6.21 yields:

$$\frac{\mu}{r} \frac{\partial v_r}{\partial \theta} \Big|_{\theta_0} = -\frac{\lambda}{r^{5/2}} \quad (6.23)$$

Luckily, the function  $w_\phi(r, \theta)$  expressed in spherical coordinates and evaluated at the surface contains exactly the quantity in Eqn. 6.23:

$$w_\phi(r, \theta) = \frac{1}{r} \frac{\partial(rv_\theta)}{\partial r} - \frac{1}{r} \frac{\partial v_r}{\partial \theta} = -\frac{1}{r} \frac{\partial v_r}{\partial \theta} = \frac{\lambda/\mu}{r^{5/2}} \quad (6.24)$$

thus reducing the stress boundary condition in the following simplified form:

$$\frac{\lambda/\mu}{r^{5/2}} = \sum r^p \left( A \left\{ \frac{\cos \theta_0 P_\nu - P_{\nu-1}}{\sin \theta_0} \right\} + B \left\{ \frac{P_{\nu+1} - P_{\nu-1}}{\sin \theta_0} \right\} \right) \quad (6.25)$$

Eqn. 6.25 indicates that the boundary condition can be satisfied for one and only one value of  $\nu$ :  $\nu = -5/2$ , hence the summation in Eqn. 6.25 will contain only one term. Imposing continuity by rewriting Eqn. 6.8 in spherical coordinates gives:

$$\frac{\partial v_r}{\partial r} + \frac{2v_r}{r} + \frac{1}{r} \frac{\partial v_\theta}{\partial \theta} + \frac{\cot \theta}{r} v_\theta = 0 \quad (6.26)$$

Since both the continuity and the momentum equations are self-similar in  $r$ , the tangential and the radial velocity components as well as  $w_\phi$  can all be written as products of the corresponding functions of  $\theta$  with proper dependence on  $r$ :

$$v_r = \frac{f(\theta)}{r^{3/2}} \quad (6.27)$$

$$v_\theta = \frac{g(\theta)}{r^{3/2}} \quad (6.28)$$

$$w_\phi = \frac{\Omega(\theta)}{r^{5/2}} \quad (6.29)$$

where

$$\Omega(\theta) = A \left\{ \frac{\cos \theta_0 P_{-5/2} - P_{-7/2}}{\sin \theta_0} \right\} + B \left\{ \frac{P_{-3/2} - P_{-7/2}}{\sin \theta_0} \right\} \quad (6.30)$$

Substituting Eqns. 6.27-6.29 into Eqns. 6.24 and 6.26 yields two differential equations for  $f(\theta)$  and  $g(\theta)$ :

$$-\frac{g(\theta)}{2} - \frac{\partial f(\theta)}{\partial \theta} = \Omega(\theta) \quad (6.31)$$

$$\frac{f(\theta)}{2} + \frac{\partial g(\theta)}{\partial \theta} + g(\theta) \cot \theta = 0 \quad (6.32)$$

These are two coupled ordinary differential equations which can be solved simultaneously subject to the following boundary conditions:

$$g(\theta_0) = 0; \quad g(0) = 0 \quad (6.33)$$

Since  $g(\theta)$  is constrained at the two boundary points  $\theta = (0, \theta_0)$  and no initial conditions are specified for  $f(\theta)$ , an iterative technique is required to obtain such a value of  $f(\theta_0)$  to satisfy both terminal conditions on  $g(\theta)$ . The numerical procedure used to solve for  $g(\theta)$  and  $f(\theta)$  is discussed in the following section.

It should be noted that  $\Omega(\theta)$ , the right hand side of Eqn. 6.31, still contains two yet undetermined constants of integration A, B. The shear stress condition - (Eqn. 6.25), supplies one of the two constraints necessary to determine these constants. The second condition is obtained by setting the radial component of the pressure gradient to zero at the surface of the cone. As discussed in Sec. 5.3.1, the simplest electrostatic solution for which the surface of the fluid is an equipotential, is that of a cone with a semi-cone angle of  $49.29^\circ$ . The surface balance is normally maintained by a three-way equilibrium of surface tension, electrostatic traction, and the normal pressure gradient:

$$\Delta P + \frac{\epsilon_0 E_n^2}{2} = \frac{2 \cot \theta_0}{r} \quad (6.34)$$

Since the surface tension and the electrostatic traction both scale inversely with  $r$ , Eqn. 6.34 is satisfied only if  $\Delta P = 0$ , hence  $(\nabla p)_r = 0$ . It should be noted that for a given voltage, the conical meniscus is experimentally obtained only for a specific value of the internal pressure; i.e. a non-zero surface curvature may contribute to the overall surface stress balance, allowing additional freedom in the electrostatic solution and non-zero pressure variations. This flexibility, although physically more sound, introduces additional complications into the solution and is avoided for the purposes of this analysis. Such deviations from an ideal conical solution can be included by numerically solving for the electrostatic stress on the surface and iteratively reconstructing the surface profile to satisfy the stress balance. The details of this numerical simulation are discussed in Chapter 7.

Assuming that the pressure gradient in the radial direction vanishes at the surface of the cone and using the fact that the gradient is proportional to  $\nabla^2 v$ , setting  $(\nabla^2 v)_r$  to zero at the surface would yield the second constraint between A and B. Expressing the radial component of  $\nabla^2 v$  in spherical coordinates, substituting Eqns. 6.27-6.29,

and evaluating the resultant equation at  $\theta = \theta_0$  gives the following relation:

$$-\frac{5}{4}f(\theta_0) + \cot \theta_0 \left( \frac{\partial f}{\partial \theta} \right)_{\theta_0} + \left( \frac{\partial^2 f}{\partial \theta^2} \right)_{\theta_0} - 2 \left( \frac{\partial g}{\partial \theta} \right)_{\theta_0} = 0 \quad (6.35)$$

Combining Eqns. 6.35 with Eqns. 6.31-6.32 yields the remaining boundary condition:

$$\left( \frac{\partial \Omega}{\partial \theta} \right)_{\theta_0} + \Omega(\theta_0) \cot \theta_0 = 0 \quad (6.36)$$

Fortunately, both constraints on A and B (Eqns. 6.36 and 6.25) are decoupled from the unknown radial velocity component  $f(\theta_0)$ . Therefore, these constraints can be used independently to obtain constants A and B prior to the integration of Eqns. 6.31-6.32. Having obtained the radial and the tangential velocity components,  $v_r$  and  $v_\theta$ , for the shear flow, a radial sink profile with an arbitrary net volumetric flow  $Q$ :

$$v_{sink} = -\frac{Q}{2\pi(1 - \cos \theta_0)r^2} \hat{r} \quad (6.37)$$

can be added to account for the flow transport to the tip.

Although the actual numerical results will be discussed in the following section in some detail, it should be noted that the sink flow scales as  $1/r^2$  while the recirculating shear flow scales as  $1/r^{3/2}$  (Eqns 6.27-6.28). This suggests that sufficiently close to the tip, for small values of  $r$ , sink flow would dominate over the shear flow, and viscosity would have little or no effect near the tip. One way to verify this claim is to locate the stagnation point along the cone axis and compare the radius  $r_{st}$  at which the stagnation point occurs to the characteristic jet radius  $r^*$  observed under similar conditions.

## 6.3 Numerical Procedure and Results

The following is an outline of the inputs, the outputs, and the numerical procedure used to solve for the velocity profile.

**Inputs:** Flow rate ( $Q$ ), charge to mass ratio ( $q/m$ ), viscosity ( $\mu$ ), electrical conduc-

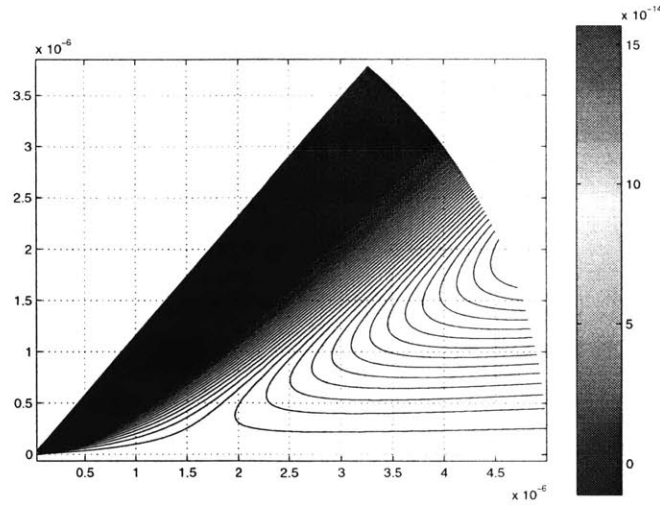


Figure 6-2: Streamline map (horizontal axis is the axis of symmetry, all dimensions given in meters)

tivity ( $K$ ), fluid density ( $\rho$ ), surface tension coefficient ( $\gamma$ ).

**Outputs:** Radial velocity  $v_r(r, \theta)$ , tangential velocity  $v_\theta(r, \theta)$

**Numerical procedure:**

1. Compute  $\lambda/\mu$  (Eqn. 6.21); solve for A and B (Eqns. 6.25, 6.36)
2. Assume  $g(0)=0$ ; guess  $f(0)$ ; integrate Eqns. 6.31-6.32
3. Goto step (2); iterate on  $f(0)$  until  $g(\theta_0) = 0$
4. Compute  $v_r$  and  $v_\theta$  (Eqns. 6.27-6.28)

A typical streamline map for  $(q/m)$  of 5,000 C/kg and a flow rate of  $10^{-14} \text{ m}^3/\text{s}$  in formamide with an electrical conductivity of 1 Si/m is shown in Figure 6-2. The stagnation point can be clearly seen on the axis of the cone near  $z \sim 10^{-6} \text{ m}$ . A similar analysis detailed in Ref. [35] for these conditions gives  $z_{st} \sim 8 \times 10^{-7} \text{ m}$  - in good agreement with the results of the current model. For comparison, the characteristic jet size  $r^*$  for these operating conditions is of the order of  $2 \times 10^{-8} \text{ m}$ , just under two orders of magnitude in radial distance downstream of the stagnation point. This result validates the claim that the viscous shear flow does not influence the region near the tip and shows that viscosity is not a major player in the mechanisms responsible for the formation of the jet. What is left to show is that the result of this specific case can be generalized to other regimes, proving that viscosity has little or no influence over a wide range of operating conditions.

A simple scaling argument can be used to deduce the dependence of  $z_{st}$  on the

fluid properties and other operating parameters, such as the current and the flow rate. It was shown in the previous section that the tangential stress at the surface creates a recirculating shear flow according to Eqn. 6.23. The partial derivative  $\partial v_r / \partial \theta$  scales as  $v_r / \theta_0$ , hence the backward radial velocity due to the shear stress scales as:

$$v_r \sim \frac{\lambda \theta_0}{\mu r^{3/2}} \quad (6.38)$$

The stagnation point occurs when the radial velocity due to the recirculating shear flow becomes on the order of the sink flow velocity:

$$\frac{\lambda}{\mu r^{3/2}} \sim \frac{Q}{r^2} \quad (6.39)$$

Substituting for  $\lambda$ , solving for the characteristic radius  $r \equiv z_{st}$ , and identifying  $I / \rho Q$  as  $q/m$  gives:

$$z_{st} \sim \left( \frac{\mu K}{\rho} \right)^2 \frac{1}{\epsilon_0 \gamma} \frac{1}{(q/m)^2} \quad (6.40)$$

This result indicates that the location of the stagnation point is not dictated by the flow rate alone, but instead scales inversely with the square of the ratio of the current to the flow rate. The importance of the shear flow in the vicinity of the jet can be analyzed by determining the relative location of the stagnation point with respect to the characteristic jet dimension  $r^*$ , i.e. the ratio of  $z_{st}$  to  $r^*$ . Since the droplet size is of the same order as the jet size, the Rayleigh limit for a droplet can be used to express the characteristic jet dimension  $r^*$  in terms of  $q/m$ . Substituting Eqn. 5.39 into Eqn. 6.40 the ratio  $z_{st}/r^*$  can be written as:

$$\frac{z_{st}}{r^*} \sim \frac{(\mu K)^2}{(\rho \epsilon_0 \gamma)^{4/3} (q/m)^{4/3}} \quad (6.41)$$

Using numerical values for a typical formamide solution:  $\mu \sim 10^{-3} Pa \cdot s$ ,  $K = 1 \text{ Si/m}$ ,  $\gamma = 0.05 \text{ N/m}$ ,  $\rho = 1,100 \text{ kg/m}^3$  and  $q/m \sim 5,000 \text{ C/kg}$  the ratio of  $z_{st}$  to  $r^*$  is on the order of 30. Since the value of the charge to mass ratio used in this example is representative of an upper limit of the achievable values of  $q/m$ , any lower value of

this ratio for a given electrolyte concentration would result in the stagnation point located further upstream and, hence, further away from the neck. Moreover, it was shown in Sec. 5.3.4 that the electrical conductivity of the solution is proportional to the ion mobility  $\Lambda_0$  which scales inversely with viscosity. Since the ratio of  $z_{st}$  to  $r^*$  in Eqn. 6.41 contains the product  $\mu K$  and  $(q/m)_{max}$  is independent of viscosity, the relative location of the stagnation point with respect to the neck is independent of viscosity. It is, therefore, safe to assume that under most conditions that may be encountered in the operation of cone-jet emitters, viscous shear flow would have negligible contribution to the local flow pattern and, thus, would have minimal impact on the formation of the jet and production of charged droplets.

# Chapter 7

## Electro-Hydrodynamic Model of a Cone-jet Emitter

### 7.1 Introduction and Literature Survey

The problem of electro-spray physics has been addressed by a number of researchers in the past. Since the use of inorganic electrolyte solutions for propulsion applications was not favored up until recently, most of the prior analytical work in the field was concentrated primarily on the modeling of liquid-metal ion sources. Because of the inevitable coupling of electrostatics with fluid and charge transport processes, all of which control the performance of electro-spray emitters, the enormous complexity of the problem hindered any attempt to develop a complete electrohydrodynamic solution. The existing body of literature addressing the various aspects of ion emitter physics is quite extensive and can not all be cited here. However, a brief survey of the research activities in the area of electro-spray science, emphasizing some of the more successful modeling attempts will be included here for completeness.

Reference [42], for instance, contains a linearized analysis of a nearly conical meniscus, in which the time-dependent fluid equations and the known conical electrostatic solution are both linearized with respect to a small perturbation of the surface from that of an ideal cone. The stability condition for a first-order deformation was derived for various operating conditions indicating the proper time dependence of the angular

perturbation to ensure stability. In addition, a first-order perturbation in the shape of the meniscus was obtained as a function of the applied pressure gradient. Another model is presented in Ref. [43], where a specific analytical shape is prescribed parametrically, and then consistently optimized to satisfy the stress boundary condition at the surface. As a result, an approximate fluid shape was obtained and shown to be consistent with the predictions from other analyses. The main emphasis of this model was on the physics of liquid metal ion sources, hence any finite conductivity effects were ignored assuming a rounded hemispherical meniscus in place of a jet. A numerical model based on the boundary element technique is presented in Ref. [44] in which an external electrostatics solution is obtained for a prescribed electrode/fluid geometry. This model, too utilizes a hemispherical cap at the tip of the meniscus to avoid a numerical singularity. Ref. [45] presents a similar but less restrictive numerical solution to the external electrostatics assuming no fluid flow and using the boundary element method. The fluid surface was assumed to be equipotential and the properly constrained shape of the meniscus was determined as part of the solution by systematically enforcing the stress balance. Singularity near the tip was removed by replacing the terminal panel with a 49.3-degree cone for which the electric potential has a well-known analytical solution. Although the effects of inertia and the internal normal and tangential fields on the stress balance were ignored, the resultant fluid shapes were found to be consistent with the known experimental observations. Ref. [46] presents an asymptotic cone-jet solution for an infinitely long and thin jet. Expressions for the electric current, shape, and charge distribution are obtained in terms of the liquid properties and other operating parameters. This model too assumes the surface of the cone to be equipotential. Ref. [47] contains a quasi-one dimensional formulation for a capillary jet in the limit when charge relaxation effects can be ignored. The model predicts the existence of a convectively unstable region along the jet beyond which the current is independent of the downstream conditions. By far the most sophisticated treatment of the problem is presented in Ref. [35], in which asymptotic solutions of the fluid and electrostatic equations are developed for both the conical meniscus and the jet including fluid inertia and viscosity. Unlike other

similar models, this work also analyzes the contributions from both the external and internal electric fields to the overall stress balance and includes the effects of internal pressure. A number of other attempts have been made to develop analytical, semi-analytical, or fully numerical models addressing one or more aspects of this complex problem (see Refs. [48] [49] [9] [27] [50] [51] [52] [53] [54]).

Although some of the models do incorporate specific mechanisms which, one way or another, determine the operation of a cone-jet, most fail to include a complete set of the mechanisms responsible for the charge and fluid transport. Some make simplifying assumptions which invalidate these solutions in the regimes of interest, others artificially avoid singularities near the tip, thus failing to predict necking and formation of the charged jet. Since the primary objective in the development of a feasible design suitable for propulsion applications is to model the mechanisms ultimately linked to the production and acceleration of charged droplets, a novel approach is needed.

## 7.2 Model description and assumptions

The purpose of this work is to exploit some of the existing modeling ideas to develop a numerical algorithm capable of predicting the formation of the jet. The benefit of such a numerical approach is the added flexibility that it offers in changing the operating conditions, fluid properties, and electrode configurations to suit a specific application. As part of the model, an attempt was made to predict the resulting meniscus shape and the charge to mass ratio - a quantity directly linked to the specific impulse of the device. The following mechanisms were included in the model: a) a full solution to external electrostatics, i.e. charge density for the electrode-needle configuration and fluid meniscus; b) stress balance at the fluid interface: including surface tension, electrostatic traction, inertia, and pressure differential; c) computation of the internal normal field; d) computation of conductive and convective currents; e) computation of the internal tangential field; f) computation of the voltage drop along the fluid interface; g) model of the jet including surface tension, electrostatic traction and

inertia.

For simplicity, all computations except for external electrostatics were kept in the realm of ordinary differential equations. Some of the simplifying assumptions used in the model to make it more tractable are discussed below.

- As shown in Chapter 6, sufficiently close to the tip, fluid velocity is dominated by the sink flow, therefore, convective current near the tip is adequately modeled even if the shear flow is ignored. Since the sum of the convective and the conductive currents remains constant through any cross section of the meniscus, the total current is completely determined by the convective component alone if taken sufficiently close to the tip. Thus, an exact viscous flow solution is not needed in predicting the overall current and can be well approximated as a sink flow throughout the meniscus. Moreover, it should be noted, that the shear flow solution discussed in Chapter 6 is only applicable to an ideal conical surface subject to a prescribed shear stress which was shown to vary as  $1/r^{5/2}$  for the case of an ideal cone. Since in most cases the surface will not necessarily be conical and the surface stress will not scale as  $1/r^{5/2}$ , the flow solution developed in Chapter 6 is not generally applicable to cases with arbitrary geometry.

- Determination of the external electric fields involves the solution of a boundary value problem with prescribed voltages on the fixed electrodes and the iteratively obtained fluid surface. Since it is the surface field which creates traction to balance the surface tension and the pressure gradient and which ultimately determines the shape of the meniscus, complete solution of the Laplace's equation on a grid spanning the whole external region is not economical from the computational standpoint. Instead, a boundary element technique similar to the one discussed in Ref. [45] will be used to compute charge densities on the boundary surfaces of interest.

- It is assumed that the current density which determines the conduction current is uniform throughout any cross section of the meniscus.

- In order to reduce the computational load involved in the grid generation and solution for external electrostatics, the model was developed to handle only cylindrically symmetric geometries. The main disadvantage of this approach is that it

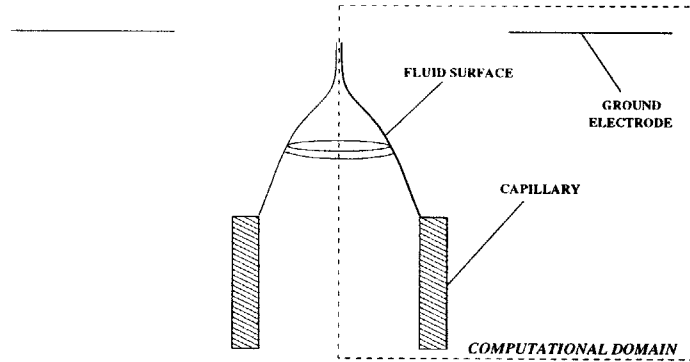


Figure 7-1: Computational domain (assuming cylindrical symmetry)

precludes one from predicting and performing the analysis of asymmetric multi-cone configurations.

### 7.3 External electrostatics model

A standard boundary element scheme is used to determine the charge density on the boundary surfaces of the electrodes and the fluid interface. The computational domain includes a thin capillary which delivers the fluid to the tip, a ground electrode, and the fluid meniscus as shown in Fig. 7-1. The boundary is subdivided into a number of panels each with a prescribed value of the electric potential. Each panel is also assigned an unknown value of the charge density which is subsequently determined as part of the solution. Due to the cylindrical symmetry of the problem, all of the panels are shaped as horizontal strips in the plane perpendicular to the axis of symmetry. Contributions to the potential from each panel are evaluated along all of the remaining strips and assembled into a linear matrix equation which is then solved for the unknown charge densities. The benefit of this approach is that it eliminates the need for any computations to be performed in the region between the capillary and the electrode and, as a result, offers great savings in computational time in comparison to the alternative finite element or finite difference schemes. In addition, this method is readily adaptable to varying geometries, while other methods would require re-generation of two-dimensional grids at every step of the iteration.

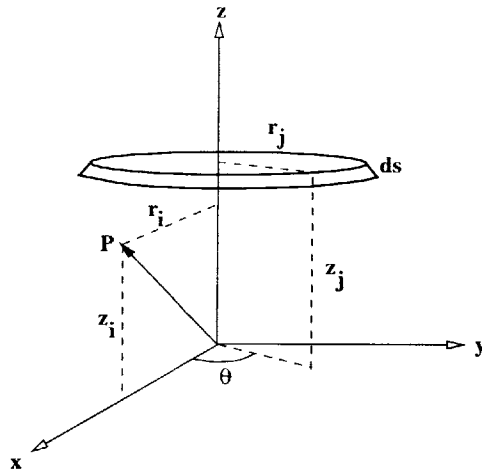


Figure 7-2: Coordinate definition

The coordinate system used in the formulation of the problem is shown in Fig. 7-2. The contribution to the potential at point  $(x_i, y_i, z_i)$  due to an element with charge  $dq$  located at point  $(x_j, y_j, z_j)$  is given by:

$$d\phi_{i,j} = \frac{dq}{4\pi\epsilon_0\sqrt{(x_i - x_j)^2 + (y_i - y_j)^2 + (z_i - z_j)^2}} \quad (7.1)$$

Since the electric potential will be constant along each of the panels due to the axial symmetry, the azimuthal coordinate of the reference point  $(x_i, y_i)$  is arbitrary. Assuming the strips to have radii  $r_i$  and  $r_j$  respectively, the charge  $dq$  can be expressed in terms of the local charge density  $\sigma_j$  and the arclength  $ds_j$  as  $\sigma_j ds_j r_j d\theta$ . Assuming the reference to be on the x-axis, the expression for the electric potential due to each panel becomes:

$$d\phi_{i,j} = \frac{\sigma_j ds_j r_j d\theta}{4\pi\epsilon_0\sqrt{(r_i - r_j \cos \theta)^2 + (r_j \sin \theta)^2 + (z_i - z_j)^2}} \quad (7.2)$$

Combining all of the constant terms and using the following definitions:

$$a = r_i^2 + r_j^2 + (z_i - z_j)^2 \quad (7.3)$$

$$b = 2r_i r_j \quad (7.4)$$

$$m = \frac{2b}{a + b} \quad (7.5)$$

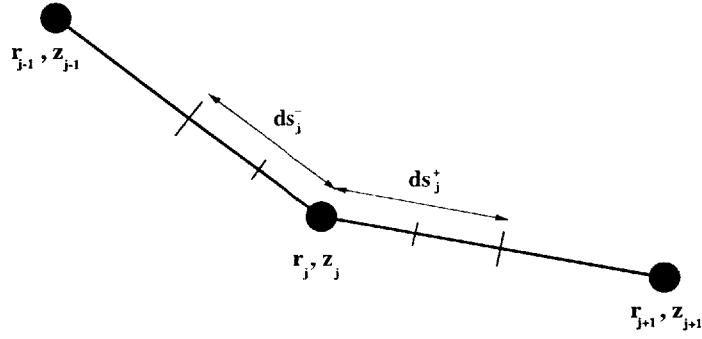


Figure 7-3: Computational grid

Eqn. 7.2 can be integrated around each panel producing the following expression for the potential  $\phi_{i,j}$ :

$$\phi_{i,j} = \frac{\sigma_j ds_j r_j}{4\pi\epsilon_0} \frac{2}{\sqrt{a}} \int_0^\pi \frac{d\theta}{\sqrt{1 - \frac{b}{a} \cos \theta}} \quad (7.6)$$

Rewriting Eqn. 7.6 in terms of the elliptic function of the first kind  $K(m)$ , the final expression for  $\phi_{i,j}$  becomes:

$$\phi_{i,j} = \frac{\sigma_j ds_j r_j}{4\pi\epsilon_0} \frac{4}{\sqrt{a+b}} K(m) \quad (7.7)$$

Summing up all of the contributions to the potential from the  $n$  elements at the location of the  $i$ th panel yields an  $n \times n$  system which can then be inverted and solved for  $\sigma$ :

$$\phi_i = C_{ij} \sigma_j \quad (7.8)$$

where

$$C_{ij} = \frac{ds_j r_j}{4\pi\epsilon_0} \frac{4}{\sqrt{a+b}} K(m) \quad i \neq j \quad (7.9)$$

Due to the non-uniformity of the grid, each panel segment is centered about its nominal position  $(r_j, z_j)$  and then split into two pieces as shown in Fig. 7-3: a right-handed and a left-handed arc whose lengths are respectively given by:

$$ds_j^- = \sqrt{\left(\frac{r_j - r_{j-1}}{2}\right)^2 + \left(\frac{z_j - z_{j-1}}{2}\right)^2} \quad (7.10)$$

$$ds_j^+ = \sqrt{\left(\frac{r_{j+1} - r_j}{2}\right)^2 + \left(\frac{z_{j+1} - z_j}{2}\right)^2} \quad (7.11)$$

The corresponding values of parameters  $a$  and  $b$  are evaluated at the center of each segment:

$$a^- = r_i^2 + (r_j^-)^2 + (z_j^- - z_i)^2 \quad (7.12)$$

$$a^+ = r_i^2 + (r_j^+)^2 + (z_j^+ - z_i)^2 \quad (7.13)$$

$$b^- = 2r_i r_j^- \quad (7.14)$$

$$b^+ = 2r_i r_j^+ \quad (7.15)$$

where the center coordinates of the left-hand and the right-hand segments respectively are given by:

$$P^- : \left( r_j - \frac{r_j - r_{j-1}}{4}, z_j - \frac{z_j - z_{j-1}}{4} \right) \quad (7.16)$$

$$P^+ : \left( r_j + \frac{r_{j+1} - r_j}{4}, z_j + \frac{z_{j+1} - z_j}{4} \right) \quad (7.17)$$

In terms of these quantities, the off-diagonal influence coefficients  $C_{ij}$  can be expressed as:

$$C_{ij} = \frac{1}{\pi \epsilon_0} \left( \frac{ds_j^- r_j^-}{\sqrt{a^- + b^-}} K(m^-) + \frac{ds_j^+ r_j^+}{\sqrt{a^+ + b^+}} K(m^+) \right) \quad i \neq j \quad (7.18)$$

Due to the lack of precision, the diagonal coefficients  $C_{ii}$  may not be evaluated using Eqn. 7.18 since both  $m^+$  and  $m^-$  approach unity as the grid size is reduced. As  $K(m)$  diverges when its argument approaches unity, the diagonal elements need special consideration. Although asymptotic expressions for  $K(m)$  do exist in the limit in which  $m \rightarrow 1$ , the limiting behavior fails near the tip when  $r_i^2 + r_j^2$  becomes of the same order as  $(z_i - z_j)^2$  and, hence, the limiting condition for  $2b/(a + b)$  to approach unity is no longer satisfied.

Numerical evaluation of the self-contribution coefficients eliminates this difficulty. Splitting the panel into two segments as before, the contribution due to each segment at the point  $(r_i, z_i)$  can be evaluated by integrating the expression in Eqn. 7.9

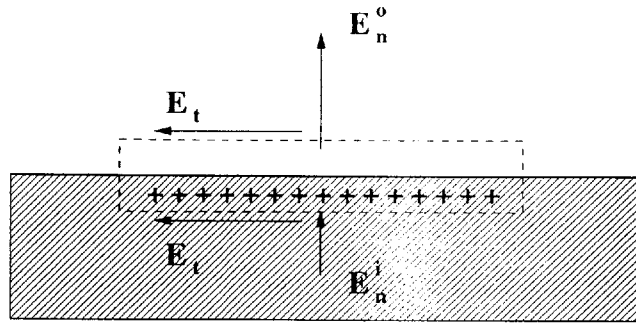


Figure 7-4: Surface field configuration

assuming locally linear interpolations for both  $r(s')$  and  $z(s')$ :

$$C_{ii} = \int_{s-ds^-}^s \frac{ds' r(s')}{4\pi\epsilon_0} \frac{4}{\sqrt{a(s') + b(s')}} K(m(s')) + \int_s^{s+ds^+} \frac{ds' r(s')}{4\pi\epsilon_0} \frac{4}{\sqrt{a(s') + b(s')}} K(m(s')) \quad (7.19)$$

At each step of the iteration, after the geometry of the boundary surfaces had been updated, the influence coefficients are re-evaluated and the new surface charge densities are obtained.

## 7.4 Electrohydrodynamics at the fluid interface

### 7.4.1 Surface electrostatics

This section presents the analysis and discussion of the relevant equations for the components of the electric field, the stress tensor at the fluid interface, as well as the equations governing both the conductive and convective charge transport. Figure 7-4 shows the generic configuration of the electric fields at the surface and the corresponding notation utilized for the remainder of this chapter. Due to the finite electrical conductivity of the fluid, the tangential component of the electric field will, in general, be non-zero creating a voltage drop downstream of the capillary. This voltage drop, once computed, can be incorporated into Eqn. 7.8 to iteratively yield a self-consistent electrostatic solution. Since the internal fields within the conical meniscus are generally smaller in magnitude than the normal external fields, the electric potential should not vary significantly over the cross-section of the meniscus. The tangential field, therefore, can be approximated as being uniform across any plane perpendicular to the axis of symmetry. It should be noted that since the accounting

of the total current is performed at the tip of the jet, where convective current is the dominant contributor, any such approximation in the computation throughout the bulk of the fluid would have little effect on the estimate of the convective current near the tip. Moreover, since the magnitude of the tangential electric field is generally small within the bulk of the fluid, adapting such an approximation should not dramatically impact the stress balance.

Using a pill-box shown in Fig. 7-4 and applying Gauss's law across the fluid boundary results in the following expression relating the internal and the external fields to the local charge density:

$$\sigma = \epsilon_0(E_n^o - \epsilon E_n^i) \quad (7.20)$$

Taking the downstream direction to be positive, the gradient of the electric potential along the boundary can be related to the tangential electric field:

$$\frac{dV}{ds} = -E_t \quad (7.21)$$

An additional relationship can be found between the internal normal field  $E_n^i$  and the tangential field  $E_t$  by applying current conservation for a cylindrically symmetric section positioned internally with respect to the meniscus surface as shown in Fig. 7-5. The expressions for the convective and the conductive components of the current are given by:

$$I_{cond} = K\pi r^2 E_t \quad (7.22)$$

$$I_{conv} = 2\pi r v \sigma \quad (7.23)$$

where  $v$  is the fluid velocity at the surface and  $K$  is the electrical conductivity. Since the sum of the two currents must remain constant along the surface of the meniscus, so that:

$$\frac{d}{ds}[I_{cond} + I_{conv}] = 0 \quad (7.24)$$

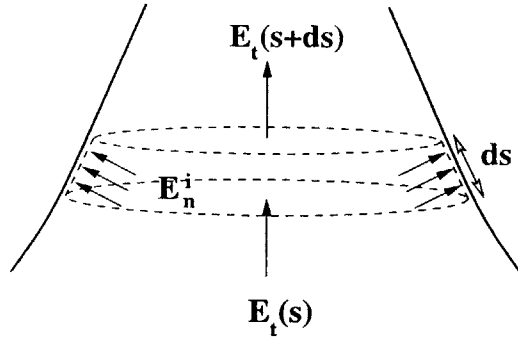


Figure 7-5: Internal field configuration

or, substituting Eqns. 7.22-7.23 into Eqn. 7.24:

$$r \frac{dE_t}{ds} + 2E_t \frac{dr}{ds} + \frac{2}{rK} \frac{d}{ds} [rv\sigma] = 0 \quad (7.25)$$

Using Ohm's law at the outer surface of the fluid element to relate the internal normal field  $E_n^i$  to the rate at which the charge arrives at the fluid surface yields:

$$E_n^i = \frac{1}{rK} \frac{d}{ds} [rv\sigma] \quad (7.26)$$

Equations 7.20, 7.21, 7.22-7.24, and 7.26 together with the solution for the charge density obtained by inverting the matrix equation 7.8 form a complete set of relations necessary to solve for the fields and the currents given a prescribed profile of the fluid meniscus  $r(z)$ . The fluid profile is obtained independently by imposing the stress balance at the surface. It should be noted that the value of the total current is initially indeterminate and must come out as part of the solution.

Both the normal and the tangential components of the electric field interact with the charge collected at the surface and produce electrostatic traction which must be in balance with the surface tension and the pressure differential. In order to obtain an expression for the stress tensor, it is first necessary to determine the relationship between the external and internal tangential fields. Since  $\nabla \times E$  must equal zero in a static situation, the line integral of the electric field around any closed path must vanish. Considering a closed path, such as the one shown in Fig. 7-4, it is readily seen that the tangential electric field  $E_t$  must remain constant across the interface. The

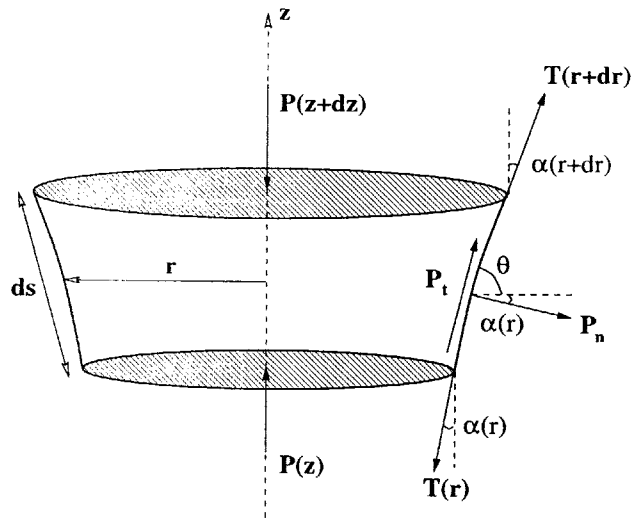


Figure 7-6: Force diagram

surface stress components can now be obtained from the divergence of the Maxwell stress tensor given by:

$$f_j = \frac{\partial}{\partial x_k} [E_j D_k] - \frac{1}{2} \frac{\partial}{\partial x_j} [E \cdot D] \quad (7.27)$$

Using the divergence theorem to rewrite Eqn. 7.27 in the integral form and evaluating the tensor on the two faces of the surface element in Fig. 7-4 yields the following expressions for the normal and the shear stress components:

$$P_{nn}^o - P_{nn}^i \equiv P_n = \frac{1}{2} \epsilon_0 [E_n^{o2} - \epsilon E_n^{i2} - (1 - \epsilon) E_t^2] \quad (7.28)$$

$$P_{nt}^o - P_{nt}^i \equiv P_t = \epsilon_0 E_t [E_n^o - \epsilon E_n^i] \quad (7.29)$$

The coupling of the fluid equations together with the electrostatic stresses at the surface is addressed in the following section.

## 7.4.2 Stress and momentum balance

Each section of the fluid meniscus is subject to the electrostatic normal and tangential stresses, pressure differential, and surface tension all of which must be in balance and must satisfy equilibrium in the steady state. A diagram showing all of the forces acting on a fluid section of radius  $r$  and height  $dz$  is shown in Fig. 7-6. The positive  $z$ -axis is pointing in the direction of the tip, even though in order to maintain a consistent sign convention the normally negative slope of the generatrix has been

chosen to be positive in that direction. The force balance will be considered in the axial direction first. Then, a local pressure equilibrium will be enforced for each surface element along the circumference of the section. The surface tension force  $T$  acts along the perimeter of the volume element in the direction which is locally tangent to the surface. The net contribution of the surface tension to the overall balance can be evaluated as the differential of the axial projections of the surface tension components across the section boundaries:

$$dT = \frac{d}{dr} (2\pi\gamma r \cos \alpha) dr \quad (7.30)$$

Since  $\cos \alpha$  can be written in terms of the slope  $r' = dr/dz$ :

$$\cos \alpha = \frac{1}{\sqrt{1 + r'^2}} \quad (7.31)$$

the differential on the right hand side of Eqn. 7.30 can be expanded into:

$$dT = 2\pi\gamma r \left( \frac{1}{r\sqrt{1 + r'^2}} - \frac{r''}{(1 + r'^2)^{3/2}} \right) dr \quad (7.32)$$

Note that the surface tension contains contributions from the two principal radii of curvature, as expected. The first term in parentheses is the radial curvature due to the cylindrical symmetry while the second term is the profile curvature of the generatrix. Projecting now the remaining pressure components in the axial direction, the momentum balance for the cylindrical section yields:

$$\frac{dT}{dr} - 2\pi r P_n + 2\pi r \frac{dz}{dr} P_t - \frac{d}{dz} (\pi r^2 p) \frac{dz}{dr} = \left( \rho \pi r^2 \frac{dz}{dr} \right) v \frac{dv}{dz} \quad (7.33)$$

Applying momentum conservation to the control volume in Fig. 7-6 yields:

$$\frac{2}{r} P_t - \frac{1}{\rho} \frac{dp}{dz} = v \frac{dv}{dz} \quad (7.34)$$

where the first term represents the contribution of the electrostatic shear stress distributed over the cross-sectional area of the control volume. Simplifying Eqn. 7.33

by differentiating the pressure term with respect to  $z$  it is apparent that the momentum equation in Eqn. 7.34 is contained within the axial stress balance in Eqn. 7.33. Subtracting Eqn. 7.34 from Eqn. 7.33 yields a relation which can be easily identified as a normal stress balance for a surface element:

$$\gamma \left( \frac{1}{r\sqrt{1+r'^2}} - \frac{r''}{(1+r'^2)^{3/2}} \right) - P_n - p = 0 \quad (7.35)$$

Finally, the flow must obey continuity. As discussed earlier, due to the low Reynolds numbers, the shear stress applied at the surface diffuses through to the internal layers of the fluid resulting in a fairly flat velocity profile. Assuming the profile to be uniform across any cross section of the meniscus, one gets:

$$Q = \pi r^2 v \quad (7.36)$$

Knowing the electrostatic stress components from Sec. 7.4.1, Eqns. 7.35-7.36 can be solved simultaneously to yield the surface profile  $r(z)$  and the pressure variation along the meniscus.

## 7.5 Results of the numerical model

### 7.5.1 Summary of the model

In order to avoid zero-slope singularities corresponding to the purely vertical or purely horizontal slopes, all of the relevant derivatives were expressed in terms of  $s$ , the distance along the fluid interface, and the polar angle  $\theta$  such that  $dz/dr = \tan \theta$ . A summary of the resulting equations used in the numerical procedure is provided below:

- Normal stress balance

$$\frac{d\theta}{ds} = \frac{\sin \theta}{r} - \frac{(P_n + p)}{\gamma} \quad (7.37)$$

- Axial momentum balance

$$\frac{dp}{ds} = \frac{2}{r} \left( P_t \sin \theta + \frac{\rho Q}{\pi^2 r^4} \cos \theta \right) \quad (7.38)$$

- Electric fields

$$E_n^o = \frac{\sigma}{\epsilon_0} + \epsilon E_n^i \quad (7.39)$$

$$E_n^i = -\frac{Q}{\pi r K} \frac{d}{ds} \left( \frac{\sigma}{r} \right) \quad (7.40)$$

$$E_t = \frac{1}{K \pi r^2} \left( I_o - \frac{2Q\sigma}{r} \right) \quad (7.41)$$

- Electrostatic stresses

$$P_n = \frac{1}{2} \epsilon_0 [E_n^{o2} - \epsilon E_n^{i2} - (1 - \epsilon) E_t^2] \quad (7.42)$$

$$P_t = \epsilon_0 E_t [E_n^o - \epsilon E_n^i] \quad (7.43)$$

- Surface element geometry

$$\frac{dr}{ds} = \cos \theta \quad (7.44)$$

$$\frac{dz}{ds} = \sin \theta \quad (7.45)$$

- Electrostatics equations

$$\frac{dV}{ds} = -E_t \quad (7.46)$$

$$V = \tilde{C} \sigma \quad (7.47)$$

Overall, there are  $11N + 1$  unknowns and a total of 11 algebraic vector equations and differential equations with the appropriate boundary conditions, where  $N$  is the number of elements along the fluid interface. A similar analytical model by A. Ganan Calvo [55] indicates that the total current is an “eigenvalue” of the problem and can be analytically extracted by asymptotic matching. However, no numerical analog was found, as of yet, as to the procedure for determining the overall current as part of the

solution.

## 7.5.2 Preliminary numerical results

A one-dimensional logarithmic grid  $s_i$  along the fluid interface was used for discretization. The minimum grid size at the tip was chosen so as to be smaller than the radius of the meniscus at that location ( $ds_{tip} < r_{tip}$ ). After the completion of each cycle, a new surface profile  $r(z)$  was determined from the stress balance and matched to satisfy the terminal conditions on  $r$  and  $z$  at the capillary. This was done by stretching the grid  $s_i$  as well as the profile coordinates,  $r_i$  and  $z_i$ , by a constant multiple  $\beta$  until the terminal condition on the radius was met. Since none of the relations (except for the slowly-updating electrostatics) depend explicitly on  $z$ , each iterate can be shifted appropriately along the  $z$ -axis to automatically match the terminal condition on  $z$  at the capillary. The uniform stretching of the grid by a constant factor  $\beta$  ensures that the geometrical constraints  $dz/ds = \sin \theta$  and  $dr/ds = \cos \theta$  are satisfied both before and after the “stretching”, i.e.  $d(\beta z)/d(\beta s) = \sin \theta$ ,  $d(\beta r)/d(\beta s) = \cos \theta$ .

In spite of the difficulty in determining the overall current, preliminary test runs for a prescribed value of  $I_o$  have been obtained. Shown in Fig. 7-7 is a sample iterate for a  $20 \mu m$  capillary supplied with a formamide solution ( $K = 1 Si/m$ ) at the flow rate of  $10^{-13} m^3/s$  and an applied voltage of 3,000 V. The total current was chosen to be at twice the value predicted by the empirical relation in Eqn. 5.36 for identical operating conditions. Although it is believed that a stable solution can only exist for a single value of the total current, increasing or decreasing the prescribed value of the current by as much as factors of two or three made no significant difference in the solution. Fig. 7-7 indicates that the tangential electric field is negligible within the cone so that the fluid surface is mostly equipotential, as predicted by the Taylor’s model. In addition, pressure variations are found to be very small within the fluid meniscus for  $r \gg r^*$ , once again confirming Taylor’s assumption that the balance in this region is achieved primarily by the two dominant stress components - the surface tension and the electrostatic traction. Although signs of necking are clearly visible at the tip of the meniscus, due to the lack of convergence in its vicinity, no conclusive

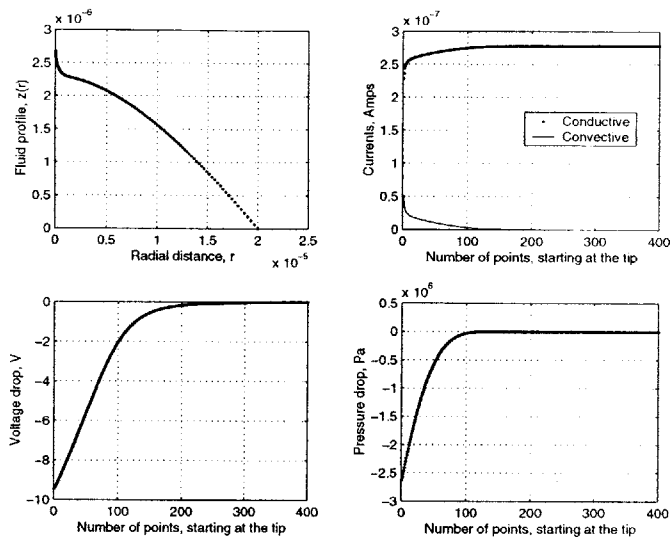


Figure 7-7: Sample solution

statements can be made as to the steady-state diameter of the jet.

In the conical region, for which  $r \gg r^*$ , any stress imbalance that exists between the cylindrical component of the surface tension and the normal electrostatic stress is compensated by the properly chosen generator curvature (see Eqn. 7.37). Divergence near the tip occurs due to the lack of balance between the three stress components all of which are intensified as  $r \rightarrow 0$ . As a result of the significant deviations from equilibrium, large profile curvatures are required to compensate for the mismatch, creating a “swirling” surface profile. Although alternative iteration schemes which avoid solving for the generator curvatures in the jet region may eliminate the instability, it is believed that this divergence is not accidental but is a consequence of the improper choice of the total current. Additional studies are needed to better understand the nature of these solutions before any strides are made to obtain a numerically stable iteration.

## 7.6 Conclusions

In spite of the divergence near the tip, formulation and development of this electrohydrodynamic model is an important first step in identifying and understanding the mechanisms which govern the operation of electrospray emitters. Although the development of similar models has been attempted in the past, the physical and

numerical formulations developed in this Chapter are some of the most complete. The novelties implemented as part of this model are outlined below.

- The ability to simultaneously resolve features with relative geometrical proportions of 10,000:1
- Formulation in the intrinsic surface coordinates  $(s, \theta)$  was used to avoid singularities associated with infinite slopes
- The model is flexible: arbitrary electrode geometries, fluid properties, and operating conditions can be prescribed
- The model utilizes very few simplifying assumptions in the formulation and implementation (i.e. includes effects of internal pressure, inertia, finite conductivity, finite flow rate, geometry, etc)

Preliminary results are in good qualitative agreement with existing theories, however, additional theoretical work is required before any further progress can be made (see Chapter 8 for Recommendations).

# Chapter 8

## Conclusions and Recommendations for Future Work

Some of the more important contributions of this work to the field of spacecraft propulsion are briefly summarized in this Chapter. Notable progress has been made in identifying the advantages and the limitations of the existing propulsion technologies through modeling and, where appropriate, fabrication and testing. This work, however, is by no means exhaustive in the search for a “perfect” high-performance miniature propulsion device. More importantly, as a result of the effort to develop a working miniature prototype, a number of critical issues have been identified and an extensive knowledge base has been acquired for any future work in this field. Based on the author’s own experience, some of the recommendations, suggestions, and general directions for future improvements are presented in the following sections.

### 8.1 Contributions to the scaling methodology

Scaling of the existing high-power devices to attain operation at low power is not a novel approach; it has been studied and experimentally attempted by many researchers in the past. In most cases, however, scaling was implemented as either a photographic reduction in the thruster dimension, or as a set of ad hoc variations in the length scale, power level, B-field, and the flow rate to achieve optimal operation.

Little consideration was given to the physical phenomena which actually control the overall efficiency, specific impulse, and the lifetime of a particular device. The present work is unique in that it identifies and develops, from first principles, a collection of generic scaling strategies, designed specifically to preserve certain non-dimensional quantities which ultimately characterize the performance of the individual thrusters. Specifically, this work has demonstrated that gas-phase ionization devices, such as Hall and ion thrusters, both require an increase in the particle density at small scale in order to preserve high efficiency. It was shown that increasing particle densities helps maintain the relative proportions of the mean free path to the length scale of the device (see Chapter 2.2.2) and, therefore, preserves the utilization efficiency under scaling. In all cases, however, deviations from this scaling strategy were shown to have resulted in a decrease of the overall thruster efficiency, as supported by the experimental data gathered from a number of existing commercial and laboratory thrusters (see Sec. 4.5).

Another important aspect of the higher plasma density is the increased heat flux into the wall. Although the heat fluxes were shown to increase with decreasing size, it was found that, the temperature differentials must remain constant as long as heat conduction is the dominant heat transfer mode. It was, therefore, important to maintain the aspect ratios of critical thruster components so as to avoid overheating them at small scale. A clear example of a case where the aspect ratio was not preserved is in the design of a center pole piece for the 50 W Hall thruster. Although its diameter was chosen strictly according to scaling, its length ended up being twice as long as needed to maintain an adequate temperature differential. Permanent magnets, on the other hand, were designed to have a disproportionately large base and, in spite of the larger thickness, were able to reject heat and maintain relatively low temperatures.

The inability to use electric coils at small scale to produce the required magnetic fields was shown to be an important aspect in the design of small-scale electron bombardment devices. Although the use of permanent magnets has extended the available scaling range to power levels beyond what is normally possible with electric coils, they introduced a number operational difficulties. One of the most troublesome

was the inability to adjust or “turn off” the magnetic field. As a result, both the channel walls and the center pole piece collected metallic dust and magnetic particles during handling and installation, causing excessive arcing and, at times, damage to the anode.

The issue of the operational lifetime is generally of little concern for most high-power devices, as they usually operate at lower plasma densities and suffer only moderate erosion rates over the course of their operating life. For this reason, lifetime has generally been overlooked by many of the researchers as a secondary issue. As it was demonstrated in Sec. 2.2.2, however, a combination of smaller thruster dimensions with a proportional increase in the particle fluxes at small scale, both result in a dramatic increase of the erosion rates and a significant reduction of operating life. The consequences of the increased erosion rates were clearly seen by examining the erosion pattern at the tip of the center pole and at the outer edges of the anode in a 50 W Hall thruster after about 8-10 hours of accumulated operational time (see Sec. 4.6). Identification and experimental justification of the intrinsic lifetime limitations of gas-phase ionization devices at small scale are thought to be two of the most important contributions of this work.

Alternative scaling strategies were considered in the hope of alleviating lifetime limitations at small scale. Studies have shown that viable solutions do exist for improving lifetime by relaxing the constraint on the particle density and accepting a partial loss in the operating efficiency. Most importantly, however, it was shown that it is intrinsically impossible to build a small-scale, low-power device with electron bombardment ionization which is both efficient and durable at the same time.

Finally, this work features the development and testing of the smallest Hall thruster ever built. It is in the process of its design and fabrication that many of the previously unknown, yet critical issues were identified and lessons were learned. Scaling rules, general design strategies, and guidelines developed here, are some of the most important contributions of this work to the field of micropropulsion. It is hoped that this work will not only stimulate interest, but will also provide a strong foundation for any related work in this area.

## 8.2 Recommendations pertinent to scaling of Hall thrusters

### 8.2.1 Theoretical work

1. The analysis of alternative scaling strategies developed for the Hall thrusters in Sec. 4.5 opens up new avenues for exploration of the possible designs with reduced efficiencies and improved life. Since currently existing low-power devices, such as PPTs, demonstrate efficiencies of only 7-10 %, while more efficient colloidal thrusters are still in their early stages of development and are unlikely to be available for a number of years, low-efficiency Hall thrusters ( $\eta \sim 20 - 25\%$ ) may become an attractive alternative to PPTs in the near future. It may, therefore, be useful to perform a comparison study of these low-efficiency Hall thrusters against other competing technologies and evaluate, from a systems standpoint, the envelopes of mission objectives (velocity increments, available power, mission duration and operating life) which could benefit from the use of these devices.
2. Departures from strict scaling of the plasma density and its effects on the operating efficiency of Hall thrusters were analyzed in detail in Sec. 4.5. Departures in the scaling of a magnetic confinement scheme, however, were never considered. Significant losses in the magnetic field strength have a well-known effect of increasing the leakage of electrons and reducing the utilization efficiency. At the other extreme, a disproportional increase in the magnetic field strength has shown to have a similar effect on the efficiency due to the inability of the electrons to penetrate the magnetic barrier and fully ionize the propellant. Quantifying and generalizing these effects for families of existing thrusters is important in an attempt to develop a complete sensitivity map of the performance on various scaling parameters and departures from strict scaling, similar to what was done in Sec. 4.5.

3. Scaling laws for the Hall thrusters, as presented in Sec. 2.2 and Sec. 4.5, were developed under the assumption of continuous thruster operation. It is conceivable, however, that in order to reduce mean operating power levels, a larger thruster could be operated in a pulsed mode with a prescribed duty cycle, delivering mean thrust levels which are lower than the instantaneous nominal thrust. The instantaneous required power levels would be too high for a miniaturized spacecraft, however, with an appropriate use of energy storage elements, the thruster could be successfully operated in this regime. In fact, such operation was achieved with a 200 W Hall thruster developed by Busek Co., MA. Further studies, however, are needed to analyze the impact of pulsed operation on thruster's efficiency and operating life.

### 8.2.2 Experimental work

1. Most of the miniature plasma devices may require a small-size cathode which could be operated at low power. Although low-power cathodes which supply adequate emission current per unit area do exist and are currently being used in most electron microscopy devices, no cathode technology exists at this time suitable for miniature propulsion. Development of low-power cathodes is an important step for any future work in this area.

2. Development of adequate diagnostic equipment at small scale is important in testing and troubleshooting new miniature devices. Specifically, small magnetic probes capable of resolving and mapping the profile of the magnetic field strength over a length scale of 1 mm or smaller would have been extremely useful in identifying the causes for the inefficiency of the 50 W Hall thruster.

Because of the intrinsically larger heat fluxes at small scale, adequate thermal design of sensitive thruster components becomes very important. Development of miniature temperature probes, which could be installed to monitor critical elements during operation, would be important for testing and validation of prototype designs.

### 8.3 Contributions to the modeling of colloidal thrusters

The physics of colloidal thrusters has been studied for decades, yet many of the phenomena that govern their operation are still either poorly understood or completely unknown. Numerous attempts have been made in the past to model the operation of colloidal thrusters, however, most of these models failed to include all of the critical elements necessary to predict the performance of a colloidal thrusters subject to an arbitrary set of operating conditions.

This work, on the other hand, presents one of the most complete formulations of the physics of colloidal thrusters, including the effects of non-zero flow rate and non-zero electrical conductivity as well as the effects of internal pressure, fluid inertia, electrostatic forces, and arbitrary electrode geometry (Sec. 7.2). One of the more important novelties of this model is its ability to capture and resolve not only the base of the conical meniscus, but also the very tiny jet with a scale ratio of up to 10,000:1 in geometrical dimensions (Sec. 7.5.2). Another novelty developed in the present work is the use of intrinsic coordinates along the fluid interface to avoid numerical singularities that other models experience in the cases of purely vertical or purely horizontal profiles (Sec. 7.4.2). Most importantly, however, this model is extremely flexible in that it can be used to predict the performance of colloidal thrusters with arbitrary geometries and for a variety of operating conditions.

A separate semi-analytical flow model was developed to predict the effects of viscosity on the flow pattern in the interior region of the conical meniscus (Chapter 6). It was concluded, based on the results of the model, that the viscous shear flow is insignificant in the vicinity of the tip regardless of fluids viscosity and for most operating conditions of interest (see Sec. 6.3). This result is important as it validates one of the critical assumptions, made in the formulation of the more detailed electrohydrodynamic model, that the fluid flow at the surface of the meniscus can be well approximated as a one-dimensional inviscid flow.

## 8.4 Recommendations pertinent to the modeling of colloidal thrusters

1. The model developed in Chapter 7 to simulate the behavior of cone-jet emitters is adequate only in the conical region where the internal pressure, surface tension, and electrostatic stresses are all small in magnitude. Any imbalance of the stress components in this region is compensated by the profile curvature, creating a well-known bullet-like meniscus. In the vicinity of the jet, however, all three of the stress components become proportionately larger. As a result, intermediate iterates require large profile curvatures to compensate for the stress imbalance causing the shape of the meniscus to twist and subsequent iterations to diverge. Alternative schemes are required to obtain convergent solutions in this region.
2. A number of existing analytical models indicate that a stable solution can only be obtained for a single value of the total current extracted as part of the computation. As there is currently no available method for determining this current numerically, additional analytical work is required to understand the nature of the solution in order to develop a suitable procedure or a criterion to consistently solve for the value of the total current at each iteration.
3. As it was indicated in Chapter 5, the mixed regime, when both ions and droplets are emitted, may be a more desirable mode of operation as it improves the mean specific impulse of the device. It is, therefore, important to include the mechanism of ion emission as part of the numerical model. The large currents usually associated with the emission of ions may have an impact on the conductive and the convective components of the total current within the cone, thus modifying some of the electrostatic and geometrical properties of the fluid meniscus currently obtained in the absence of ions. Implementation of this mechanism and its integration with the currently existing model amounts to setting a threshold on the external electric field near the tip corresponding to  $E_n^o \approx E_{cr}$ . When the

threshold is exceeded, the ion current density can be locally modeled by Eqn. 5.62. The current conservation equation (Eqn. 7.24) will have to be modified accordingly to account for the loss of ions at the surface.

# Appendix A

## Additional Considerations in the Scaling of Hall Thrusters

This section contains additional details on the scaling model of Hall thrusters, supplementing a brief summary presented in Chapter 2.

All of the basic plasma phenomena in Hall thrusters rely heavily on the ionization process that takes place within the acceleration chamber whereby the neutrals are ionized in collisions with the electrons. As the size of the device is reduced, all else remaining unchanged, the number of collisions that the electrons and the neutrals experience with each other as they traverse the effective length of the device is reduced. Thus, in order to maintain the collisionality properties of the plasma, it is necessary to increase the number density of each species in proportion. This is equivalent to the statement that the ratio of the mean free paths of each of the species to the characteristic length of the device has to be preserved under scaling

$$\frac{\lambda}{L} = \frac{1}{nQL} = \text{const.} \quad (\text{A.1})$$

where  $n$  is the particle number density and  $Q$  is the collision cross-section. Here we have assumed that the collision cross-section, being a function of the electron temperature alone, remains invariant. Thus, particle densities (both  $n_e$  and  $n_n$ ) are

inversely proportional to the characteristic thruster dimension:

$$n_e, n_n \sim \frac{1}{L} \quad (\text{A.2})$$

Invariance of  $T_e$  also yields a similar result for the pressure  $p$ :

$$p \sim \frac{1}{L} \quad (\text{A.3})$$

Knowing the particle densities, it is now possible to determine how the mass flow rate of the propellant scales with size:

$$\dot{m} = m_i n c A \quad (\text{A.4})$$

where  $c$  is the ion exhaust velocity and  $A$  is the cross-sectional area of the channel opening. Since the number density scales inversely with size and the area scales as the square of the size, the mass flow rate must be linear in the characteristic thruster dimension:

$$\dot{m} \sim L \quad (\text{A.5})$$

We shall now turn to the discussion of the electrical properties of the plasma. The total current in the channel can be deduced from a one-dimensional generalized Ohm's law:

$$j = \sigma \left( E + \frac{1}{en} \frac{dP_e}{dx} \right) \quad (\text{A.6})$$

where  $\sigma$  is the electrical conductivity given by:

$$\sigma = \frac{n_e e^2}{m_e \nu} \quad (\text{A.7})$$

and  $\nu$  is the collision frequency, proportional to the neutral number density. Since both number densities scale the same way,  $\sigma$  remains invariant, and therefore:

$$j \sim E \sim \frac{V}{L} \sim \frac{1}{L} \quad (\text{A.8})$$

As an additional mechanism, based on Bohm diffusion across the magnetic field,

$$\sigma = \frac{en_e}{16B} \quad (\text{A.9})$$

which is also invariant, provided both  $n_e$  and  $B$  both scale as  $1/L$  (see below). The electron current, then, is the product of the current density and the plasma column area ( $\sim L^2$ ), hence:

$$I_e \sim L \quad (\text{A.10})$$

The ion current density, on the other hand, is governed by the distribution of ionization rates ( $\nabla \cdot \mathbf{j}_i = e\dot{n}_e$ ), and since the ionization mean free path remains the same fraction of length,  $\dot{n}_e$  will be distributed the same way, and its magnitude will scale as  $n_e v_i / L \sim 1/L^2$ , giving

$$j_i \sim 1/L \quad (\text{A.11})$$

$$I_i \sim L \quad (\text{A.12})$$

The previous result suggests that the utilization efficiency, given by:

$$\eta_u = \frac{m_i I_i}{em} \quad (\text{A.13})$$

scales as the ratio of the ion current to the mass flow rate, and thus remains invariant, as desired. The total power required for the thruster scales as the product of the applied voltage times the ion current:

$$P = VI \sim L \quad (\text{A.14})$$

This relationship forms the basis for scaling, as it is the desired power level in the miniaturized thruster that ultimately determines its characteristic dimension.

We can now examine the losses and evaluate the thruster efficiency. The loss of ions to the wall can be estimated as the ion current into the wall times the ionization potential:

$$P_{wall} \sim v_{Bohm} n_e A V_i \sim L \quad (\text{A.15})$$

where  $v_{Bohm} = \sqrt{kT_e/m_i}$ . Therefore, the overall efficiency, which depends mainly on the wall recombination losses ( $P_{wall}/P$ ), ionization-radiation losses, and neutral losses ( $\eta_u$ ), will remain invariant, as desired.

In order to preserve the electron confinement characteristics by the magnetic field, it is necessary to maintain the ratio of the Larmor radius relative to the chamber dimension constant:

$$\frac{r_L}{L} = \frac{mv}{eBL} = const. \quad (\text{A.16})$$

Hence,

$$B \sim \frac{1}{L} \quad (\text{A.17})$$

Although most of the parameters considered above scale with the thruster dimension as desired, the sheath thickness (Debye length) which goes as  $\sqrt{T_e/n_e}$ , scales as  $\sqrt{L}$  hence violating the general trend. As a result, sheaths will become proportionally bigger as the characteristic dimension is reduced. It is believed, however, that this does not have a strong impact on the general scale invariance as long as the sheaths remain much thinner than the channel width.

Finally, an electron energy equation can be used as a check on the assumption of the electron temperature invariance under scaling. Neglecting for the moment radiation and elastic losses, the electron energy equation reads:

$$\nabla \cdot \left( -\frac{\mathbf{j}_e}{e} h_e - K_e \nabla T_e \right) = \mathbf{E} \cdot \mathbf{j}_e \quad (\text{A.18})$$

where  $h_e$  is the electron enthalpy (including ionization), and is invariant if  $T_e$  is constant, and  $K_e$  is the electron thermal conductivity. The general Wiedemann-Franz law states that  $K_e/\sigma$  is proportional to  $T_e$ , the proportionality constant being  $\sim (k_B/e^2)$  for a plasma; since  $\sigma$  and  $T_e$  are invariant, so is  $K_e$ . It can be verified, therefore, that each term in the electron energy equation scales as  $1/L^2$ , and the conservation law is satisfied by the same  $T_e$  at all scales. Elastic power loss to heavy particles also scales (per unit volume) as  $1/L^2$ , as can be easily verified as follows. The energy transferred from an electron to an ion due to an elastic collision per electron is

given by:

$$\delta\epsilon = \frac{2m}{M}\epsilon \quad (\text{A.19})$$

Then, the energy per unit volume per unit time can be written as:

$$P_{elastic} = \frac{\delta\epsilon}{t}n_e \sim \frac{1}{L^2} \quad (\text{A.20})$$

as desired. Radiative losses deserve special consideration. Due to the preservation of all mean-free-path ratios, the gas opacity will be preserved, and, since radiation is volumetric (optically thin limit) in existing Hall devices, it will remain so upon scaling. The radiative power loss per unit volume will then scale as the ionization rate,  $1/L^2$ , since both, ionization and excitation of atoms are driven by electron-atom collisions, and photon emission is prompt. Thus, the common practice of accounting for radiative losses by using in the electron energy balance an “effective” ionization energy of 2 – 3 times  $eV_i$  will remain valid, with the same factor at all scales. Notice that for devices or components where radiation is from the surface only (optically thick limit), radiative power losses per unit volume will scale as  $1/L$ , and will become weaker than other terms in the energy balance when  $L$  is reduced.

# Appendix B

## Additional Considerations in the Design of a 50 W Hall Thruster

### B.0.1 Vacuum insulation

The internal thruster walls are electrically insulated from the anode by a vacuum gap (as shown in Fig. B-1) which prevents any discharge from being initiated due to the presence of a gas leak. As the analysis below shows, the gap size scales directly with the mean free path for a given characteristic size, and therefore, vacuum insulation would be effective as long as the mean free path of the neutrals is much larger than the gap size. Assuming, as a worst case, that all of the flow will leak through the gap, the number density there can be determined from the following relation:

$$\dot{m} = \frac{m_i n c A}{4} \quad (\text{B.1})$$

where  $c$  is the speed of sound and  $A$  is the flow area of a cylindrical shell and is given by:

$$A = 2\pi r d \quad (\text{B.2})$$

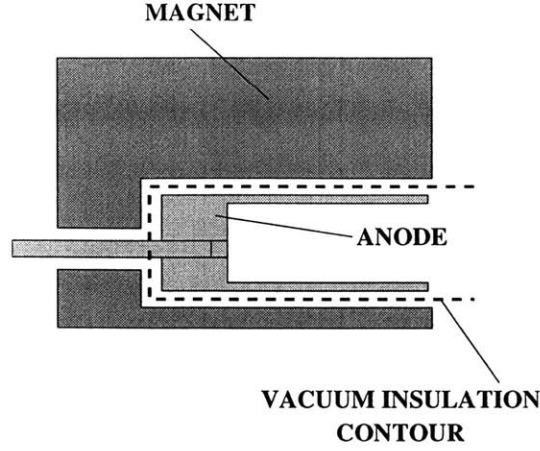


Figure B-1: Vacuum gap insulation

where  $r$  is the characteristic shell radius and  $d$  is the gap size. Thus, the ratio of the mean free path to the characteristic shell radius can be estimated to be:

$$\frac{\lambda}{d} = \frac{\pi r m_i c_n}{2 \dot{m} Q} \quad (\text{B.3})$$

where  $Q$  is the collision cross-section. Using typical values,  $\dot{m} = 0.2$  mg/sec,  $c_n = 350$  m/sec,  $r = 3$  mm,  $\lambda/d$  is on the order of 90, which is sufficient under the above assumptions. The actual gap size ( $\sim 0.3$  mm) was arrived at based on the tradeoff between the results of the magnetic circuit analysis, requiring smallest gap possible between the poles, together with the anode alignment and manufacturing considerations.

### B.0.2 Analytical thermal model of the anode

Assuming a 1-D geometry as shown in Fig. B-2, one can compute the temperature distribution along the anode, given the input power  $Q_{in} = 25$  W and the ambient temperature  $T_{amb} = 300$  K. It is further assumed that all of the heat is generated at the tip of the anode ( $x = 0$ ) and conducted through the capillaries to the insulating material (BN). It is then rejected to the support structure maintained at the ambient temperature. Along the surface of the anode, part of the heat flux is lost due to radiation to the surrounding magnet and to the central pole piece. These heat fluxes can be accounted for in the balance and the rate of change of the total heat flux along

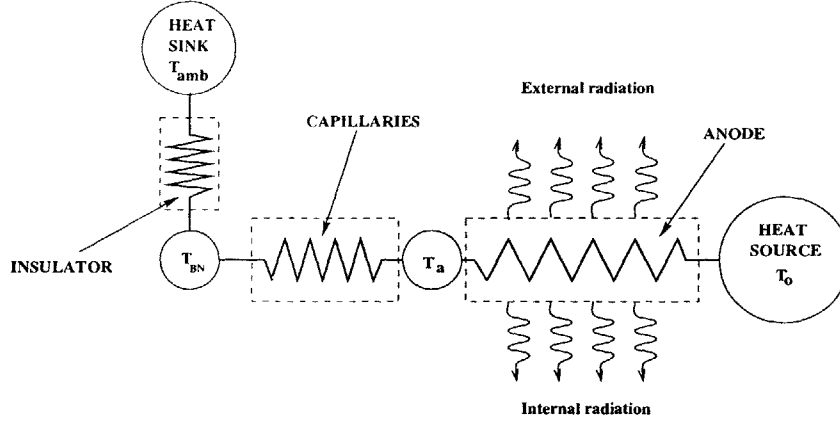


Figure B-2: 1-D thermal model

the anode can be written as follows:

$$\frac{dq(x)}{dx} = -2\pi(R_o + R_i)\epsilon\sigma T^4(x) \quad (\text{B.4})$$

Since the ultimate goal is to obtain a temperature profile, the total heat flux can be related to the anode temperature through the Fourier law:

$$q(x) = -k_a A_a \frac{dT(x)}{dx} \quad (\text{B.5})$$

These equations can be solved simultaneously with the appropriate boundary conditions to yield the following differential equation:

$$\frac{dT(x)}{dx} = -\sqrt{\frac{4\pi(R_o + R_i)\sigma\epsilon}{5k_a A_a} [T^5(x) - T_{tip}^5] + \left[\frac{Q_{in}}{k_a A_a}\right]^2} \quad (\text{B.6})$$

where  $R_o$  and  $R_i$  are the outer and inner radii of the anode respectively,  $k_a$  is the thermal conductivity of the anode material,  $A_a$  is its effective heat conduction area, and  $T_{tip}$  is the anode tip temperature. This equation is incomplete by itself and requires another condition. This condition can be obtained by relating the heat flux at the anode root ( $q_a$ ) to the respective temperature gradients across the capillaries

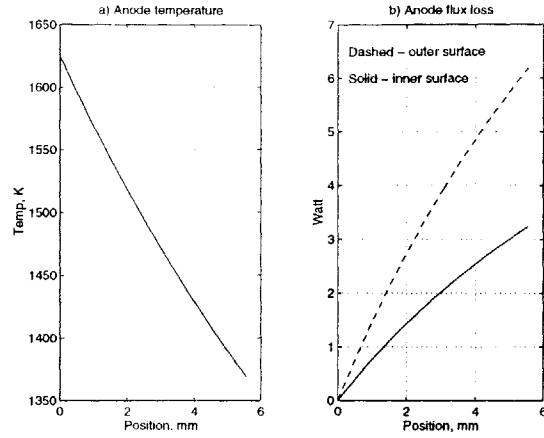


Figure B-3: (a) Anode temperature profile; (b) Radiative heat fluxes

and across the insulator:

$$q_a = \frac{(T_a - T_{BN})}{R_{cap}} \quad (B.7)$$

$$q_a = \frac{(T_{BN} - T_{amb})}{R_{BN}} \quad (B.8)$$

where  $R_{cap}$  and  $R_{BN}$  are the effective thermal resistances of the capillaries and the boron nitride (BN) insulator respectively. The last three equations can be solved iteratively to obtain the anode temperature distribution and the corresponding radiative heat fluxes to the central pole and to the outer magnets. With the proper choice of materials and component configurations it is possible to achieve reasonable tip temperatures with an adequate margin. The anode temperature profile along with the radiative heat fluxes predicted by the model for the selected geometry are shown in Fig. B-3.

# Bibliography

- [1] A.P. London. *A systems study of propulsion technologies for orbit and attitude control of micro spacecraft*. M.S. Thesis, MIT, 1996.
- [2] Roger M. Myers Steven R. Oleson. *Small Satellite Propulsion Options*. AIAA 94-2997, 1994.
- [3] J.E. Pollard S.W Janson. *Spacecraft electric propulsion applications*. Aerospace report AIR-96 (8201), 1996.
- [4] V. Khayms. *Design of a Miniaturized Hall Thruster for Microsatellites*. M.S. Thesis, MIT, 1997.
- [5] M. Martinez-Sanchez V. Khayms B. Ondrusek. *Scaling Potential of Pulsed Inductive Thrusters*. Article, 1997.
- [6] C.L. Dailey R.H. Loveberg. *The PIT MkV pulsed inductive thruster*. NASA Contractor Report 191155, 1993.
- [7] G. Eschard A. Pelissier J. Paulin J. Bonnal. *Experimental Studies of a Linear Strip Cesium Contact Ion Thruster*. AIAA 75-412, 1975.
- [8] Da-Ren Chen D. Pui S. Kaufman. *Electrospraying of conducting liquids for monodisperse aerosol generation in the 4 nm to 1.8 microns diameter range*. Journal of Aerosol Sci., 1995.
- [9] C.D. Hendricks R. J. Pfeifer. *Parametric studies of electrohydrodynamic spraying*. AIAA 66-252, 1966.

- [10] P. Kidd H. Shelton. *Life test (4350 hours) of an advanced colloid thruster module*. AIAA 73-1078, 1973.
- [11] R Moore J. Perel T. Bates, J. Mahoney. *Research on a charged particle bipolar thruster*. AIAA 67-728, 1967.
- [12] J. Perel J. Mahoney. *Duration test of an annular colloid thruster*. AIAA 72-483, 1972.
- [13] J. Mahoney H. Daley J. Perel. *Performance of colloid annular emitters*. AIAA 73-1076, 1973.
- [14] J. Rossel-Llompart J. Fernandez de la Mora. *Generation of monodisperse droplets 0.3 to 4 microns in diameter from electrified cone-jets of highly conducting and viscous liquids*. Journal of Aerosol Sci. Vol. 25, No. 6, pp. 1093-1119, 1994.
- [15] J. Fernandez de la Mora I.G. Loscertales. *The current emitted by highly conducting Taylor Cones*. Journal of Fluid Mech. Vol. 260 pp. 155-184, 1994.
- [16] J. Fernandez de la Mora. *The effect of charge emission from electrified liquid cones*. Journal of Fluid Mech. Vol. 243 pp. 561-574, 1992.
- [17] M. Gamero-Castano J. Fernandez de la Mora. *Direct measurement of ion evaporation of small ions from droplets*. Journal of Chem. Phys., 1999.
- [18] D. Laurini et al. *FEEP: Steady and Pulsed Modes of Operation*. AIAA 87-1046, 1987.
- [19] T.W. Haag. *Design of a thrust stand for high power electric propulsion devices*. 1989.
- [20] J.R. Brophy J.W. Barnett J.M. Sankovic D.A. Barnhart. *Performance of the Stationary Plasma Thruster: SPT-100*. 1992.
- [21] H. Loeb G. Popov. *Advanced Interplanetary Mission of the XXI Century*. 1995.

- [22] J.M. Sankovic T.W. Haag. *Operating Characteristics of the Russian D-55 Thruster with Anode Layer*. 1994.
- [23] et al K. Komurasaki. *Plasma Acceleration Processes in a Hall-current Thruster*. 1991.
- [24] J. Zeleny. *Instability of electrified liquid surfaces*. Phys. Review, Vol. 10, No. 1, 1917.
- [25] J. Zeleny. *The electrical discharge from liquid points and a hydrostatic method of measuring the electric intensity at their surfaces*. Phys. Review, Vol. 3, No. 2, 1914.
- [26] G.I. Taylor. *Disintegration of water drops in an electric field*. Proc. Royal Soc. of Lond. A 280, pp. 383-397, 1964.
- [27] A.J. Mestel. *The electrohydrodynamic cone-jet at high Reynolds number*. Journal of Aerosol Sci. Vol. 25 No. 6 pp. 1037-1047, 1994.
- [28] J. Fernandez de la Mora L. de Juan. *Charge and size distributions of electrospray drops*. Journal of Colloid and Interface Sci. 186, pp. 280-293, 1997.
- [29] I. Loscertales J. Fernandez de la Mora. *Experiments on the kinetics of field evaporation of small ions from droplets*. Journal of Chem. Phys. Vol. 103 Vol. 25, No. 12, 1995.
- [30] E. Cohen C. Somol D. Gordon. *A 100 kV, 10-Watt heavy particle thruster*. AIAA 65-377, 1999.
- [31] V. Krohn Jr. *Glycerol droplets for electrostatic propulsion*. EPC, Berkeley, CA, 1962.
- [32] H. Daley J. Mahoney J. Perel. *Colloid annular array thruster development*. AIAA 73-1077, 1973.
- [33] S. Rosen M. Huberman. *Advanced high-thrust colloid sources*. J. Spacecraft Vol. 11, No. 7, 1974.

- [34] A. Shtyrilin. *State of the art and future prospects of colloidal electric thrusters*. IEPC 95-103, 1995.
- [35] L.T. Cherney. *Structure of Taylor cone-jets: limit of low flow rates*. Journal of Fluid Mechanics, 1998.
- [36] M. Martinez-Sanchez. *Lecture notes 16.522 (appendix)*. MIT, 1999.
- [37] D. Smith. *The electrohydrodynamic atomization of liquids*. IEEE Transactions on Industry Applications, Vol IA-22, No. 3, 1986.
- [38] M. Martinez-Sanchez. *Progress report*. MIT, Busek, 2000.
- [39] D. R. Lide (editor). *Handbook of Chemistry and Physics*. 74th Edition, 1993.
- [40] J. Iribarne B. Thomson. *On the evaporation of small ions from charged droplets*. J. Chem. Phys. V. 64 pp. 2287-2294, 1976.
- [41] R.E. Hunter. *Theoretical considerations on non-uniformly charged expellant beams*. ARL TN 60 136, 1960.
- [42] M.S. Chung P.H. Cutler et al. *A first order electrohydrodynamic treatment of the shape and instability of liquid metal ion sources*. Surface Science 246, 118-124, 1991.
- [43] R.G. Forbes N. N. Ljepojevic. *Calculation of the shape of the liquid cone in a liquid-metal ion source*. Surface Science 246, 113-117, 1991.
- [44] L. Yun-Peng Z. Mao-Sheng. *A boundary element algorithm for the electric field of the Spindt device*. Surface Science 246, 75-78, 1991.
- [45] C. Pantano A.M Ganan-Calvo A. Barrero. *Zeroth-order, electrohydrostatic solution for electrospraying in cone-jet mode*. Journal of Aerosol Sci. Vol. 25 No. 6, 1994.

- [46] Alfonso M. Ganan-Calvo. *Cone-jet analytical extension of Taylor's electrostatic solution and the asymptotic universal scaling laws in electrospraying*. Physical Review Letters Vol. 79 Number 2, 1997.
- [47] Alfonso M. Ganan-Calvo. *On the theory of electrohydrodynamically driven capillary jets*. Journal of Fluid Mech. Vol. 335 pp.165-188, 1997.
- [48] I. Hayati A. Brailey T. Tadros. *Investigations into the mechanisms of electrohydrodynamic spraying of liquids*. Journal of Colloidal and Interface Sci. Vol. 117 No. 1, 1987.
- [49] J.R. Melcher E.P. Warren. *Electrohydrodynamics of a current-carrying semi-insulating jet*. Journal of Fluid Mech. Vol. 47 pp. 127-145, 1971.
- [50] R.G. Forbes N. N. Ljepojevic. *Liquid metal ion source theory: electrohydrodynamics and emitter shape*. Surface Science 266, pp. 170-175, 1992.
- [51] J. He P.H. Cutler et al. *Derivation of the image interaction for non-planar pointed emitter geometries: application to field emission IV characteristics*. Surface Science 246, pp. 348-364, 1991.
- [52] V.N. Kirichenko et al. *Acceleration of a free jet of low-conducting liquid in an electric field*. Dokl. Acad. Nauk SSSR 315 pp. 1066-1071, 1990.
- [53] V.N. Kirichenko et al. *Specific charge of the liquid in electrohydrodynamic atomization and microfilament forming processes*. Dokl. Acad. Nauk SSSR 315 pp. 819-826, 1990.
- [54] A.I. Grigorev S.O. Shiryayeva. *The theoretical considerations of physical regularities of electrostatic dispersion of liquids as aerosols*. Journal of Aerosol Sci. Vol. 25 No. 6 pp. 1079-1091, 1994.
- [55] A. M. Ganan-Calvo. *Cone-jet analytical extension of Taylor's electrostatic solution and the asymptotic universal scaling laws in electrospraying*. Phys. Review Letters, Vol. 79, No. 2, 1997.